Diffusion within aqueous atmospheric aerosol

Hannah Clare Price

School of Earth and Environment

School of Physics and Astronomy

University of Leeds

Submitted in accordance with the requirements for the degree of

Doctor of Philosophy

March 2015

The candidate confirms that the work submitted is her own, except where work which has formed part of jointly authored publications has been included. The contribution of the candidate and the other authors to this work has been explicitly indicated below. The candidate confirms that appropriate credit has been given within the thesis where reference has been made to the work of others. The work in chapter 2 to 5 of the thesis has appeared in publication as follows:

Price, H. C., Murray, B. J., Mattsson, J., O'Sullivan, D., Wilson, T. W., Baustian, K. J. and Benning, L. G. (2014). "Quantifying water diffusion in high viscosity and glassy aqueous solutions using a Raman isotope tracer method". Atmospheric Chemistry and Physics. Work presented in this publication is included in chapters 2 and 3. The candidate designed and performed all laboratory experiments, analysed the results and wrote the manuscript. The co-authors BJM, JM, DOS, TWW and LGB helped design the research; and JM, KJB and DOS helped analyse the Raman data. BJM and JM helped to write the paper.

Price, H. C., Mattsson, J., Zhang, Y., Bertram, A. K., Davies, J. F., Grayson, J. W., Martin, S. T., O'Sullivan, D., Reid, J. P., Rickards, A. M. J. and Murray, B. J. "Water diffusion in atmospherically relevant α-pinene secondary organic material". Submitted to Chemical Science. Work presented in this publication is included in chapters 2, 4 and 5. The candidate designed the research, performed the diffusion measurements, analysed the data, wrote the diffusion model and wrote the paper. JM, AKB, STM, JPR, BJM and YZ helped design the research. YZ generated the SOM sample. JFD, AMJR and JWG performed the EDB, optical tweezers and viscosity measurements, respectively. JM and DOS helped analyse the Raman data. JM, YZ and BJM helped to write the manuscript.

Acknowledgements

I would like to thank Ben Murray for introducing me to the field of atmospheric aerosol and for all of the opportunities he has given me, and for building my confidence by encouraging me to direct my own research. I am grateful to Johan Mattsson for his guidance, commitment to scientific rigour, enthusiasm and generosity with his time. I gratefully acknowledge funding provided for this project by the European Research Council and the Aerosol Society *via* the CN Davies award. I thank all those who encouraged me towards this PhD throughout my earlier studies, particularly John Cain, Walther Schwarzacher, Natasa Vasiljevic, Jeff Odell, Rob Parker and Hartmut Bösch.

I thank my co-workers at Leeds for valuable discussions and help in the lab, especially Kelly Baustian, Tamsin Malkin, Nsikanabasi Umo, Daniel O'Sullivan, Tom Whale, Theo Wilson, Jim Atkinson, Ross Herbert and Jim McQuaid. I also express my gratitude to our collaborators from further afield for sharing their knowledge and expertise (and samples), especially Jonathan Reid, Scot Martin, Allan Bertram, James Davies, Yue Zhang, James Grayson and Andrew Rickards. Thanks also go to Tony Windross in mechanical workshops for making the experiments possible, and to Richard Rigby, Andrew Rae and Fahed Alkhatib for their invaluable IT support.

I would also like to thank everyone in office 9.127 for such a pleasant working environment, and especially Annabel Jenkins, Anna Hogg and Kate Briggs, who made it all much nicer with lots of tea drinking. Thanks to my friends for being friendly, and especially Sarahs Kemp and Köhl for the lovely holidays during my final year. Finally, I would like to thank my mum and dad, and the rest of my family, for all their encouragement and support.

Abstract

Atmospheric aerosol particles influence our planet's climate and contribute to poor air quality, increased mortality and degraded visibility. Central to these issues is how atmospheric aerosol particles interact with gas species to affect chemistry and cloud formation. Recent research shows that some aqueous solutions relevant to atmospheric aerosol (notably secondary organic material, which constitutes a large mass fraction of atmospheric aerosol particles) can be highly viscous and can behave mechanically like a solid. This has led to suggestions that these particles exist out of equilibrium with the gas phase in the atmosphere, with implications for heterogeneous chemistry and ice nucleation. In order to quantify any kinetic limitations, it is vital to have quantitative data about the diffusion of various relevant species within these materials.

This thesis describes the direct measurement and application of water diffusion coefficients in aqueous solutions relevant to atmospheric aerosol, including sucrose and secondary organic material. A water diffusion model is developed, validated and used with a new parameterisation of the water diffusion coefficient in secondary organic material to quantify the rate of uptake and loss of water from aerosol particles. It is shown that, although this material can behave mechanically like a solid, at 280 K water diffusion is not kinetically limited on timescales of 1 s for atmospheric-sized particles. This is not the case, however, for colder conditions: modelling of 100 nm particles predicts that under mid to upper tropospheric conditions radial inhomogeneities in water content produce a low viscosity surface region and more solid interior. This may significantly affect aerosol chemistry and the ability of particles to nucleate ice.

Also reported are the diffusion coefficients of sucrose in aqueous sucrose at higher concentrations than have been previously investigated.

These measurements provide insights into the role of organic molecules in aerosol evaporation and chemistry. Together with the diffusion coefficients of water measured in this material, they will also offer a valuable means to study the fundamental nature of diffusion in a simple but widely used material, and specifically the breakdown of the Stokes-Einstein relationship.

Abbreviations

BVOC	Biogenic volatile organic compound
CCD	Charge-coupled device
CCN	Cloud condensation nuclei
FWHM	Full width at half maximum
HTDMA	Hygroscopic tandem differential mobility analyser
INP	Ice nucleating particle
M5AS	A mixture of malonic acid, malic acid, maleic acid, glutaric acid, methylsuccinic acid and ammonium sulphate
NMR	Nuclear magnetic resonance
RH	Relative humdity (with respect to liquid water, unless specified as ice)
SE	Stokes-Einstein
SOA	Secondary organic aerosol (particles suspended in vapour)
SOM	Secondary organic material (the material of which SOA particles are composed)
TTL	Tropical tropopause layer
VFT	Vogel-Fulcher-Tammann
VOC	Volatile organic compound

Contents

List of Figures

Chapter 1

Introduction

Water-soluble compounds are ubiquitous in atmospheric aerosol, which is important for the planet's climate and hydrological cycle. The ability of aerosol particles to scatter and absorb light impacts Earth's radiation budget directly, and they also influence climate indirectly by mediating cloud properties through their action as cloud condensation nuclei (CCN) and their ability to serve as ice nucleating particles (INPs) (Boucher *et al.*, 2013; Carslaw *et al.*, 2010). It is therefore of vital importance to understand aerosol particle phase transitions and interactions with water vapour, and the consequences of these for aerosol optical properties, chemical reactions and health effects (Pöschl, 2005).

1.1 Atmospheric aerosol

Atmospheric aerosol may be anthropogenic or natural in origin, and may be emitted as primary particles (e.g. mineral dust, sea salt, black carbon and primary biological particles) or form from gaseous precursors (e.g. non-sea salt sulphate, nitrate, ammonium and secondary organic aerosol, SOA). In order to understand the optical properties of aerosol particles and how they affect clouds, it is vital to know about their number size distribution, chemical composition, mixing state and morphology. This is regulated by complex transformations in the atmosphere which are not fully understood at present (Boucher *et al.*, 2013). Gas-particle interactions affect gas and particle composition, affecting aerosol chemistry, hygroscopicity, optical properties and lifetimes (Abbatt *et al.*, 2012). Therefore, in

order to predict the composition of the atmosphere and atmospheric processes it is vital to understand the physics and chemistry of heterogeneous (occuring on solid particles) and multiphase (occuring in liquid droplets) reactions (Ravishankara, 1997).

Organic material constitutes a large fraction of the mass concentration of atmospheric aerosol particles (Jimenez *et al.*, 2009; Kanakidou *et al.*, 2005). Even in the upper-troposphere, aerosol can contain more organic than sulphate material (Murphy *et al.*, 1998), and, as shown in fig. 1.1, a significant fraction (30 to 80%) of free tropospheric aerosol particle mass is carbonaceous (likely organic) (Murphy *et al.*, 2006).

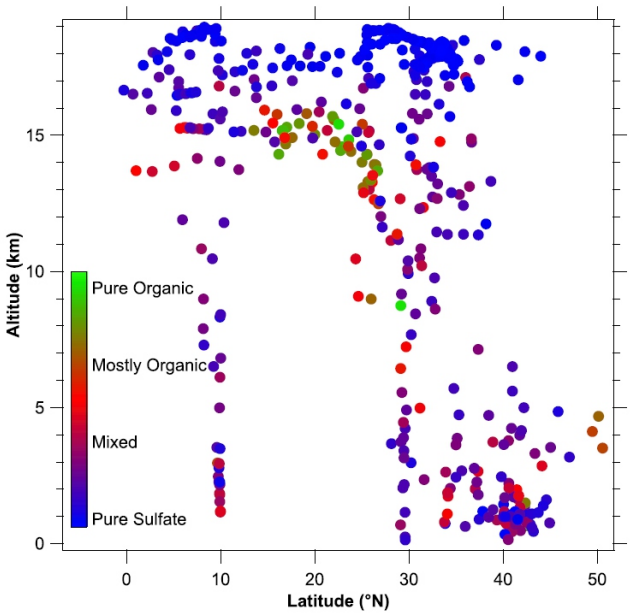

Figure 1.1: Aerosol composition based on negative ion mass spectra from Murphy *et al.* (2006).

A major source of condensed-phase organics in the atmosphere is the oxidation of volatile organic compounds (VOCs) to produce secondary organic aerosol (SOA), whose particles are composed of secondary organic material (SOM) (Jimenez *et al.*, 2009). SOA forms when low-volatitity vapours nucleate to form a clus-

ter which may grow into nanometre sized particles, or *via* condensation onto preexisitng seed particles. These particles grow to larger sizes *via* the further condensation of low-volatility vapours, and the representation of this process remains a challenge in climate modelling. Globally, most SOA is thought to be produced from biogenic volatile organic compounds (BVOCs) emitted by vegetation, although there are significant anthropogenic sources, particularly at northern mid-latitudes. The current uncertainty in SOA formation is large, at 20 to 380 $\mathrm{Tg{\cdot}yr^{-1}}$ (Boucher *et al.*, 2013), and the burden is predicted to increase in the future (Heald *et al.*, 2008). Chemical reactions in the particle phase, such as oligomerisation, reduce the volatility and increase the hygroscopicity of organic aerosol. This impacts the particles' radiative properties and interactions with water vapour to form clouds (Jimenez *et al.*, 2009). The ways in which SOA impacts upon atmospheric processes such as ice nucleation, cloud formation and heterogeneous or muliphase chemistry remain poorly understood.

1.2 Aqueous solutions and the glass transition

Liquid aqueous solutions respond to changes in the surrounding relative humidity (RH) by taking up (and losing) water in a process known as hygroscopic growth (top row, fig. 1.2). At equilibrium, the water activity of a solution droplet is equal to the surrounding relative humidity, $RH/100$. Inorganic salts abundant in the atmosphere typically exhibit hysteresis behaviour in response to changes in relative humidity: a crystalline particle will undergo prompt deliquescence followed by hygroscopic growth when RH is increased; when RH is decreased it will supersaturate below the deliquescence RH before rapidly effloresing (Martin, 2000) (middle row, fig. 1.2).

In some atmospheric aqueous solutions, solute crystallization at low RH or temperature can be inhibited, either partially or completely (Bodsworth *et al.*, 2010; Murray, 2008; Murray *et al.*, 2012; Murray & Bertram, 2008; Parsons *et al.*, 2004; Prenni *et al.*, 2001; Zardini *et al.*, 2008). This can be due to an increase in viscosity and associated decrease in the rate of diffusion within the solution as it supersaturates or supercools (bottom row, fig. 1.2). Below the melting point of a material, as temperature decreases molecular motion slows down, and may slow

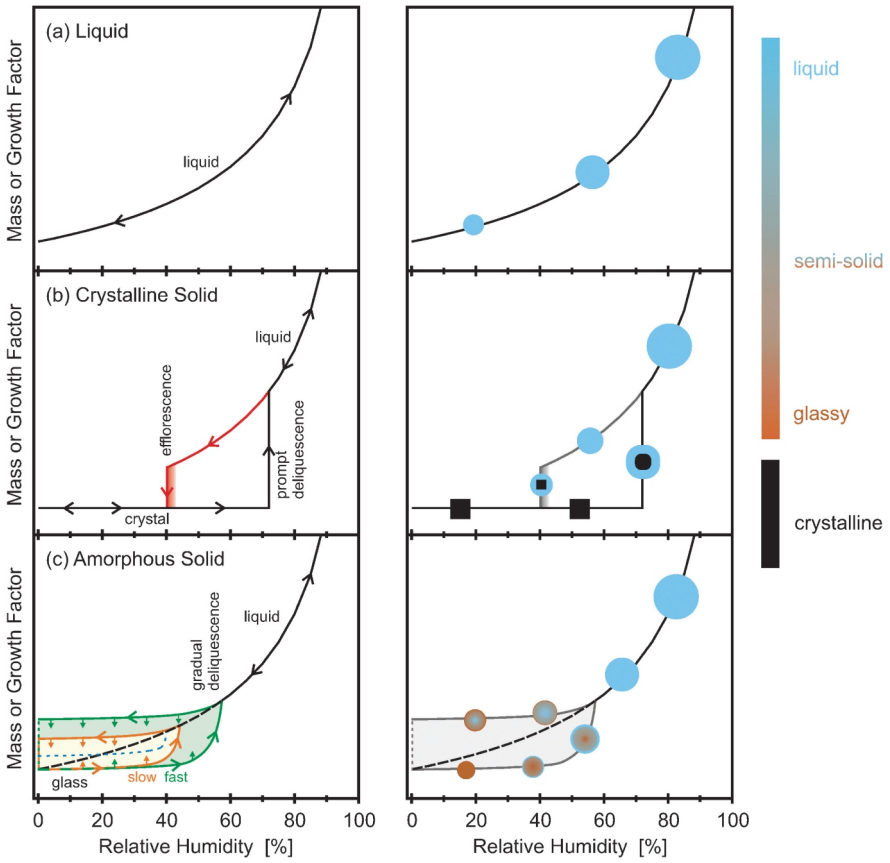

Figure 1.2: Water uptake schematic taken from Koop *et al.* (2011). (a) As RH is increased or decreased, a droplet which is an aqueous liquid under all conditions at room temperature will take up or loose water without hysteresis behaviour. (b) When a water-soluble crystalline solid is exposed to increasing RH, it remains as a crystal until the deliquescence RH (DRH) is reached, at which point water uptake is prompt and an aqueous solution is formed. If RH is increased beyond the DRH, the droplet undergoes hygroscopic growth, as in (a). When RH is decreased below the DRH, the solution becomes supersaturated until crystallisation at the efflorescence RH. (c) An amorphous solid particle experiencing changes in RH will take up and loose water depending on the rate of change of RH. Water diffusion is slow in these materials, but is a self-accelerating process. Water uptake occurs in the outer layers of a droplet before progressing to its interior once these outer layers are softened, as shown by the gradient in colour of the droplets. Water loss may be inhibited by the formation of a solid crust, also shown by the colour gradient. If the rate of RH change is small (orange lines), water may have time to diffuse into or out of the particle at low RH, hence hygroscopic growth can be observed at lower RHs than if the rate of increase in RH is high (green lines).

to the extent that molecules are unable to sample enough configurations to crystallise. In this case the material may form a glass, with the physical properties of a solid but without the long-range molecular order of a crystal. This slowing down of molecular motion corresponds to an increase in viscosity - one definition of the glass transition temperature is the point at which viscosity increases above 10^{12} Pa·s. Near to the glass transition, the viscosity is highly dependent on temperature. In some materials, this dependence may be close to Arrhenius behaviour (i.e. $\eta = Ae^{E/k_BT}$, where A and E are constants), indicating that the activation energy does not depend on temperature; these materials are described as "strong". In others the increase in viscosity may be even stronger as temperature decreases, implying that the activation energy increases as temperature decreases; these materials are known as "fragile".

At high temperatures, viscosity is inversely related to translational diffusion by the Stokes-Einstein relation:

$$D = \frac{k_B T}{6\pi\eta r} \tag{1.1}$$

where k_B is the Boltzmann constant, T is the temperature, η is the viscosity and r is the radius of the diffusing molecule. However, this relation breaks down at $\frac{T_g}{T} \sim 0.8$ (depending on fragility), below which point diffusion slows to a lesser extent than would be expected based on viscosity (Chang & Sillescu, 1997; Edmond *et al.*, 2012; Mapes *et al.*, 2006; Rössler *et al.*, 1994).

This breakdown is more pronounced in fragile than in strong materials but it is not completely understood at present and is an area of active research. An explanation of the breakdown is thought to lie in the shape of the potential energy landscape (the multi-dimensional surface describing the potential energy of the system as a function of position, orientation and vibration coordinates). The way in which a material samples this landscape determines its dynamic behaviour (Stillinger *et al.*, 1995). When a system has enough kinetic energy to sample the whole landscape, it "sees" that most minima are shallow. The rearrangement of a small number of molecules is needed to traverse these low energy barriers. When its kinetic energy decreases, the system may be unable to traverse the largest energy barriers, so gets "stuck" in any deeper minima and becomes unable to sample the full landscape. In this situation, relaxation

will involve the rearrangement of a large number of molecules (Debenedetti & Stillinger (2001) and references therein).

In strong materials, which may have only a single deep trough in the potential energy landscape, the activation energy remains almost constant as the glass transition is approached. In materials with many seperated troughs, the activation energy for relaxation increases as the glass transition is approached. This is the super-Arrhenius behaviour which characterizes fragile materials. The heterogeneity of the potential energy landscape in fragile materials leads to a range of relaxation times and the material is thus dynamically heterogeneous. Close to the glass transition, at any one time most of the molecules are non-diffusing with a few areas of mobile molecules. The Stokes-Einstein relationship is based on macroscopic hydrodynamics which assumes the material is a continuum. This is not the case in fragile materials, and is thought to lead its breakdown (Angell *et al.*, 2000; Cicerone & Ediger, 1996).

In aqueous solutions, the glass transition is concentration dependent, and an increase in concentration upon supersaturation at fixed temperature can be viewed as very roughly akin to a decrease in temperature upon supercooling in a solution of fixed concentration. There is an inherent difference between these two phenomena: during a variation in concentration the material itself changes, whereas during a variation in temperature the material stays the same but different regions of its energy landscape are sampled. Nevertheless, the glass transition may be defined by relative humidity or water activity as well as temperature, as shown in fig. 1.3.

1.3 The phase of atmospheric aerosol

It has been proposed that atmospheric aerosol particles may be present in the form of a glass or semi-solid (e.g. a gel or rubber) over a wide range of temperature and relative humidity conditions (Bahreini *et al.*, 2005; Mikhailov *et al.*, 2009; Murray *et al.*, 2012; Perraud *et al.*, 2012; Renbaum-Wolff *et al.*, 2013; Roth *et al.*, 2005; Saukko *et al.*, 2012b; Virtanen *et al.*, 2010; Zobrist *et al.*, 2008). Measurements of the phase of atmospheric aerosol are challenging because bulk samples are typically not available. Proxies are sometimes used, but experiments in bulk are

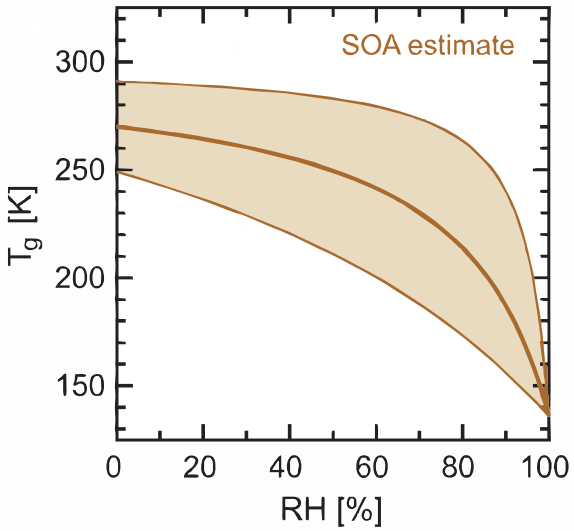

Figure 1.3: Estimated glass transition temperatures of SOM as a function of RH, from Koop *et al.* (2011)

still often not possible because the supersaturation and supercooling accessible to small droplets is not possible in the bulk. The phase state of aerosol populations has been inferred using impactors, whereby particles which bounce are inferred to be more solid than those which adhere to a surface (Saukko *et al.*, 2012a). The viscosity of proxies for mixed organic/inorganic aerosol has been measured by Power *et al.* (2013) via the coalescence of aerosol particles in optical tweezers, and by Hosny *et al.* (2013) using fluorescence lifetime imaging microscopy of molecular rotors. Renbaum-Wolff *et al.* (2013) measured the viscosity of chamber-generated SOM using the mobilty of beads and the time for recovery after the application of physical force to particles composed of SOM.

A highly viscous or glassy phase would result in reduced diffusion coefficients in comparison to the liquid phase, causing delayed interactions with gases and potentially impacting particles' optical properties through their ability to take up water (Bones *et al.*, 2012; Lu *et al.*, 2014; Murray *et al.*, 2012; Tong *et al.*, 2011). Water uptake by amorphous solids initially occurs at the surface of a particle, proceeding to the interior only when the outer layer has softened and the rate

of diffusion increased (Koop *et al.*, 2011; Zobrist *et al.*, 2011). In this way, the viscosity gradually decreases as the particle undergoes continual deliquescence, and hygroscopic growth occurs at lower relative humidity than for the particle's crystalline counterpart (Mikhailov *et al.*, 2009). When RH is decreased, a core-shell structure may develop as a glassy crust forms around a less viscous interior. Consequently, water may be trapped inside the particle, even under dry conditions (Koop *et al.*, 2011; Zobrist *et al.*, 2011). The addition of a glass-forming organic compound to ammonium sulphate has the effect of supressing its efflorescence, meaning that water uptake and optical growth is possible at intermediate RHs, below the deliquescence point of pure ammonium sulphate (Robinson *et al.*, 2014).

Highly viscous aerosol may undergo diffusion limited growth, which would result in a different size distribution to that produced by the quasi-equilibrium growth of liquid aerosol (Zhang *et al.*, 2012). In laboratory or field measurements, timescales for equilibration longer than typical thermodenuder residence times may also lead to erroneous volatility results (Saleh *et al.*, 2011). The phase of atmospheric aerosol is thought to change with age: oxidation of atmospherically relevant compounds has been linked to an increase in viscosity (Hosny *et al.*, 2013), and the glass transition temperature is known to correlate with the atomic oxygen-to-carbon ratio (O:C ratio) (Dette *et al.*, 2014; Koop *et al.*, 2011).

The possible occurance of a highly viscous phase in SOM is of particular interest due to its abundance in the atmosphere and the discrepancies which currently exist between model descriptions and observations (Ehn *et al.*, 2014; Hallquist *et al.*, 2009; Shiraiwa & Seinfeld, 2012; Tsigaridis *et al.*, 2014). SOA particles grow via the condensation of organic vapours, a process which may be affected by the phase of the particles (Riipinen *et al.*, 2012). The phase of SOA particles is governed by humidity: bounce measurements show that the hygroscopic nature of SOM can cause particles to rebound off an impactor to a lesser extent at higher RH (Bateman *et al.*, 2014b; Saukko *et al.*, 2012b). The addition of organics such as SOM to hygroscopic sulphate particles might slow cloud droplet growth kinetics, although perhaps not enough for it to be rate limiting in the atmosphere (Wong *et al.*, 2014). Figure 1.3 shows the predicted glass transition temperature of SOM as a function of water activity and temperature. By comparing this figure

to fig. 1.4 and fig. 1.5, which give the global mean variation of RH and temperature with altitude and latitude, it can be seen that a significant proportion of the troposphere matches the conditions under which SOM is thought to exist in a glassy state.

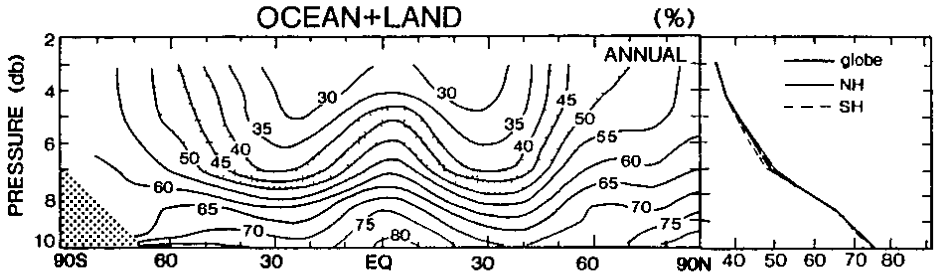

Figure 1.4: Vertical and latitudinal profile of the mean annual RH, adapted from (Peixoto & Oort, 1996).

1.3.1 Ice nucleation by viscous organic aerosol

The concentration of ice nucleating particles (INPs) in the atmosphere is very uncertain and has an important impact on climate. Highly viscous organic aerosol particles have been found to act as heterogeneous INPs and may play a role in cirrus cloud formation (Baustian *et al.*, 2013; Murray *et al.*, 2010; Wagner *et al.*, 2012; Wang *et al.*, 2012; Wilson *et al.*, 2012). Proxies for SOA, such as mixtures of carboxylic acids or organics, sugars and ammonium sulphate, are known to nucleate ice under cirrus conditions when in a highly viscous or glassy state (Baustian *et al.*, 2013; Murray *et al.*, 2010; Wagner *et al.*, 2012; Wilson *et al.*, 2012). Wang *et al.* (2012) reported immersion mode freezing by SOM above 230 K, and deposition mode freezing between 200 and 230 K at an RH_{ice} 10-15% below the homogeneous ice nucleation threshold. Möhler *et al.* (2008) found that 1% of SOA particles nucleated ice at temperatures between 205 and 210 K (RH_{ice} between 150 and 190%), and an SOM coating suppressed the ice nucleating abilities of mineral dust. Prenni *et al.* (2009) found SOA to be ineffective at

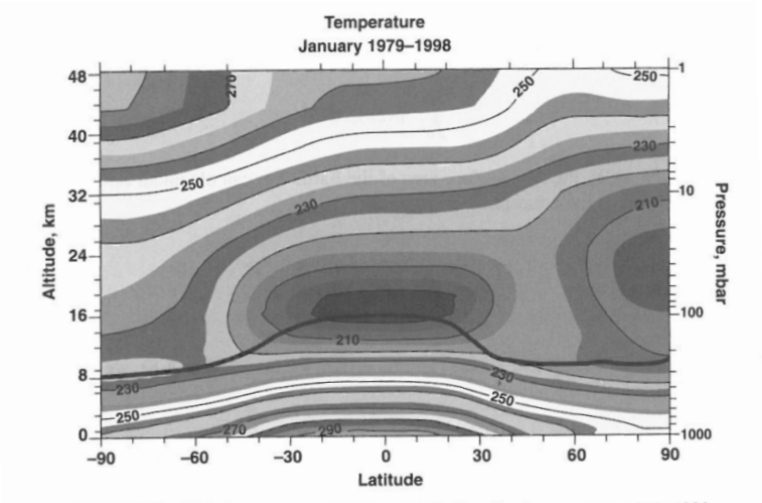

Figure 1.5: Vertical and latitudinal profile of mean January temperature (Seinfeld & Pandis, 2012).

nucleating ice at 243 K, and Ladino *et al.* (2014) found SOA to be not highly active as INPs between 213 and 233 K. Schill & Tolbert (2013) examined the ice nucleating effect of organic coatings on solid ammonium sulphate cores, and found that above 220 K water diffused through the organic shell and froze on the ammonium sulphate core. At 215 K, ice nucleated at the air-organic interface, implying that the organic coating had become sufficiently solid-like to induce freezing. The freezing of humidified organic aerosols can modify their morphology and lead to the formation of a porous structure and an increase in particle size once ice sublimes (Adler *et al.*, 2013, 2014). This porous structure alters the optical properies of the aerosol and may affect its ability to nucleate ice.

Heterogeneous nucleation of ice on glassy aerosol particles well below water saturation may lead to less, but larger, ice crystals which have a greater sedimentation velocity; this may be particularly important in the very cold and dry tropical tropopause layer (TTL) (Murray *et al.*, 2010). Froyd *et al.* (2010) propose that the enhancement of sulfate-organic material in subvisible cirrus residue relative to unfrozen aerosol indicates that this material was effective at nucleating

ice in this region. Clouds in the TTL have a non-negligible radiative impact and regulate the transport of water vapour into the stratosphere (McFarquhar *et al.*, 2000), a driver for climate change (Solomon *et al.*, 2010).

1.3.2 Kinetic limitations to mixing and gas-particle partitioning

If diffusion within aerosol particles is very slow, mixing within particles will be limited and volatile components will not have immediate access to the surface of a particle. This will mean that they do not evaporate as expected according to thermodynamic equilibrium partitioning - volatile species will be "trapped" inside particles and their evaporation inhibited. Several studies have suggested that organic atmospheric aerosol particles are not in equilibrium with surrounding gas phase compounds (Abramson *et al.*, 2013; Perraud *et al.*, 2012; Roth *et al.*, 2005). If this is the case, it could lead to errors in the evaluation of particle-phase and gas-phase concentrations (Liu *et al.*, 2013; Shiraiwa & Seinfeld, 2012; Shiraiwa *et al.*, 2013). Vaden *et al.* (2011) observed slow evaporation rates in SOA and attributed this to condensed phase kinetic limitations to gas-particle partitioning. Cappa & Wilson (2011) reported that the evaporation of α-pinene SOA particles is not described by partitioning theory, speculating that this was due to low diffusivity: aerosol components did not evaporate according to their various vapour pressures, so it was inferred that they were unable to reach the surface of the particle and a kinetic limitation on the particle-to-gas evaporative flux was imposed. Loza *et al.* (2013) observed that SOA formed sequentially from two different precursors evaporated in the same way as SOA from the second precursor, implying that mixing between the two types of SOM is limited. This was attributed to slow diffusion.

However, there may be an alternative explanation for some of these observations. The slow evaporation of semi-volatile components from SOA particles can have two origins - kinetic and thermodynamic. In the first, as described above, slow diffusion of the evaporating component within the particle bulk may lead to slow mixing within the particle, imposing a kinetic limitation on the particle-to-gas flux. In the second, components of SOM can be of such low volatility (due to

low vapour pressure and low mixing ratio, see for example Ehn *et al.* (2014)) that the evaporative flux into the gas phase is low and the evaporation timescale is long, a process driven by the inherent thermodynamic properties of the complex mixture (Cappa & Wilson, 2011; Saleh *et al.*, 2013). It is difficult to distinguish between these two origins in evaporation experiments. In an experiment directly measuring equilibration timescales at 30°C, Saleh *et al.* (2013) reported no substantial gas-particle partitioning inhibition due to kinetic limitations within particles. Robinson *et al.* (2013) observed mixing within laboratory-generated SOA on the minute timescale at room temperature. They used single-particle mass spectrometry to find that toluene SOA mixed into α-pinene SOA, implying that the diffusion coefficients within these particles were high enough for mixing to happen on timescales of minutes. Gas-particle partitioning occurred on a timescale of 1-2 hours in a study of pine-forest aerosol by Yatavelli *et al.* (2014). There, the response of partitioning to temperature changes was rapid, so kinetic limitations to partitioning were interpreted as minor (although the RH at this particular site was usually greater than 30%). A lack of mixing between condensed phases may not necessarily imply slow diffusion. Robinson *et al.* (2013) showed that mixing in organic aerosol particles can be inhibited thermodynamically (components may simply be immiscible) without being kinetically hindered by slow diffusion.

The volatility of SOA is governed by particle age and the environmental conditions to which it has been exposed. Aged SOA particles have been seen to evaporate to a lesser extent than fresh particles, implying a reduction in volatility with age, and particles formed in the prescence of water vapour contain more lower-volatility components than those formed under dry conditions (Wilson *et al.*, 2014). Thus, deciphering which processes underpin the observations noted above is a complex task. The discrepancies between evaporation- and equilibration-rate measurements highlight the need for more direct measurements of potential kinetic limitations in aerosol particles.

1.3.3 Influence of particle phase on reactivity

The phase of an aerosol particle is known to affect its reactivity (Knopf *et al.*, 2005; Kuwata & Martin, 2012). As noted earlier, the phase of atmospheric aerosol depends on its temperature and surrounding RH (and their history), as well as its age and composition. Broadly speaking, a decrease in molecular mobility with decreasing temperature (and increasing altitude) and decreasing RH is thought to reduce reactivity. When translational motions are reduced, it is likely that in many cases oxidation will be less efficient. The weakening of oxidative ageing could lead to the chemical lifetimes of condensed organics being significantly increased (Pfrang *et al.*, 2011; Shiraiwa *et al.*, 2010, 2011). This would affect source apportionment, potentially leading to underestimations of, for example, biomass burning aerosol concentrations (Shiraiwa *et al.*, 2012; Slade & Knopf, 2014). Likewise, an organic coating through which diffusion of gas-phase species was slow may provide a shield from oxidation, enabling hitherto unexpected transport.

Several studies have examined the importance of phase in the ozonolysis of condensed species. Chan & Chan (2012) found that the rate of ozonolyis of maleic acid/ammonium sulphate mixtures was depenent on RH, which was interpreted as a dependence on phase. The degradation rate of shikimic acid during ozonolysis depends on RH and appears to be controlled by the diffusion coefficient of ozone, and is also dependent on partical size, indicating that slow diffusion limits the reaction to a thin layer at the surface of the particles (Steimer *et al.*, 2014). Ozone uptake coefficients on bovine serum albumin were found to increase with RH and it was determined that oxidative ageing in this material was diffusion limited (Shiraiwa *et al.*, 2011). Gallimore *et al.* (2011) and Lee *et al.* (2012) found that the effect of RH on the ozonolysis of carboxylic acids was compound dependent: whilst RH had little effect on the ozonolysis of oleic acid (which is known to be liquid under all conditions at the investigated temperature), it had a significant effect on the ozonolyis of maleic and arachidonic acid (which are known to become more solid during oxidation or as RH decreases). Interestingly, water is known not to change the chemistry of oleic acid oxidation, but is a key reactant in maleic acid oxidation.

1. INTRODUCTION

Highly viscous organic coatings have been shown to be better than liquid layers at supressing the ozonolysis of the core which they protect. Weitkamp *et al.* (2008a) found that an SOM coating decreased the reaction of unsaturated compounds from meat cooking emissions with ozone. Zhou *et al.* (2012) coated an ammonium sulphate/benzo[*a*]pyrene core with either a liquid (bis(2-ethylhyxyl)sebacate or phenyl-siloxane oil) or a solid (eicosane) organic, and exposed it to ozone. The liquid coating did not affect the kinetics of the heterogeneous reaction, but the reactivity of benzo[*a*]pyrene was reduced by a thin film of solid eicosane and completely supressed by a thick coating. The same group also found that an SOM coating at low RH slowed the ozone and benzo[*a*]pyrene reaction, but the coating was less important at higher RH (by 70%, it had little effect) (Zhou *et al.*, 2013).

The OH oxidation reaction does not seem to be affected by a viscous organic coating in the same way as ozonolysis. Weitkamp *et al.* (2008b) found that what was thought to be an SOM coating on motor oil did not make a difference to the rate constants of the OH oxidation reaction. This was in contrast to the same group's observations of the effect of an SOM coating on the reaction of ozone with meat cooking emissions (Weitkamp *et al.*, 2008a). They suggest that the differing responses could be explained if the SOM had not in fact formed a coating, but instead mixed with the seed particle. Given that ozonolysis occurs in the bulk, whereas OH reacts with a thin surface layer, the latter would be less affected by the presence of incorporated SOM. Kolesar *et al.* (2014) found that the OH-initiated heterogeneous oxidation of squalane particles was not supressed by an α-pinene SOM coating - instead, the effective uptake coefficients increased with coating thickness. The authors hypothesize that OH radicals react with the SOM and generate organic radicals. In this way, the SOM coating acts to present a larger surface area for the uptake of OH. If this is indeed the case, it would seem that the ability of a viscous organic coating to shield a core from oxidation depends on the oxidant - the available evidence seems to suggest that an organic coating can inhibit ozone reactivity by physically separating the reactants, whereas OH oxidation at the surface apparently allows radicals to chemically migrate through a highly viscous medium to the core.

As well as reducing the viscosity and increasing diffusion coefficients within aerosol, the water content associated with higher RH can affect chemical reactions and block reactive sites (see Jia & Xu (2014); Slade & Knopf (2014) and references therein). Slade & Knopf (2014) examined the OH oxidation of organic aerosol, and found that OH uptake by levoglucosan is enhanced at higher RH (apparently because of lower viscosity), but OH uptake by methyl-nitrocatechol is reduced at higher RH. The differing response was ascribed to the relative importance of water's different effects: in levoglucosan, the reduced viscosity with increasing water content improved OH uptake, whereas the low water-solubility of methyl-nitrocatechol is thought to have enabled a layer of water to accumulate at the particle surface, blocking the reactive sites to OH. Wang *et al.* (2014) noted that in a reaction between α-pinene SOM and NaCl at 95% RH (when the particles were thought to be liquid and so free from kinetic limitations) higher chloride depletion was observed for longer reaction times. It was suggested that this could be attributed to interactions between the SOM and water - some of the organic components are hydrolysed to produce smaller acids which dissociate and fuel the reaction.

Clearly, the reactivity of organic atmospheric aerosol is not solely regulated by particle phase, which in turn is not solely regulated by water content and temperature. Water does have a plasticising effect on hygroscopic particles, but it also has chemical effects which can be important for reactivity. Other factors (e.g. miscibility and solubility) are important besides diffusivity, and caution should be exercised when attributing a decrease in reactivity wholly to an increase in viscosity. The condensed-phase material with which a reactant is mixed affects its reactivity in the atmosphere, and thus single-component data cannot easily be extrapolated to the real world. Detailed kinetic models (Roldin *et al.*, 2014; Shiraiwa *et al.*, 2013; Zaveri *et al.*, 2014) are required to unravel the complexities of aerosol processes, and these require knowledge of the diffusion coefficients of component species.

1.4 Quantifying diffusion in aqueous aerosol

Diffusion is the transport phenomenon which occurs due to the thermal motion of molecules. Where concentration gradients exist, Brownian motion results in the transfer of a substance from regions of high concentration to regions of low concentration. In the absence of concentration gradients, the random motion of molecules results in self-diffusion. Diffusion is described by Fick's laws, the first of which states that the diffusive flux, J (the amount of substance per unit area per unit time), is proportional to the concentration gradient:

$$\mathbf{J} = -D\nabla\phi \tag{1.2}$$

where D is the diffusion coefficient and ϕ is the concentration (amount of substance per unit volume). Fick's second law describes the evolution of the concentration gradient with time, t:

$$\frac{\partial\phi}{\partial t} = D\Delta\phi \tag{1.3}$$

Current techniques used to determine the formation and properties of semi-solid and glassy aerosol often involve some method of establishing mechanical properties such as viscosity, quantitatively or qualitatively (Hosny *et al.*, 2013; Renbaum-Wolff *et al.*, 2013; Virtanen *et al.*, 2010; Wang *et al.*, 2012). Whilst these techniques give information about phase, on their own they cannot be used to predict kinetic processes; for example, it has been shown that bounce measurements might not necessarily indicate long equilibration timescales (Bateman *et al.*, 2014a). As mentioned in section 1.2, the Stokes-Einstein relation cannot always be used to predict diffusion from viscosity: the mobility of water and larger molecules deviate near the glass transition (Champion *et al.*, 1997; Power *et al.*, 2013; Rampp *et al.*, 2000; Zhu *et al.*, 2011), and diffusion coefficients do not always vary with temperature in the same way as viscosity (Debenedetti & Stillinger, 2001; Parker & Ring, 1995). Since it is diffusion, rather than viscosity, which is key to quantifying the response of aerosol to changing conditions, it is advantageous to directly measure the diffusion coefficients of the species of interest, rather than inferring them from the viscosity.

The diffusion coefficient of water, D_{water}, in atmospheric aerosol is a particularly important parameter because water is often the most mobile component of a glassy aqueous solution (Roberts & Debenedetti, 1999) and it is crucial in cloud formation processes. As discussed earlier, water can act as a plasticiser (Koop *et al.*, 2011; Zobrist *et al.*, 2011), is a reactant (Ravishankara, 1997), and can act as a barrier to gas uptake by blocking surface sites (Pöschl *et al.*, 2001; Rubasinghege & Grassian, 2013). The plasticizing effect of water leads to difficulties in measuring its diffusion coefficient in highly viscous aerosol undergoing hygroscopic growth or shrinkage because the diffusion equation becomes non-linear (Tong *et al.*, 2011). Water diffusion coefficients in single-component aqueous solutions have been predicted using a free volume model (He *et al.*, 2006) and by reproducing water uptake and loss in suspended droplets with a multi-shell diffusion model (Lienhard *et al.*, 2014; Zobrist *et al.*, 2011). Zhu *et al.* (2011) used Raman and NMR spectroscopy to directly measure water diffusion in aqueous maltose, providing some of the only measurements of the diffusion coefficient of water at very high solute concentrations. Water diffusion coefficients in SOM have been predicted using percolation theory (Shiraiwa *et al.*, 2013) and inferred using a semi-empirical approach (Berkemeier *et al.*, 2014). Direct measurements are needed to test these models and these were not available prior to the present work.

In aqueous solutions, large organic molecules diffuse more slowly than water molecules. Quantifying just how much more slowly is key to predicting how aerosol particles will evaporate and interact with gas phase species via multiphase and heterogeneous chemistry. Few studies report literature data for organic diffusion in solutions relevant to organic aerosol, and those which quantify diffusion coefficients do so using indirect methods (Abramson *et al.*, 2013; Zhou *et al.*, 2013). Again, direct methods of evaluating diffusion in highly viscous materials are highly desirable.

1.5 Thesis structure

This thesis is concerned with the measurement and application of diffusion coefficients in highly concentrated aqueous solutions. The experimental methods

developed for the quantification of slow diffusion are described in chapter 2. The results of water diffusion experiments are given in chapters 3 and 4 for simple proxies for atmospheric aerosol and α-pinene SOM, respectively. Chapter 5 details a water diffusion model which is used to relate the results of the previous chapter to real-world situations. Chapter 6 presents the results of sucrose diffusion measurements, and chapter 7 provides a summary and conclusions.

Chapter 2

Raman isotope tracer methods

In the previous chapter, the need for measurements of diffusion coefficients in aqueous solutions relevant to atmospheric aerosol was identified. In this chapter, two experimental systems are described which are designed for this purpose, whereby Raman spectroscopy is used to directly monitor the diffusion of isotope tracers in aqueous solutions.

2.1 Raman spectroscopy

By monitoring the spatial and temporal evolution of the Raman spectrum, diffusion of molecules within a sample may be monitored. Unlike Rayleigh scattering, where incident and scattered photons have the same energy, Raman scattering is an inelastic effect: the interaction between a photon and a molecule causes a transfer of energy so that the scattered photon has a frequency that is shifted from the incident light.

Figure 2.1 shows the transitions between vibrational states which occur during Rayleigh and Raman scattering. In both cases, an incoming photon excites a molecule to a higher energy, short-lived "virtual" state. A photon is emitted via the Raman effect when the molecule then makes a transition to a different vibrational state than its original state. For vibrations to be Raman active, they must cause a change in the polarizability of the molecule. The difference in energy between the original and final energy state of the molecule determines the shift in frequency between the incident and emitted photons. If the final

state is higher in energy than original state then the scattered photon has lower energy than original; this is known as Stokes scattering. If the final state is lower in energy than the original state then the scattered photon will have a higher energy than the incoming photon; this is known as Anti-Stokes scattering. Anti-Stokes scattering is usually weaker in intensity, so spectrometers typically measure Stokes scattering radiation.

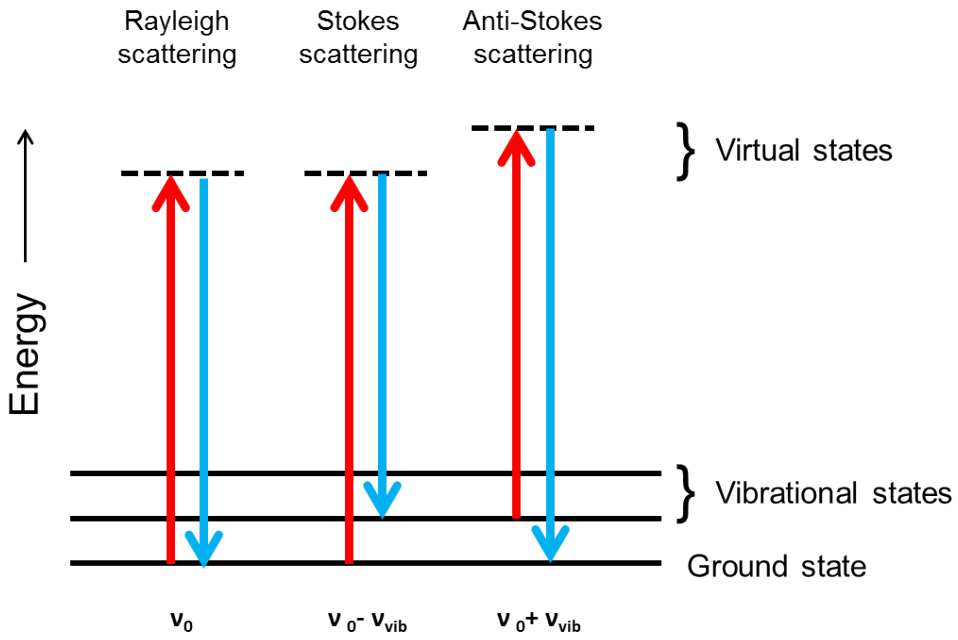

Figure 2.1: Energy level diagram showing the transitions involved in Rayleigh, Stokes and anti-Stokes scattering.

A Raman microscope works by focusing laser light onto a particular spot on a sample. The Stokes- and Rayleigh-scattered photons are collected on a CCD via a diffraction grating, so that the relative intensities of the different frequencies can be measured. A plot of Raman shift (away from the incident laser wavenumber, in cm^{-1}) *vs* intensity conveys quantitative information about the chemical nature and physic-chemical environment of the molecules in the sample.

In previous studies Raman techniques have been used to investigate hygroscopic growth and phase transitions by making use of peak shifts with changing

water to solute ratio and changing peak full width at half maximum (a sharp change in FWHM indicates crystallisation) (Lee *et al.*, 2008). Peak integration can provide quantitative measures of water uptake (Liu *et al.*, 2008; Yeung *et al.*, 2009), assuming peak area is directly proportional to concentration of the related species. Spectra also provide information on metastable crystalline phases and hydrates which form upon efflorescence (Ling & Chan, 2008; Wise *et al.*, 2012). Changes (and lack thereof) in spectral peak positions and FWHMs allow confirmation of the presence of amorphous solids (Liu *et al.*, 2008), and differences in spectra taken at the centre and edge of a particle can indicate any core shell structures (Freedman *et al.*, 2010). The technique has also been used to identify aerosol composition, mixing state and ice nucleation properties (Baustian *et al.*, 2010, 2013, 2012).

The kinetics of water transport in amorphous inorganic aerosol have previously been investigated by Li *et al.* (2011), who used Raman spectroscopy to observe the exchange of deuterium with hydrogen in aqueous magnesium sulphate, but did not determine diffusion coefficients. Ahlqvist & Taylor (2002) also used H/D exchange to observe diffusion in crystalline and amorphous sugars. Zhu *et al.* (2011) determined the diffusion coefficient of water in aqueous maltose solutions as a function of concentration by using Raman spectroscopy and NMR to observe the movement of D_2O. In a similar way, the methods outlined here allow for the quantitative determination of diffusion coefficients in aqueous solutions relevant to atmospheric aerosol over a wide range of RH and temperature conditions, assuming Fickian diffusion.

2.2 The diffusion of water

In order to directly measure water diffusion, a technique was developed which relies upon the observation of the diffusion of D_2O into a disc of aqueous solution. This involves equilibrating the solution at a chosen RH in H_2O vapour and then switching to D_2O vapour of almost the same RH. The progression of D_2O into the solution disc is then monitored as a function of time and distance which allows a quantitative assessment of the diffusion coefficient. The advantage over techniques which involve changing RH in a stepwise fashion is that the solution

to the diffusion equation is greatly simplified since the water content (D_2O + H_2O) of the disc remains constant throughout the experiment - there is no radial solute concentration gradient.

2.2.1 Experimental setup

A Renishaw InVia Raman spectrometer with a 514 nm laser and motorized XYZ stage was coupled to a temperature and relative humidity controlled chamber (fig. 2.2, see Murray *et al.* (2012)). The chamber was formed from a cylindrical piece of Teflon (3 cm in diameter, 1 cm in height) with a hole (0.7 cm or 1.3 cm in diameter, depending on which type of experiment was being performed - the larger diameter was required for the organic diffusion experiments) vertically through the centre. The sample sat at the base of the chamber, sealed with an O-ring. The top of the chamber was sealed with a glass cover slip, held in place with vacuum grease, through which the sample could be viewed and Raman spectra acquired. A dry zero grade N_2 flow was humidified as it passed through a H_2O or D_2O bubbler, whose temperature was regulated by a Haake DC50-K40 chiller, and then diluted to the desired dew point with additional N_2 using two MKS 1179A mass flow controllers. This flow was delivered to the chamber *via* stainless steel piping connecting to a narrow horizontal inlet 0.7 cm from the base. The flow exited the chamber through an identical outlet on the opposite side. The dew point of the outflow from the chamber was recorded using a GE Optica hygrometer with model 1311DR sensor. The stage temperature was maintained using a separate recirculating Julabo ME-F81 chiller and measured using a Fluke 5622 Fast Response PRT Probe, and could be varied between -35 and 50°C. Spectra containing information on the chemical composition of the sample could be continually acquired at predetermined locations on the sample with a laser spot size of 1.3 µm. A 600 lines/mm grating was used, enabling Raman intensities to be simultaneously collected across the wavenumber range of interest. All spectral and environmental data were computer logged for subsequent analysis.

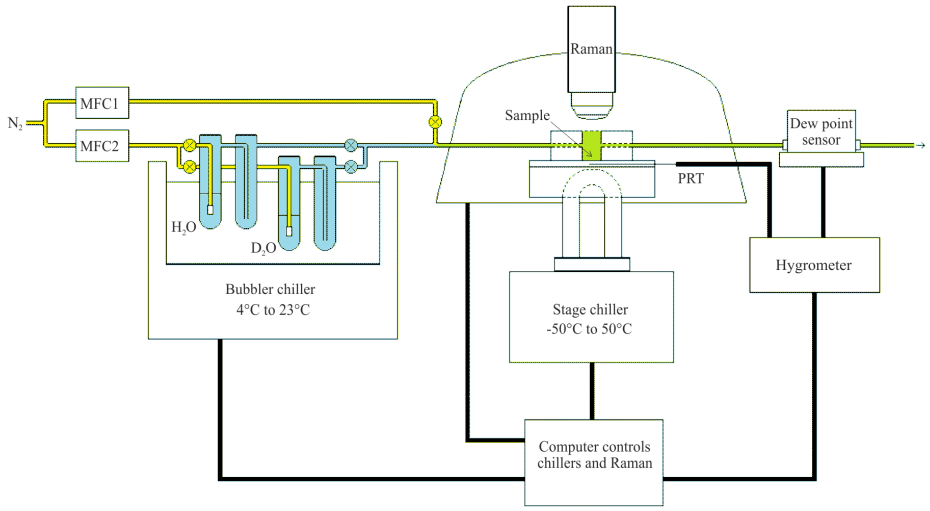

Figure 2.2: Humidity and temperature controlled Raman spectroscopy setup. Nitrogen gas flows were regulated using two mass flow controllers (MFC1 and MFC2) and either remained dry or were humidified in a bubbler. The two flows were mixed at a known ratio to produce the desired relative humidity at the stage, which was also temperature controlled. A hygrometer logged temperature and humidity data.

2.2.2 Diffusion in a disc

The two separate locations of the O-H and the O-D bond stretch bands in the Raman spectrum were used to monitor the diffusion of D_2O from the gas phase into a H_2O solution droplet. As diffusion progressed, O-H bonds were exchanged for O-D bonds, as shown in fig. 2.3. In order to avoid inhomogeneity in the vertical column of sample which contributed to the Raman signal, a disc of solution was prepared such that its circumference (but neither face) was exposed to the surrounding gases (fig. 2.4). In this way, diffusion only occurred horizontally in the radial direction.

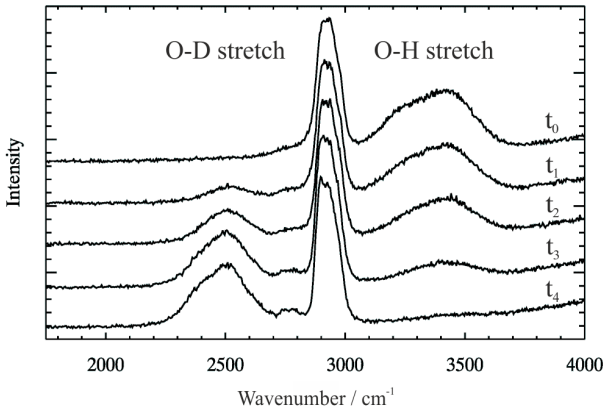

Figure 2.3: Raw Raman data for aqueous sucrose showing the gradual decrease in the O-H stretch (at 3100 to 3500 cm^{-1}) band and increase in the O-D stretch (at 2300 to 2700 cm^{-1}) band as time progessed from t_0 to t_4 after switching from H_2O to D_2O vapour. The central band (at 2800 to 3100 cm^{-1}) is the C-H stretch.

Assuming that a disc is homogenous, i.e. the diffusion coefficient does not depend on radial position, Fick's second law is

$$\frac{\partial \phi(r,t)}{\partial t} = D\nabla^2\phi(r,t) \tag{2.1}$$

where ϕ is the concentration of the diffusing molecule in $mol{\cdot}m^{-3}$, t is time and D is the diffusion coefficient in m^2s^{-1}. A solution to the above equation for a disc

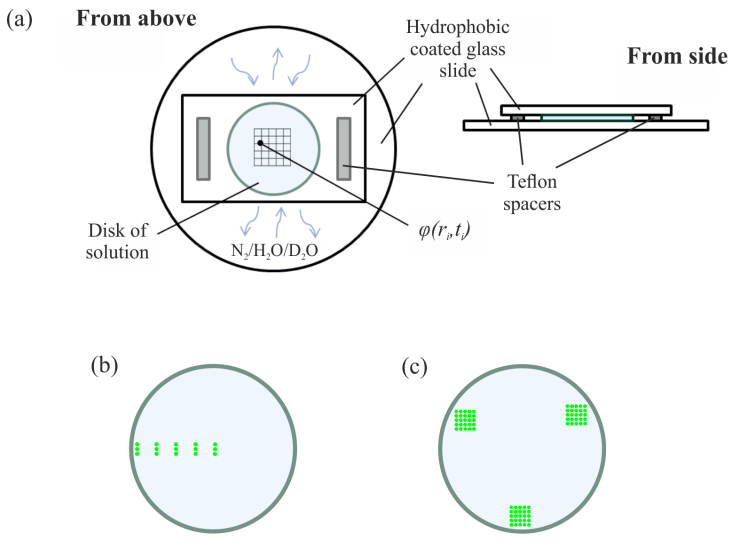

Figure 2.4: (a) Arrangement of a disc on the slide in the D_2O diffusion experiment. The slide was placed in the RH and temperature controlled chamber. A typical disc of solution had a size of around 200–300 µm, and the laser spot had a size of 1.3 µm. The 25 µm thick spacers and top slide were held in place using vacuum grease. Each Raman spectrum was obtained at a predetermined location on a grid, whose size and spacing was chosen to suit the rate of diffusion in each experiment. Other spacer thicknesses were tested to ensure that results were the same and there were no edge effects. (b) Spectral collection configuration for diffusion measurements at high RH. (c) Spectral collection configuration for diffusion measurements at low RH.

of radius a whose edge is maintained at concentration ϕ_0 is

$$\phi(r,t) = \phi_0 + 2(\phi_1 - \phi_0) \sum_{\alpha} \frac{1}{\alpha J_1(\alpha)} e^{\frac{-\alpha^2 Dt}{a^2}} J_0\left(\frac{\alpha r}{a}\right) \tag{2.2}$$

where ϕ_1 is the concentration at $t = 0$ everywhere in the disc except at the edge ($r = a$) at $t = 0$, J_0 and J_1 are Bessels functions of order 0 and 1, respectively, and α are the positive roots of the equation $J_0(x) = 0$ (Bowman, 1958).

2.2.3 Preparation of aqueous solutions

Simple proxies for atmospheric aerosol

Dilute aqueous solutions were prepared with pure water (Milli-Q 18.2 MΩ·cm). The solutes used were sucrose (Sigma, >99.5%), levoglucosan (Acros Organics, >99%), magnesium sulfate (Sigma-Aldrich, >99.5%) and raffinose/M5AS (50 wt% D-(+)-raffinose pentahydrate (Alfa Aesar, >99%), 15.4 wt% malonic acid (Alfa Aesar, >99%), 7.1% maleic acid (Fluka, >99%), 7.4% DL-malic acid (Aldrich, >99%), 3.7% methylsuccinic acid (Aldrich, >99%), 8.9% glutaric acid (Alfa Aesar, >99%) and 7.7% ammonium sulfate (Fluka, >99.5%)).

Secondary organic material

SOM was generated in a flow tube reactor by Yue Zhang at Harvard University, as described by Shrestha *et al.* (2013) and shown in fig. 2.5. The inner diameter of the glass flow tube was 48.2 mm and the length was 1.30 m, operated with a residence time of 38±1 s. The gas flow system and flow tube were surrounded by a temperature-controlled housing which maintained a temperature of 20.0±0.1°C throughout each experiment (this was vital for the reproduction of particle number-diameter distributions between experiments). Ozone was produced by passing 3.0 slpm of pure air through an ozone generator (Jelight, Model 600); α-pinene (Sigma-Aldrich, ≥ 99%) and 2-butanol (Sigma-Aldrich, ≥ 99.5%, used as an OH scavenger) in a ratio of 1:49 were added to the flow tube using a syringe injector (CHEMYX, Fusion Touch 200 Model) and 0.50 slpm of pure air. Ozone concentrations at the inlet were between 12 and 16 ppm, α-pinene concentrations were 6 ppm. The mass concentration at the outlet was 10 mg·m^{-3}, as

measured by a scanning mobility particle sizer. After collection on a quartz filter over 48 to 63 hours, SOM was extracted by ultrasonication using 5.00 ml of ultra-pure water and stored in a refrigerator before being used for this experiment. As noted by Renbaum-Wolff *et al.* (2013), a significant amount (63±27%) of total particle mass can be extracted from filters using water (Hall & Johnston, 2011), and the use of 50:50 methanol:water instead of water for the extraction of similar materials has been shown to make little difference to the extract composition (Heaton *et al.*, 2009).

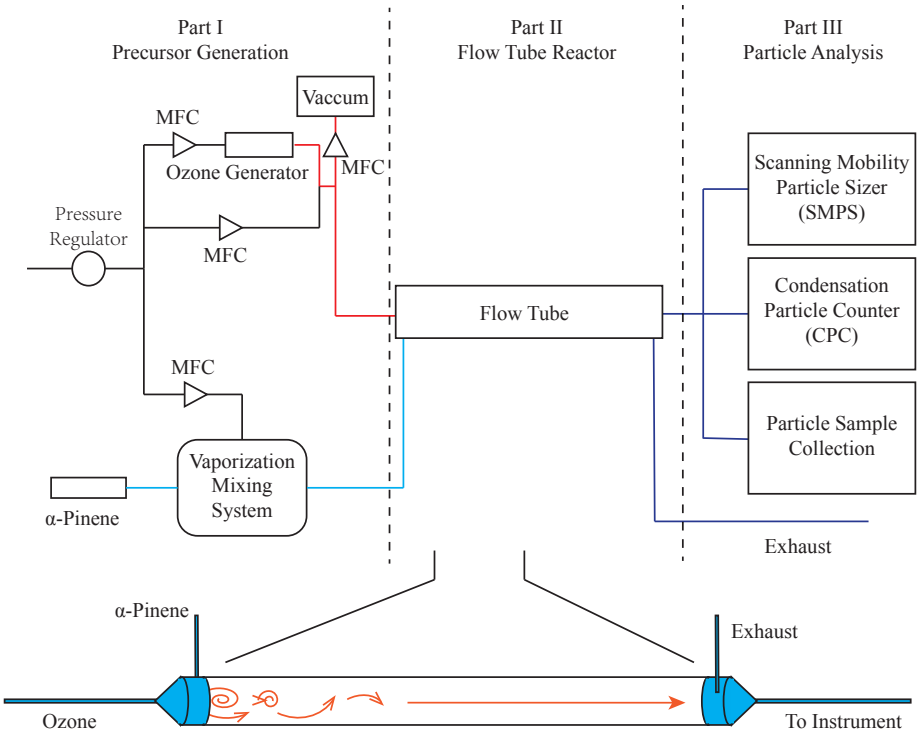

Figure 2.5: Schematic of the flow-tube setup for generating secondary organic aerosol, by Yue Zhang, Harvard.

2.2.4 D_2O diffusion measurements

For each experiment, a ∼0.5 µL droplet of solution was placed on a hydrophobic siliconized glass slide (Hampton Research) using a micropipette and allowed to adapt its size as it started to equilibrate with the surrounding air. Similarly coated glass slides have been used previously and shown not to trigger nucleation (Murray *et al.*, 2012). Once enough water had evaporated to form a concentrated solution droplet, a smaller piece of hydrophobic glass was placed on top of the droplet, supported by a pair of 25 µm-thick Teflon film spacers, in order to create a disc of 200-300 µm radius (fig. 2.4(a)). The slide was then placed in a temperature and humidity controlled chamber, initially at 90% RH.

For each experiment, the solution disc was exposed to a flow of nitrogen gas with a controlled partial pressure of H_2O vapour in order to achieve the water activity corresponding to the chosen RH. In these experiments it was essential that the water activity across the disc was constant, so it was important that the disc was exposed to H_2O vapour for a sufficient period of time. This time required for equilibration depended on solute and RH; the lower the RH, the longer the H_2O equilibration time. Hence, it was necessary to estimate the diffusion coefficient and solute concentrations at a particular water activity so that the time required for equilibration could be estimated using the solution to Fick's second law for a cylindrical geometry (2.2). In this case, ϕ_0 was the water concentration corresponding to the target water activity, and ϕ_1 was the water concentration corresponding to a water activity of 0.9 (i.e. the concentration at the start, defined by the starting RH of 90%). Water concentrations were calculated using relations between water activity and solute mass fraction given in the literature (Ha & Chan, 1999; Lienhard *et al.*, 2012; Wagner *et al.*, 2012; Zobrist *et al.*, 2011), and densities estimated assuming the volume additivity of pure component densities (Tong *et al.*, 2011). The diffusion coefficient used in this estimation was a best initial estimate of the diffusion coefficient of water in the disc at the target water activity, either taken from the literature or based on the trends of previous measurements. By solving 2.2 with these conditions, the time after which the water mass fraction in the centre of the disc corresponded to a water activity within 0.01 of the target water activity could be determined this was used to define the

H_2O exposure time. This process sometimes required several iterations: if the final measured diffusion coefficient was found to be lower than that used in the calculation, the experiment was repeated, this time leaving the disc exposed to H_2O for a longer time period. The equilibration time varied between minutes at high humidity to weeks at low humidity.

In most experiments, equilibration was done at the same temperature as the intended diffusion measurements. However, some of the low temperature or water activity experiments required impractical H_2O exposure times at the measurement temperature, so the sample was equilibrated at an elevated temperature to speed up diffusion. Once the necessary exposure time at this temperature had elapsed, the sample was cooled back to the desired measurement temperature over a period of several hours, with the RH (and thus water activity) kept constant to within 1% RH. Any uncertainty in water activity associated with this procedure is accounted for in error bars. To confirm that this treatment did not alter the diffusion properties of the sample, two measurements of the water diffusion coefficient in sucrose were made at around 80% RH, one before exposure to higher temperatures and one after a week at 50°C. They were in good agreement (see fig. 3.7). Experiments on SOM were not performed above 6°C to avoid changes in the sample (such as browning and an associated increase in fluorescence) which were observed at these temperatures.

To determine disc size and location on the motorized XYZ stage, the positions of three points on the disc's circumference were found. This was done by taking three series of spectra along radial tracks traversing the edge of the particle, with 1 µm spacing between each spectrum and a laser spot size of 1.3 µm. For each of these three spectral series, the points at which peaks originating from the sample first appear in the spectra were used to calculate an upper limit on the disc's radius. Similarly, the three points at which the sample peaks reach their maximum intensity were used to determine a lower limit on the disc's radius. The difference between these upper and lower limits was typically around 20 µm. The best estimate for the disc radius was taken to be the mid-point between the upper and lower limits.

Once the water activity of the disc was estimated to be within 0.01 of $RH/100$, the H_2O vapour was replaced with a flow of D_2O vapour of the same dew-point.

Due to the lower saturation vapour pressure of D_2O, this led to a decrease in RH of up to 1.25% (Matsunaga & Nagashima, 1987). It is estimated that the complete exchange of gases in the pipework and chamber around the solution disc takes 12±2 s, although in a worst-case scenario where the D_2O and H_2O vapours mix only via gas-phase diffusion in the RH-controlled chamber this exchange may take up to 95 s.

The spectrometer was configured to collect Raman spectra after chosen time intervals at locations across a grid covering a portion of the sample disc (see fig. 2.4). The spatial and temporal separations of the spectra were chosen such that, as far as possible, a broad range of D_2O concentrations could be observed over the entire disc radius during the experiment. Each spectrum was measured at a new XY coordinate (and hence radial position), chosen according to the rate of diffusion in each experiment. The vertical position of the focal point was approximately half-way between the two hydrophobic glass slides (test were performed to verify that the measured diffusion coefficients did not vary across the depth of the sample). The D_2O exposure time required to collect enough information to determine a diffusion coefficient was about 10 minutes for a D_{water} of 10^{-10} m^2s^{-1}, about 2 hours for a D_{water} of 10^{-12} m^2s^{-1}, about 20 hours for a D_{water} of 10^{-14} m^2s^{-1}, and about 8 days for a D_{water} of 10^{-16} m^2s^{-1}.

The Raman software could be used to define a rectangular grid across which spectra could be collected in a raster fashion. At high diffusion coefficients, it was important to collect data across the entire radius of the disc in a short space of time. For this reason, a grid such as that shown in fig. 2.4(b) was configured, with a 25 µm spacing in the x direction and a small (up to 5 µm) spacing in the y direction. Limitations existed at low RH because diffusion was so slow as to make it impractical to wait for high D_2O concentrations at the disc centre; it was nevertheless possible to determine diffusion coefficients using the concentration measurements near the edge of the disc (see fig. 2.4 (c)). At these slow diffusion coefficients, where many spectra could be collected without the concentration gradient changing significantly, it was less important to cover the entire radius of the disc in a short space of time. This allowed for the collection of clusters of more spectra at higher spatial resolution (typically with x and y spacing of 5 µm), with time breaks between each cluster (fig. 2.4(c)). As diffusion progressed,

and the O-D band was visible across greater proportions of the radius, the spread and number of spectra in each cluster was increased to cover more of the radius.

The time taken to collect each spectrum was typically 1 s, with a further 1 s period required between spectra for the motorized XYZ stage to move to the next location. This therefore defined the upper limit to the diffusion coefficients which could be measured where diffusion occurred on a minute timescale. Some spectra were longer in duration (up to 40 s per spectrum); these longer acquisitions were used where the extra duration did not compromise the time resolution, but did improve the quality of the spectral data. For very slow experiments (e.g. sucrose 20% RH, which involved a 3 week D_2O exposure), there were breaks between several series of spectral acquisitions in order to avoid wear on the laser. The number of points used in each surface fit varied according to the duration of each experiment, which was directly influenced by the rate of diffusion at each relative humidity. Experiments where diffusion coefficients were large typically involved the collection of several hundred spectra (and thus data points in the surface fit); experiments with the smallest diffusion coefficients usually generated several thousand spectra.

After the exchange had taken place, the process of determining the disc radius by finding the positions of three points on the disc edge was repeated. Decreases in radius of up to 3% were noted; this can be accounted for by the combined effects of a change in molar volume due to isotope exchange (Bartell & Roskos, 1966), and a change in water activity due to the lower saturation vapour pressure of D_2O (Matsunaga & Nagashima, 1987). The shrinkage was included in the calculation of the error bars associated with each data point.

Raffinose/M5AS was seen to fluoresce at the lowest water activity investigated (0.22), which meant the Raman scattering bands were partially obscured (no significant fluorescence was oberved at other humidities or in the other samples). To minimise these effects, the Raman laser was used to photobleach the sample for 500 s prior to each spectral acquisition. Since any photobleaching-induced effects would have been concentrated in a small area due to the small laser spot size, and given that each spectrum was aquired in a new position, it is not expected that there are any effects on the determined diffusion properties from the bleaching technique.

2.3 Diffusion of organics

Large organic molecules are expected to diffuse more slowly in aqueous solutions than small molecules such as water. To measure the diffusion coefficient of sucrose molecules in aqueous solution, a Raman isotope tracer method was again employed, very similar to that described by Zhu *et al.* (2011). The diffusion of sucrose molecules across a boundary between aqueous solutions of deuterated and non-deuterated sucrose was monitored by virtue of the differing wavenumber locations of the C-D and C-H Raman stretch bands.

2.3.1 Diffusion across a plane interface

Assuming the boundary between the deuterated and non-deuterated solutions can be treated as a semi-infinite plane at $x = 0$, the intensities of the C-H band, I_h, is described by (Jost, 1960; Zhu *et al.*, 2011):

$$I_h(x) = \frac{1}{2} I_{h0} \left(1 + \mathrm{erf} \left(\frac{x}{\sqrt{2}\sigma} \right) \right) \tag{2.3}$$

where I_{h0} is the intensity of the C-H stretch in aqueous non-deuterated sucrose and σ describes the width of the interface broadened by diffusion. Similarly,

$$I_d(x) = \frac{1}{2} I_{d0} \left(1 + \mathrm{erf} \left(\frac{x}{\sqrt{2}\sigma} \right) \right) \tag{2.4}$$

where I_{d0} is the intensity of the C-D stretch in aqueous deuterated sucrose.

2.3.2 Experimental setup

33 wt% aqueous solutions of sucrose (Sigma, > 99.5%) and deuterated sucrose (β-D-[UL-$^2H_7$]fructofuranosyl α-D-[UL-$^2H_7$]glucopyranoside, Omicron Biochemicals, see fig. 2.6) were made using Milli-Q (18.2 MΩ·cm) pure water. A droplet of each solution was placed on a hydrophobic siliconised glass slide (Hampton Research) using a micropipette, and put in the RH and temperature controlled cell in the Raman microscope system. The droplets were then allowed to equilibrate with the surrounding water vapour. The time taken for equilibration was calculated using the water diffusion coefficients (chapter 3) together with the multi-shell sucrose

diffusion model (see chapter 5). At RHs below 50%, this step was performed at an elevated temperature (up to 36°C) to speed up equilibration time (see section 2.2.4).

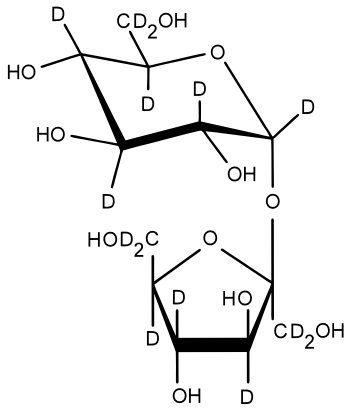

Figure 2.6: Structure of deuterated sucrose.

Once a uniform water activity across each droplet radius had been achieved, the RH controlled cell was briefly opened, with the humidified N_2 still flowing, to allow a second hydrophobic siliconised glass slide to be place on top of the droplets. This slide was prepared by placing several squares of double-sided adhesive tape around its edge to act as spacers and prevent slippage. By applying a small amount of force to this top slide, the two droplets were compressed and made contact, as shown in fig. 2.7.

Raman measurements were made to monitor the progress of sucrose (both non-deuterated and deuterated) diffusion across the boundary. The high-wavenumber Raman spectrum of non-deuterated aqueous sucrose features an O-H stretch band at ∼3100 to 3500 cm^{-1}, and a C-H stretch band at ∼2800 to 3100 cm^{-1}. The spectrum of deuterated aqueous sucrose lacks the C-H stretch band, and instead has a C-D band at ∼2000 to 2300 cm^{-1}. Five Raman spectra taken along a track traversing the boundary between the deuterated and non-deuterated are shown in fig. 2.8, with the decrease in C-H and increase in C-D bands clearly visible.

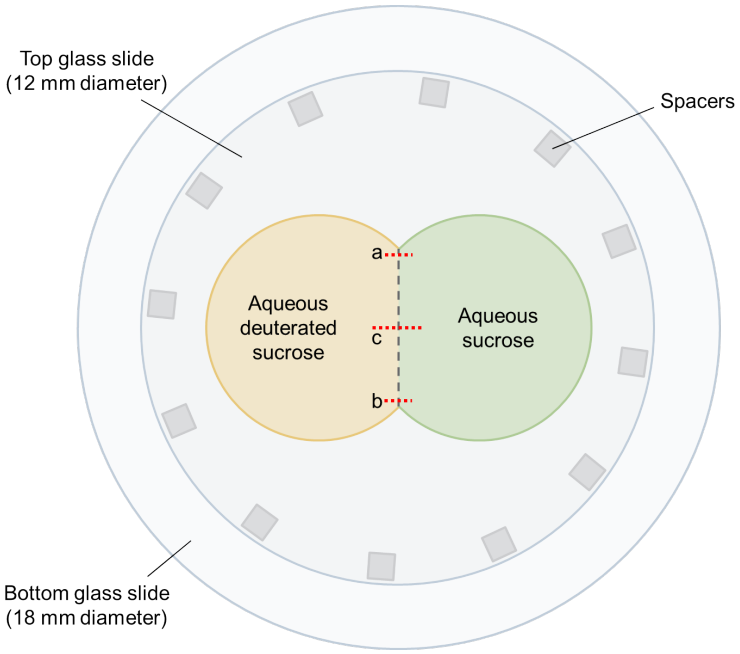

Figure 2.7: Setup used for measuring sucrose diffusion in aqueous sucrose solutions. The top glass slide causes the two droplets (one non-deuterated sucrose, the other deuterated sucrose) to make contact, and is held in place by spacers.

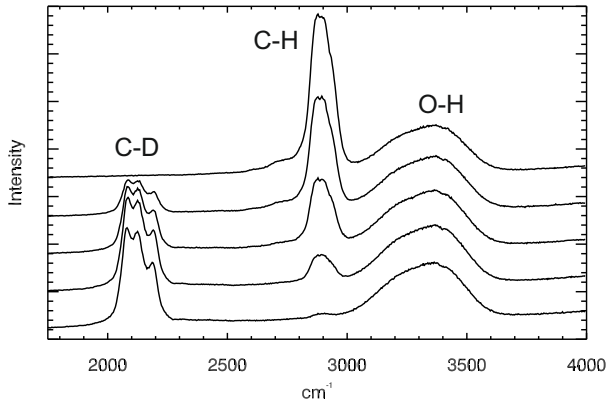

Figure 2.8: Raw Raman data for aqueous sucrose showing the gradual decrease in the C-H stretch (at 3800 to 3100 cm^{-1}) band and increase in the O-D stretch (at 2000 to 2300 cm^{-1}) band as the Raman laser traces a path across the boundary between the deuterated and non-deuterated sucrose droplets. The unchanging band at 3100 to 3600 cm^{-1} is the O-H stretch.

To use equations 2.3 and 2.4 to determine the diffusion coefficient of sucrose, it was necessary to make Raman measurements along a perpendicular bisector to the boundary between the different solutions. To determine the location of this line, two short series of spectra were taken at either end of the boundary, marked as (a) and (b) in fig. 2.7. The points at which the C-H and C-D intensities were the same in each of these series were used to find the location of the boundary, and trigonometry was used to determine the position of the perpendicular bisector, marked as (c) in fig. 2.7. A series of spectra were acquired along this line with a spatial separation and acquisition time chosen such that the duration of the collection of this series was short in comparison to the diffusion timescale.

Chapter 3

Water diffusion in simple proxies for atmospheric aerosol

The new isotope tracer technique for measuring water diffusion described in section 2.2 is here applied to simple aqueous solutions. These solutions can be seen as proxies for atmospheric aerosol, and have been widely studied in previous literature allowing for direct comparison. Sucrose, in particular, has been the subject of several diffusion studies, which allows for the verification of the technique. Bounce factor data are available for levoglucosan, whilst raffinose/M5AS (a mixture of raffinose, five carboxylic acids and ammonium sulphate) has been used to represent mixed tropospheric aerosol in ice nucleation studies. Magnesium sulphate has the interesting property of gel formation at low relative humidity, and represents a significant component of seawater aerosol. Knowledge of the water diffusion coefficients in these materials will therefore provide valuable insights into the possible behaviour of aqueous solutions in the atmosphere as well as providing an opportunity to test and validate the experimental system.

3.1 Analysis of Raman data to determine O-D concentration

The Raman spectra of aqueous solutions of organics such as sucrose and levoglucosan are characterized at high wavenumbers by C-H stretch bands at ∼2800

to 3100 cm^{-1} and O-H stretch bands at ~3100 to 3500 cm^{-1} (see, for example, the top spectrum of fig. 2.3). The C-H stretch band originates entirely from the organic molecules, whilst the O-H band originates from hydroxyl groups both in the organic and in water. The magnesium sulfate spectrum lacks the C-H stretch, whilst the raffinose/M5AS spectrum also features a band arising from the NH_4^+ species which is situated around 3100 cm^{-1}. This band was small (due to the relatively small amount of ammonium in the mixture) and overlapped with the O-H stretch. The O-D stretch band is located at ~2500 cm^{-1}, which is $1/\sqrt{2}$ times the O-H stretch frequency, and has a lower integrated intensity than the O-H stretch band by a factor of $1/\sqrt{2}$ (Kohen & Limbach, 2005). Similarly, the ND_4^+ band is located at ~2200 cm^{-1}. After switching from H_2O vapour to D_2O flow, the O-H stretch band decreased in area, whilst the O-D band appeared and grew (fig. 2.3). In raffinose/M5AS, the NH_4^+ band was also seen to decrease whilst the ND_4^+ band grew. The area of the C-H stretch band did not decrease: hydrogen atoms on oxygen or nitrogen may exchange with deuterium due to the polarisation of the electron density within the bond, whilst C-H bonds do not exchange as they are not sufficiently polarised.

Using the Levenberg-Marquardt technique (Markwardt, 2009), a set of Gaussian peaks were fitted to the spectral bands. The background was accounted for using a constant plus a broad, high frequency Gaussian which smoothly matched the low and high frequency ends of the spectra. It should be emphasized that the spectral fits produced here are not intended as accurate band assignments. The sole purpose is to achieve a reasonable, background-corrected quantification of the relative integrated band intensities of the broad O-H and O-D bands.

The spectral data and fitted Gaussian peaks for sucrose, levoglucosan, raffinose/M5AS and magnesium sulfate are shown in figs. 3.1 to 3.4. For sucrose, levoglucosan and raffinose/M5AS, the parameters describing these Gaussian functions (i.e. peak height, width and wavenumber) were constrained so that variable intensity peaks were fitted to the O-H, NH_4^+, O-D and ND_4^+ bands, and fixed intensity peaks were fitted to the C-H band. A satisfactory fit with a reduced χ^2 value close to 1 was achieved by fitting up to three Gaussians to the O-H band (or the combined O-H and NH_4^+ bands in the case of raffinose/M5AS), up to three Gaussians to the O-D band (or the combined O-D and ND_4^+ bands in the case of

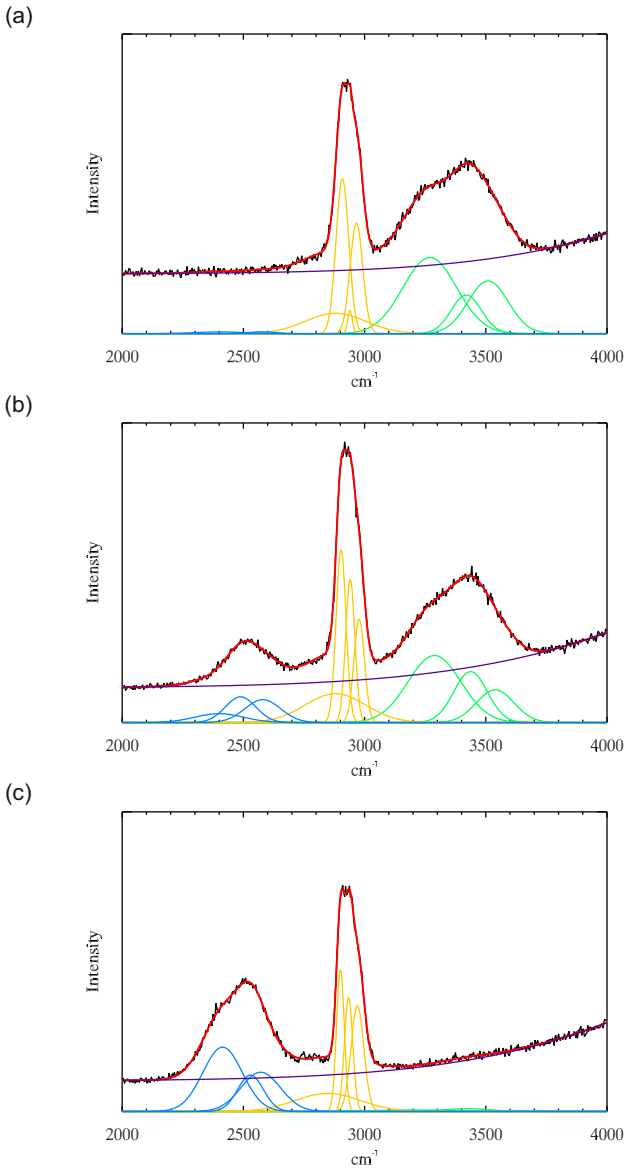

Figure 3.1: Example fits to the Raman spectra of sucrose. Raw data are shown in black, green peaks are fitted to the O-H stretch, blue peaks are fitted to the O-D stretch, orange peaks are fitted to the C-H stretch, and the background fit is shown in purple. The sum of all fitted peaks is shown in red. Green and blue peaks were allowed to vary as H/D exchange took place; orange peaks were more tightly constrained. (a) A spectrum taken before the switch to D_2O. (b) A spectrum taken during H/D exchange. (c) A spectrum taken after H_2O had been replaced by D_2O.

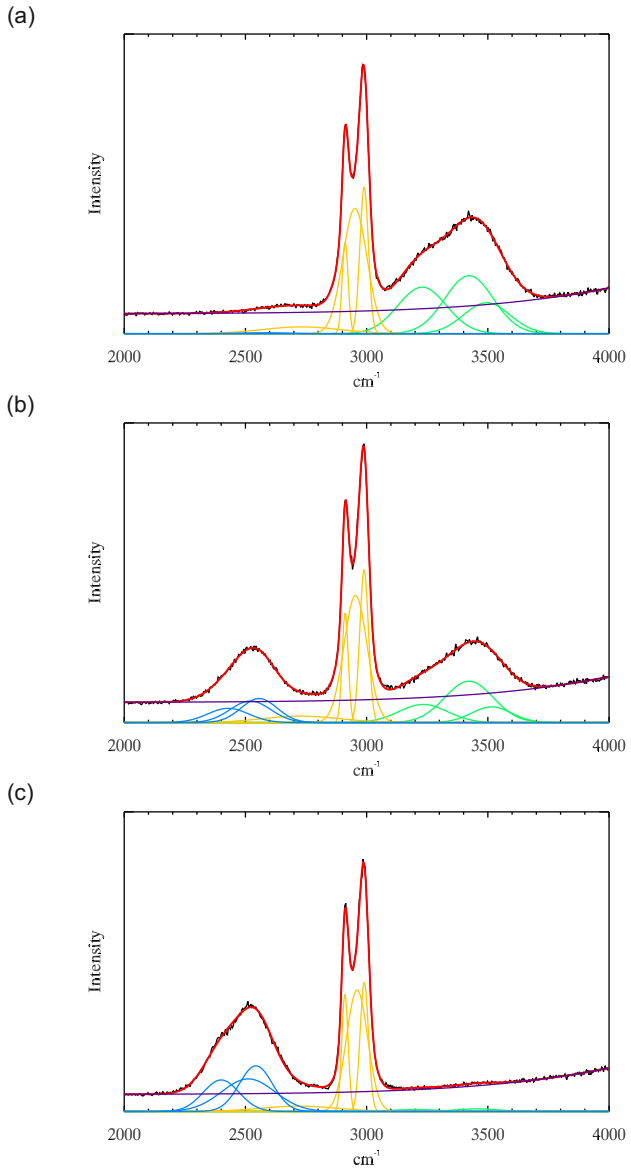

Figure 3.2: Example fits to the Raman spectra of levoglucosan. Raw data are shown in black, green peaks are fitted to the O-H stretch, blue peaks are fitted to the O-D stretch, orange peaks are fitted to the C-H stretch, and the background fit is shown in purple. The sum of all fitted peaks is shown in red. Green and blue peaks were allowed to vary as H/D exchange took place; orange peaks were more tightly constrained. (a) A spectrum taken before the switch to D_2O. (b) A spectrum taken during H/D exchange. (c) A spectrum taken after H_2O had been replaced by D_2O.

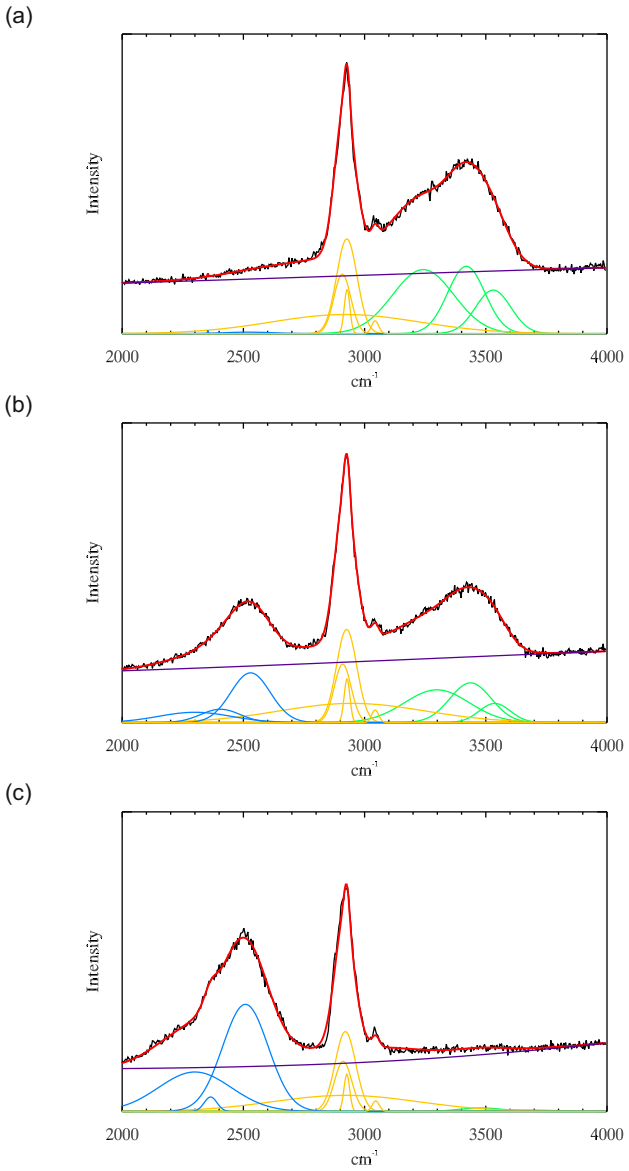

Figure 3.3: Example fits to the Raman spectra of raffinose/M5AS. Raw data are shown in black, green peaks are fitted to the O-H and NH_4^+ stretch, blue peaks are fitted to the O-D and ND_4^+ stretch, orange peaks are fitted to the C-H stretch, and the background fit is shown in purple. The sum of all fitted peaks is shown in red. Green and blue peaks were allowed to vary as H/D exchange took place; orange peaks were more tightly constrained. (a) A spectrum taken before the switch to D_2O. (b) A spectrum taken during H/D exchange. (c) A spectrum taken after H_2O had been replaced by D_2O.

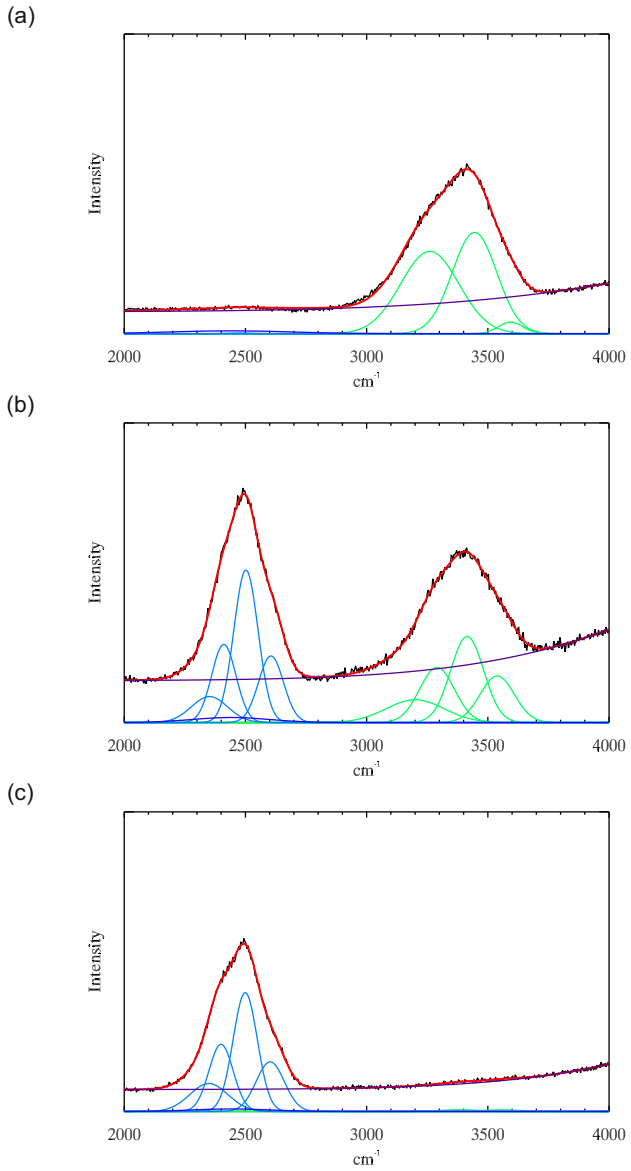

Figure 3.4: Example fits to the Raman spectra of $MgSO_4$. Raw data are shown in black, green peaks are fitted to the O-H stretch, blue peaks are fitted to the O-D stretch, and the background fit is shown in purple. The sum of all fitted peaks is shown in red. Green and blue peaks were allowed to vary as H/D exchange took place. (a) A spectrum taken before the switch to D_2O. (b) A spectrum taken during H/D exchange. (c) A spectrum taken after H_2O had been replaced by D_2O.

raffinose/M5AS), and up to five Gaussians to the C-H band. Constraining the parameters describing these peaks was particularly important in the overlap region between the O-D and C-H bands. So that no C-H intensity was attributed to O-D vibrations, the C-H stretch bands were initially fitted before any D_2O exposure. As the C-H band would not vary during the experiment, the parameters found in this initial fit to the corresponding Gaussian peaks were used to constrain the C-H band fit when D_2O was present. For magnesium sulfate (fig. 3.4), up to four Gaussians were fitted to the O-H stretch and up to four to the O-D stretch, as well as a weak Gaussian to account for a slightly raised background at ∼2450 cm^{-1}.

3.1.1 Obtaining the water diffusion coefficient

The results of the spectral fitting procedures were used with equation 3.1 to find the diffusion coefficient of D_2O in the sample. Unlike in section 2.2.4, ϕ is now the D_2O concentration. Because the total amount of water (D_2O plus H_2O) and solute remains constant throughout the experiment, ϕ can simply be written as the fractional concentration of O-D bonds relative to the total O-D and O-H bonds at each spectral location and time. Thus,

$$\phi = \frac{A_{OD}}{A_{OD} + \frac{1}{\sqrt{2}} A_{OH}} \tag{3.1}$$

where A_{OD} is the integrated intensity of the O-D stretch (i.e. the summed areas of the Gaussian curves representing the broad band between 2300 cm^{-1} and 2700 cm^{-1}) and A_{OH} is the integrated intensity of the O-H stretch (i.e. the summed areas of the Gaussian curves representing the broad band between 3100 cm^{-1} and 3500 cm^{-1}). The progression of ϕ with time at fixed radial positions is shown in fig. 3.5.

To determine D_{water} at a given RH, a surface fit of equation 2.2 with the diffusion coefficient as a variable parameter is performed to the measured values of $\phi(r,t)$, again using the Levenberg-Marquardt technique. ϕ_0 is set to 1 (the fractional O-D concentration maintained at the edge of the disc) and ϕ_1 is here set to 0 (the O-D concentration everywhere except the edge at t=0).

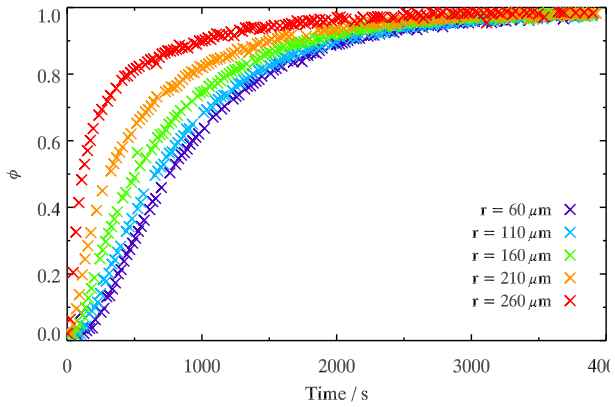

Figure 3.5: Fractional concentration of O-D bonds, ϕ, as a function of time after switch from H_2O to D_2O vapour in a 278 µm (radius) levoglucosan disc at 60% RH. Colours indicate radial distance (where $r = 0$ µm is the centre of the disc): red data points are near the edge, blue are near the centre. This was a one-off experiment in which data were repeatedly collected at five specific radial positions, for the purpose of visualising how concentration changed at a fixed location over time.

Figure 3.6 shows examples of the surface fit to a set of data for aqueous (a) sucrose, (b) levoglucosan and (c) raffinose/M5AS, where each measured data point is connected to the fitted surface by a black line for comparison, and fig. 3.6(d), (e) and (f) show the corresponding fit *vs* measurement plots. Due to the finite size of the laser spot (estimated by the manufacturers as 1.3 µm), measured values of ϕ are least reliable where the radial concentration gradient is changing rapidly.

It is evident from the complete disappearance of the O-H stretch band in figs. 2.3 and 3.1 to 3.3 that H/D exchange occurs not only in the water molecules of the sample, but also in the hydroxyl groups of the organics. A large difference between the rates of these two exchanges would complicate the determination of the diffusion coefficient. However, at 90% RH, complete H/D exchange at the centre of a disc was observed on the timescale of minutes. Given that measurements at RHs lower than ∼70% took significantly longer than this, and that the calculated diffusion coefficients were several orders of magnitude lower, it is concluded that the limiting step here is diffusion, not H/D exchange rate. It is noted, however, that for measurements between 70 and 90% RH the procedure may introduce some uncertainty. The determined diffusion coefficient above 70% RH may thus be slightly lower than the true value.

3.2 Measured diffusion coefficients in sucrose, levoglucosan, magnesium sulfate and raffinose/M5AS

The determined diffusion coefficients of D_2O in sucrose, levoglucosan, magnesium sulfate and raffinose/M5AS as a function of water activity, at 23.5°C, are shown in fig. 3.7. The upper error bars shown for D_{water} represent the value of D_{water} calculated using the highest value measured for the upper limit on the disc's radius (usually that calculated from the three edge measurements before exposure to D_2O vapour), with a time delay of 95 s, and include the random error in the surface fit due to errors in ϕ. The lower error bars shown for D_{water} represent the value of D_{water} calculated using the lowest value measured for lower limit on the disc's radius (usually that calculated from the three edge measurements after

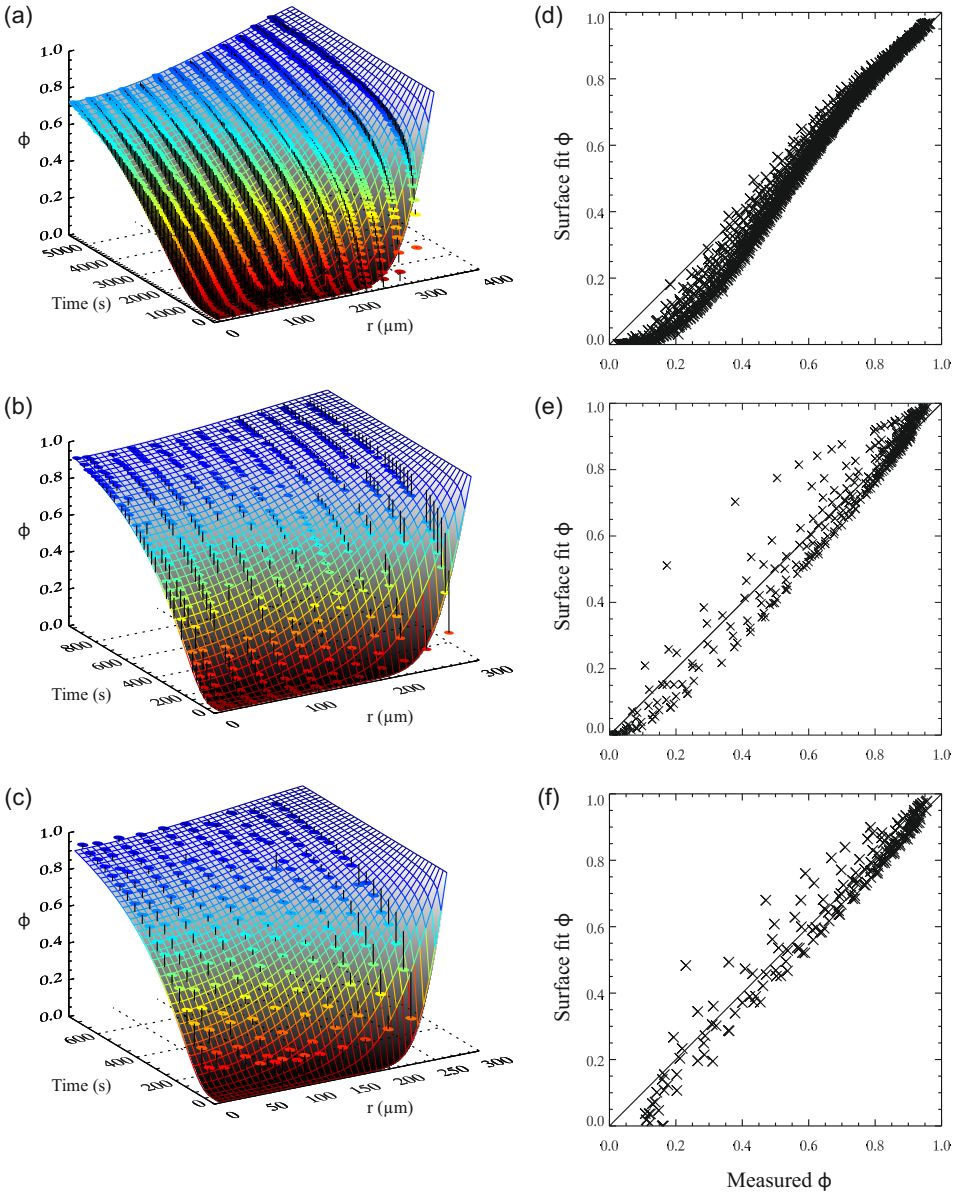

Figure 3.6: (a), (b) and (c) Plots of the fractional concentration of O-D bonds, ϕ, as a function of radial distance and time after switch from H_2O to D_2O vapour in aqueous solution discs at 70% RH, for sucrose, levoglucosan and raffose/M5AS, respectively. The grid shows the surface fit to the data, the collected data points are joined to the grid by black lines. The colour corresponds to the value of ϕ. (d), (e) and (f) One-to-one plots showing the measured ϕ *vs.* ϕ according to the fit, again for sucrose, levoglucosan and raffose/M5AS, respectively.

exposure to D_2O vapour), with a time delay of 10 s, and also include the random error in the surface fit due to errors in ϕ. Lines are fitted to the data as follows:

$$\log_{10} D = a + ba_w + ca_w^2 + da_w^3 \tag{3.2}$$

where a, b, c and d are empirically fitted parameters detailed in table 3.1. The fits for all substances converge to the diffusion coefficient for water in water at a water activity of 1.0 (Holz *et al.*, 2000).

Table 3.1: Fit parameters a to d used in equation 3.2 for $D_{water}(a_w)$.

	a	b	c	d
Sucrose	-20.89	25.92	-26.97	13.25
Levoglucosan	-18.41	31.10	-44.43	23.12
Raffinose/M5AS	-17.21	24.00	-32.50	17.02

The diffusion of D_2O is expected to be slightly slower than that of H_2O. As a guide, the ratio of the self-diffusion coefficients of H_2O and D_2O have been found to lie in the range 1.10 to 1.25 (Liu & Macedo, 1995; Mills, 1973; Svishchev & Kusalik, 1994). However, given that the measured values cover six orders of magnitude, the diffusion coefficient of D_2O can be taken as a good approximation for that of H_2O.

3.3 Sucrose - comparison with literature data

The diffusion coefficients of water in aqueous sucrose solutions are compared to literature data in fig. 3.8 and are in good agreement for water activities between 0.5 and 0.7. Below a water activity of 0.5, where the He *et al.* (2006) and Zobrist *et al.* (2011) parameterisations deviate from each other, the fit to the data measured here lies between the available literature values, but seems to follow the trend of the free-volume model (He *et al.*, 2006). This is consistent with the observation by Tong *et al.* (2011) that the diffusion coefficient reported by Zobrist *et al.* (2011) for a 95% sucrose solution (a water activity of 0.28) is too large to explain their observed droplet size changes.

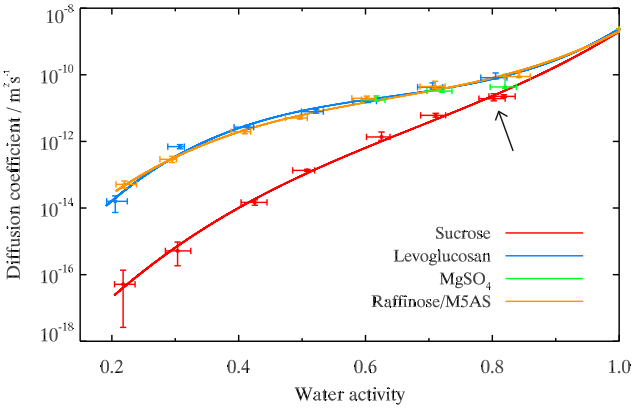

Figure 3.7: Measured water diffusion coefficients of sucrose, levoglucosan, magnesium sulfate and raffinose/M5AS. Lines are fitted to the data with an empirical polynomial fit (equation 3.2). The arrow indicates a measurement performed on a sucrose disc which had previously been held at 50°C for a week. It is inferred from the fact that this data point agrees well with its neighbour that equilibrating the samples at high temperatures does not alter their diffusion properties.

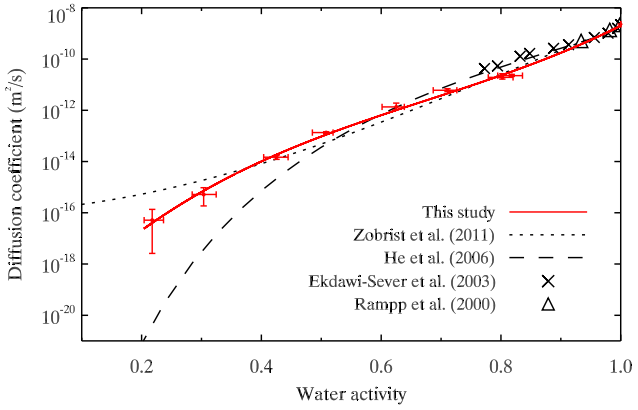

Figure 3.8: Measured diffusion coefficients of water in aqueous sucrose solutions, with comparison to the parameterisations for sucrose solutions given in Zobrist *et al.* (2011) and He *et al.* (2006), and the NMR measurements of Ekdawi-Sever *et al.* (2003) and Rampp *et al.* (2000).

At a water activity of 0.8, the water diffusion coefficients measured in this study are around half an order of magnitude lower than those measured by Ekdawi-Sever *et al.* (2003) and predicted by He *et al.* (2006). These deviations from literature values at high water activities may be due to a number of factors. When diffusion is fast, the radial progression of the concentration gradient may be limited by something other than water diffusion, possibly the slower H/D exchange in hydroxyl groups (as discussed in section 3.1.1). The fractional concentration of O-D bonds (relative to the total O-D plus O-H bonds) in the gas phase at the edge of the disc cannot instantaneously become 1 when the switch is made from H_2O to D_2O. There will be an unavoidable period of time in which a mixture of H_2O and D_2O vapours is present; the nearer the duration of this switchover is to the timescale of the measurement, the more likely it is to lead to errors.

3.4 Timescales for water diffusion

The characteristic half-time for diffusion into a spherical particle of radius at constant water activity is given by (Seinfeld & Pandis, 2012):

$$\tau_{\frac{1}{2}} = \frac{r^2}{\pi^2 D \cdot \ln 2} \tag{3.3}$$

Note that this is the diffusion timescale for water diffusing into a droplet at constant water activity and therefore D does not change. It may be of interest to know the timescales over which a droplet would respond to changes in RH under certain atmospheric circumstances. This is not a simple calculation due to the plasticising effect of water in these aqueous solutions - the diffusion coefficient is a function of concentration and would vary radially as a droplet increased or decreased in size. In order to model the response of a droplet to a change in humidity a model of the time response of a droplet undergoing water uptake and loss is required. This will be discussed in chapter 5. For now, τ is used to give basic information about the rate at which water molecules diffuse within a droplet at a given relative humidity.

Figure 3.9(a) shows these timescales for water diffusing into sucrose, levoglucosan and raffinose/M5AS aqueous spherical droplets of radii between 100 nm

and 1 mm at 20% RH. For levoglucosan and raffinose/M5AS, water diffusion timescales are faster than 1 s in particles smaller than 250 nm in radius at room temperature. For sucrose these timescales are on the order of minutes to hours. Under these conditions the calorimetry data presented by Zobrist *et al.* (2008) suggest that aqueous sucrose exists in a glassy state. As Zobrist *et al.* (2011) point out, even though particles may exist in what is by definition a glassy state, water diffusion is not necessarily arrested. Nevertheless, the kinetic limitation could be important for growth measurements in aerosol instruments which operate on short timescales, such as the HTDMA (Hersey *et al.*, 2013). In addition, diffusion coefficients decrease with temperature and thus under common atmospheric conditions these timescales are expected to be far greater.

Water diffusion coefficients measured in this study have been used to calculate water diffusion timescales as a function of RH in droplet of 100 nm radius, according to equation 3.3; these are plotted as red dots in fig. 3.9(b). These timescales have also been calculated using the water diffusion coefficients given in Zobrist *et al.* (2011) for comparison. To illustrate the magnitude of error that would be encountered when estimating these water diffusion timescales from a viscosity measurement, the Stokes-Einstein relation (equation 3.2) was used with the viscosity measurements of Power *et al.* (2013) to estimate D in equation 3.3. The resulting timescales are shown as black crosses. There is a discrepancy of more than 5 orders of magnitude between the two datasets at ∼30% RH and ∼2 orders at 62% RH. Again, this demonstrates the importance of quantifying diffusion in atmospheric aerosol.

3.5 Comparison between rebound and diffusion timescales in sucrose and levoglucosan

Diffusion coefficients of water in levoglucosan were found to be significantly higher than those in sucrose for the same RH, and correspond to diffusion in a high-viscosity liquid. This is consistent with the glass transition curve given by Lienhard *et al.* (2012) which shows that the glass transition temperatures of aqueous levoglucosan solutions of water activities above 0.2 are below 236 K.

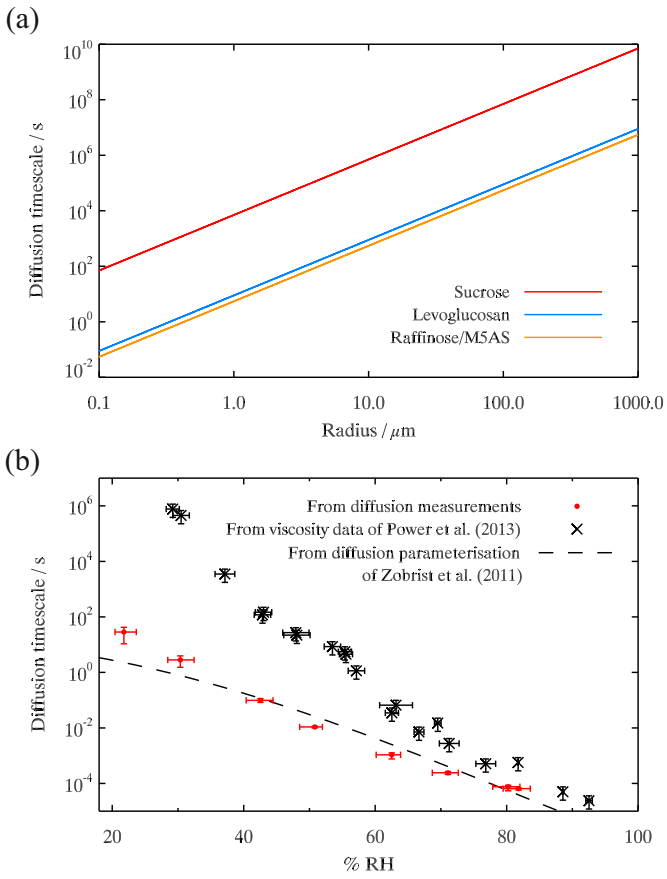

Figure 3.9: (a) Water diffusion timescales as a function of radius for spherical droplets at 20% RH, calculated according to equation 3.3. Sucrose is shown in red, levoglucosan in blue and raffinose/M5AS in orange. (b) Water diffusion timescales equation 3.3) as a function of relative humidity for 100 nm particles. Red dots show timescales calculated using water diffusion coefficients measured in this study, the dashed black line shows these timescales using the water diffusion coefficient parameterization given in Zobrist *et al.* (2011). Black crosses are calculated using the Stokes-Einstein relation with viscosity data from Power *et al.* (2013) (error bars correspond to a water molecular diameter uncertainty of 0.2±0.1 nm).

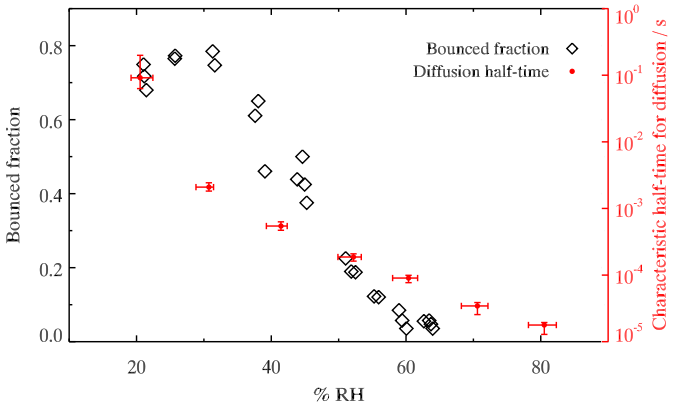

Figure 3.10: Characteristic timescales for diffusion of D_2O in 100 nm aqueous levoglucosan aerosol particles (red dots), compared with bounce fraction data from Saukko *et al.* (2012b) (black diamonds).

Saukko *et al.* (2012b) determined the rebound fraction of aqueous levoglucosan aerosol by impacting the aerosol onto a substrate and counting the number of particles which bounced; a high bounce fraction is considered to indicate high viscosity, whilst a low bounce fraction implies low viscosity. As noted by Saukko *et al.* (2012b), high-viscosity liquids and semi-solids have similar rebound behaviour to glasses and crystalline solids: bounce fractions of around 0.8 were measured for both high-viscosity liquid levoglucosan and crystalline ammonium sulfate. Figure 3.10 shows diffusion half-lives of 100 nm radius levoglucosan droplets as a function of water activity, as calculated using equation 3.3, compared with bounce fraction data. Even at low RH, this characteristic timescale for diffusion in levoglucosan is less than 0.1 s. Zobrist *et al.* (2011) measured water diffusion coefficients in glassy particles (which would presumably have similarly high bounce fractions to low RH levoglucosan) as low as 10^{-24} m^2s^{-1}, which, according to equation 3.3, would have diffusion half-lives of over 100 years.

Bateman *et al.* (2014b) also measured particle rebound for a variety of materials including sucrose, using a different set of impaction apparatus to Saukko *et al.* (2012b). Figure 3.11 shows the diffusion half-lives for aqueous sucrose particles of 100 nm radius, as calculated using equation 3.3, compared with the rebound

data. It can be seen that where there is a sharp transiton in rebound data at around 75% RH, there is no such abrupt change in water diffusion timescale. Between 30 and 60% RH there is little change in rebound fraction, whilst the diffusion timescale varies over nearly four orders of magnitude. Below 30% RH, though, the rebound fraction increases above 1, which the authors attribute to the shattering of particles upon impaction. This RH approximately corresponds to the point at which aqueous sucrose undergoes the glass transition (Zobrist *et al.*, 2008).

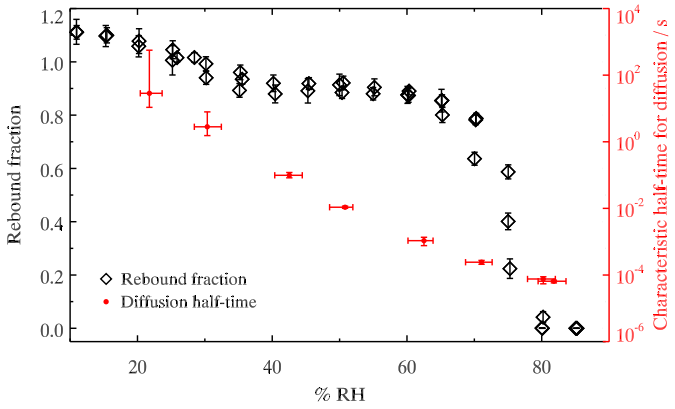

Figure 3.11: Characteristic timescales for diffusion of D_2O in 100 nm aqueous sucrose aerosol particles (red dots), compared with rebound fraction data from Bateman *et al.* (2014b) (black diamonds).

These comparisons reiterate what is already accepted about rebound measurements: although rebound fractions are useful in determining particle phase in the relevant size range, they alone cannot yet distinguish between particles in which diffusion of a small molecule such as water occurs on timescales of milliseconds and those in which it takes years (Saukko *et al.*, 2012b). This underlines the importance of quantitative diffusion measurements for the understanding of high-viscosity atmospheric aerosol.

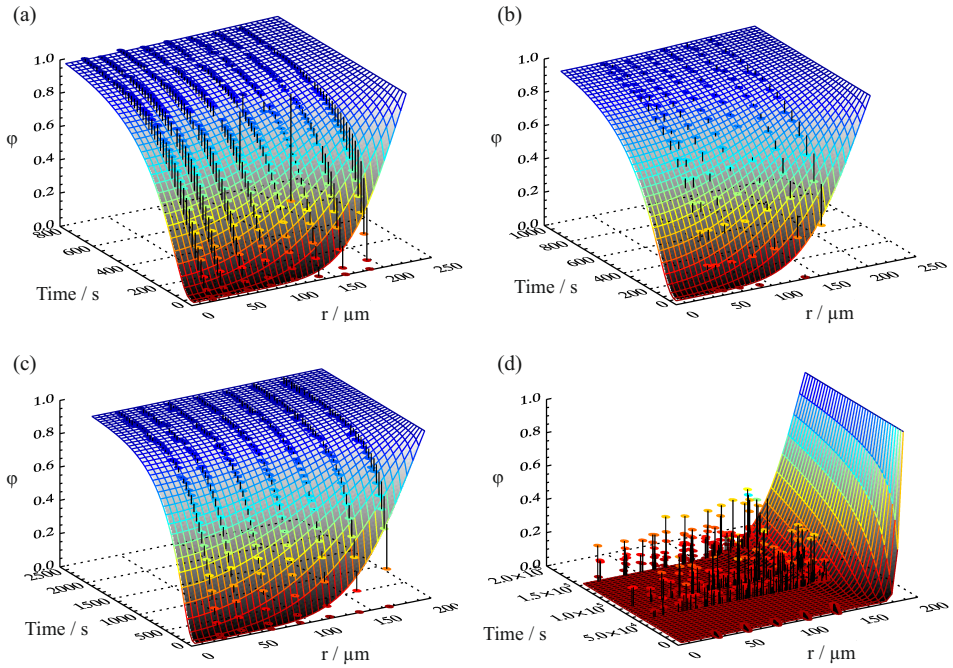

Figure 3.12: Surface fits to as a function of radial position and time, using equation 2.2, at an RH of (a) 82±2%, (b) 72±2%, (c) 62±2% and (d) 51±2% for magnesium sulfate. The quality of the fit is poor at 51% RH, which reflects the lack of homogeneity in the sample.

3.6 $MgSO_4$ gel formation

Figure 3.12 shows the diffusion surface fits for magnesium sulfate between 82 and 51% RH. There is a distinct shift from Fickian diffusion between 62 (fig. 3.12(c)) and 51% RH (fig. 3.12(d)), where it is no longer possible to find a fit to the data using equation 2.2. There is also a corresponding structural change in the sample. At 62% and higher RH, the sample appeared homogeneous when inspected with an optical microscope, whereas at 51% RH there was some structure within the disc (fig. 3.13(a)). This structure had a strong effect on D_2O diffusion. Figure 3.13(b) shows a map of ϕ for the area highlighted in fig. 3.13(a) after one day's exposure to D_2O vapour. Within the approximately triangular structure D_2O replaced the H_2O, whereas very little or no exchange occurred in the other regions.

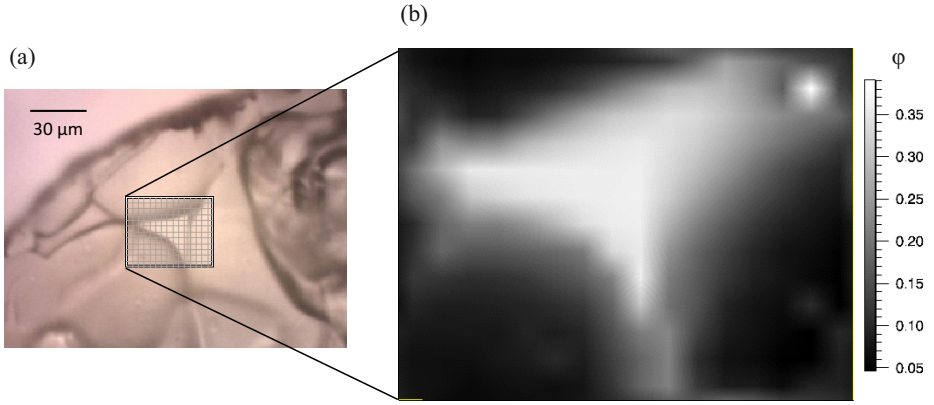

Figure 3.13: (a) Visible inhomogeneities in the magnesium sulfate disc at 51% RH. This disc was exposed to D_2O vapour for one day before a Raman map was acquired across the grid shown. (b) Fractional concentration of O-D bonds after one day. It appears that D_2O diffused faster into the central triangular shape than the surrounding regions.

Magnesium sulfate is known to form a gel due to the formation of a complex ion-induced network; this network structure has been shown to inhibit water mass

transfer within the gel (Chan *et al.*, 1998; Zhang & Chan, 2000). The transition to a gel has been variously reported to occur between 55 and 30% RH (Davies *et al.*, 2012a; Li *et al.*, 2011; Wang *et al.*, 2005; Zhao *et al.*, 2006), in agreement with the findings here. The marked change in the water diffusion process at the gel transition is completely different to the gradual decrease in the diffusion coefficient seen in the aqueous organic liquids. For this reason, it is important to note the clear distinction between semi-solids such as gels or rubbers and highly viscous liquids.

3.7 Summary

This chapter has outlined the use of a new experimental system for quantifying the diffusion coefficient of water molecules in aqueous solutions, with diffusion coefficients measured between 10^{-16} and 10^{-10} m^2s^{-1}. The methodology, which makes use of D_2O as an isotopic tracer, was shown to produce water diffusion coefficients for sucrose solutions in good agreement with those in the literature. New data for water diffusion coefficients in aqueous solutions of $MgSO_4$, levoglucosan and a mixture of raffinose, carboxylic acids and ammonium sulphate were also presented.

Using these measured water diffusion coefficients, diffusion timescales for 100 nm particles at room temperature under constant RH conditions were predicted, and it was shown that just below the glass transition it takes minutes before equilibrium with water vapour is achieved. This is a vastly shorter timescale than one would expect based on the Stokes-Einstein equation, which has been used to relate diffusion to viscosity in the past. These results reinforce previous studies showing that the Stokes-Einstein relationship is inappropriate in the regime of the glass transition (Champion *et al.*, 1997; Power *et al.*, 2013; Rampp *et al.*, 2000). It was also shown for levoglucosan and sucrose that a high bounce fraction does not necessarily mean long water diffusion timescales.

Having applied the Raman isotope tracer method to measuring water diffusion in simple proxies for atmospheric aerosol, it is now of interest to investigate a more atmospherically relevant substance: secondary organic material.

Chapter 4

Water diffusion in secondary organic material

As outlined in chapter 1, secondary organic aerosol (SOA, whose particles are composed of secondary organic material, SOM) is abundant in the atmosphere and has solid-like properties under certain conditions. Due to its potential importance in cloud formation and atmospheric chemical processes, quantitative data for water diffusion coefficients in this complex material are highly desirable. Here, the Raman isotope tracer method described in section 2.2 is used with α-pinene SOM (generated in a flow tube by collaborators at Harvard University) to provide a parameterisation for the water diffusion coefficient as a function of water activity and temperature.

4.1 Analysis of Raman data to determine O-D concentration

A sample of α-pinene SOM was prepared in the form of a disc as described in section 2.2, and equilibrated with H_2O vapour at a chosen RH and temperature. Once a uniform water activity was achieved across the disc, the H_2O vapour was replaced with D_2O vapour of the same dew point. Raman spectra were then acquired at various locations and times to monitor the diffusion of water in the sample.

In order to determine the diffusion coefficient of water, D_{water}, in SOM, it was necessary to extract the relative intensities of O-H and O-D bands from the Raman spectrum at various points on the sample. The O-H and O-D stretch bands in the SOM+H_2O and SOM+D_2O solutions were relatively small in comparison with the C-H stretch bands and the background signal. In addition, the background signal did not remain constant throughout all experiments, for example due to condensation from the laboratory on the outside of the glass window to the RH control chamber at low stage temperatures. For this reason, the spectral fitting procedure had to be carefully constrained, with certain parameters allowed to vary and others held fixed. Again, it should be emphasized that the fits produced here are for the purpose of quantifying the relative integrated band intensities of the O-H and O-D bands; they are not intended as accurate band assignments.

In order to constrain the C-H peak fitting, a spectrum was taken of the background (i.e. the hydrophobic glass side without sample). A Gaussian curve plus a constant was fitted to this, as shown in fig. 4.1. The width and wavenumber of this Gaussian were held fixed in all subsequent fits, with the intensity allowed to vary. The constant was determined by the minimum intensity recorded in each spectrum: it had to be between 80% and 100% of this minimum value. To fit a set of peaks to the C-H stretch region alone, the O-H and O-D bands needed to be removed from the spectrum. To do this, a droplet of SOM solution was exposed to H_2O vapour at 70% RH until it reached equilibrium with the surrounding vapour phase. Since the droplet was no longer changing with time, a long exposure, multiple acquisition Raman measurement could be made to obtain a high-quality spectrum with high signal-to-noise ratio. The droplet was then exposed to D_2O vapour until complete exchange had taken place and no O-H peaks remained. Again, a high-quality spectrum was taken. A background fit (using the constrained Gaussian plus constant described above) was performed using the upper and lower ends of each spectrum, then subtracted. The spectra were then normalised to the peak intensity; the results of this are shown in fig. 4.2. To obtain a spectrum without either O-H or O-D bands, the lower half of the SOM+H_2O spectrum was stitched to the upper half of the SOM+D_2O spectrum. 7 Gaussian curves were fitted to the remaining C-H stretch, along with a shallow,

broad Gaussian that was required to account for a slightly raised background, as shown in fig. 4.3. The relative peak positions and intensities of the 7 C-H Gaussians were fixed in all subsequent fits. The peak position of the broad, shallow Gaussian was fixed relative to the 7 C-H Gaussians, but its intensity and width was allowed to vary.

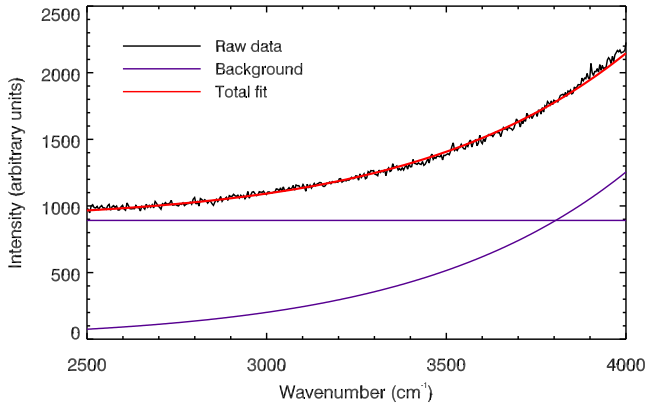

Figure 4.1: The Raman spectrum of a hydrophobic glass slide. The purple lines show a Gaussian curve and a constant which add to give the red fit to the background.

Figure 4.4 shows the total fit (red) to three spectra of varying H_2O/D_2O concentrations, using the constraints described. When fitting to a spectrum taken during a H_2O/D_2O exchange experiment, three variable-intensity Gaussians representing the O-D stretch band were constrained to lie within the wavenumber range 3200 to 3500 cm^{-1}, and had FWHMs between 45 and 235 cm^{-1} (green). Another three variable-intensity Gaussians representing the O-H stretch band were constrained to lie within the wavenumber range 2300 to 2600 cm^{-1}, and also had FWHMs between 45 and 235 cm^{-1} (blue).

For each spectrum obtained, the fitting procedure was performed three times: first with all Gaussian peaks described above available to the fitting routing, secondly without the three O-H Gaussians available, and thirdly without the three O-D Gaussians available. This allowed an f-test to be performed using the χ^2 values for the different fits, so that the level of significance of the O-H and

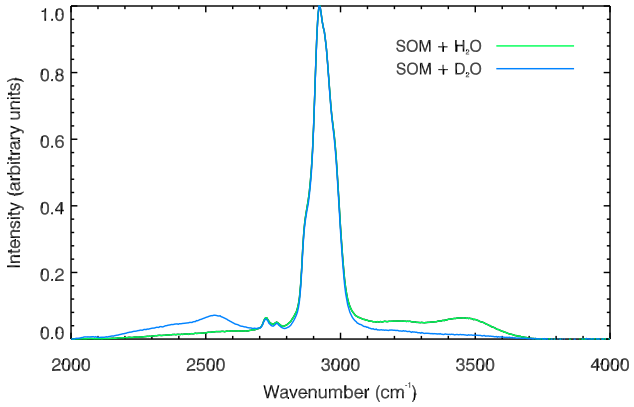

Figure 4.2: Background corrected, normalised spectra of aqueous α-pinene SOM after long periods of exposure to H_2O (green) and D_2O vapour (blue) at 70% RH.

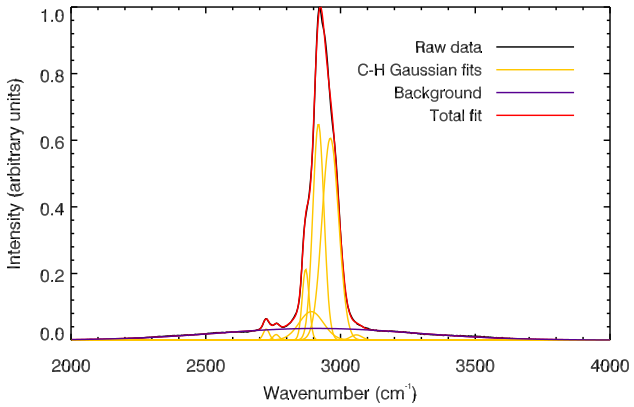

Figure 4.3: The Raman spectrum of aqueous α-pinene SOM with O-H and O-D peaks removed. Gaussian fits to the C-H stretch band (yellow) and the background (purple) shown here are used to constrain the fitting routine. The total fit (red) overlays the raw data (black) to the point that it is barely visible.

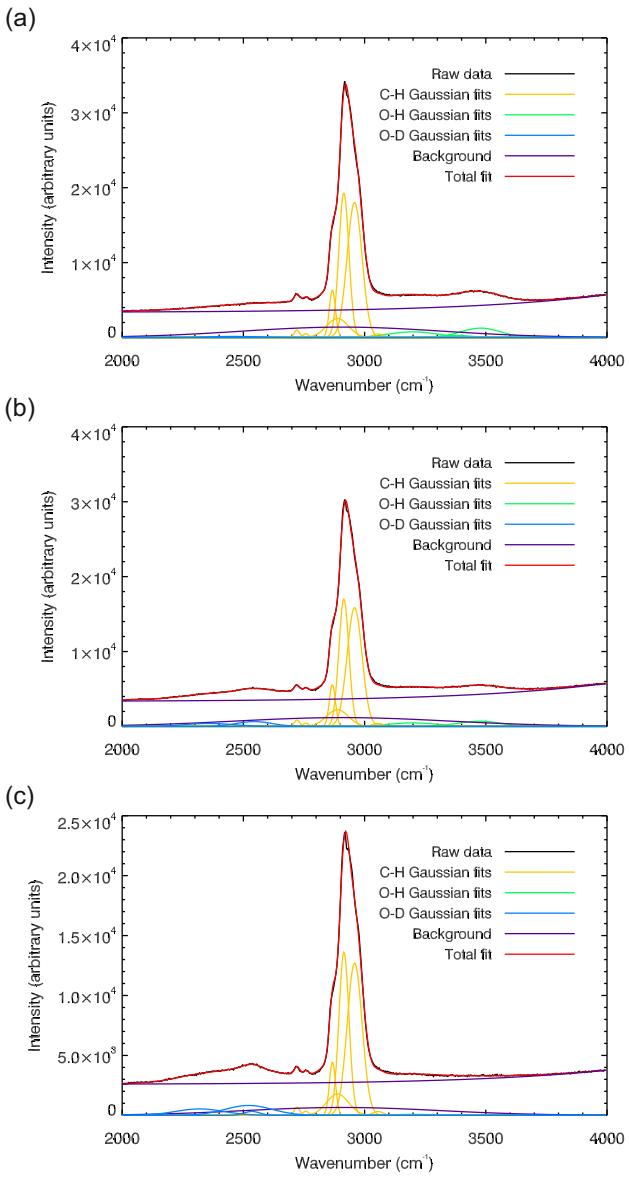

Figure 4.4: Results of the full fitting procedure for aqueous SOM containing (a) mostly H_2O, (b) similar amounts of H_2O and D_2O, and (c) mostly D_2O.

O-D bands could be determined. Spectra where the probability that the decrease in χ^2 associated with the addition of either the O-H or O-D bands was due to chance alone was greater than 0.01 were excluded from subsequent analysis in the diffusion coefficient surface fit.

4.1.1 Obtaining the water diffusion coefficient

The results of the spectral fitting procedures were used with equation 3.1 to find the diffusion coefficient of D_2O, as described in chapter 3: to determine D_{water} at a given RH, a surface fit of equation 2.2 with the diffusion coefficient as a variable parameter was performed to the measured values of $\phi(r,t)$, again using the Levenberg-Marquardt technique. Due to the difficult nature of the fitting procedure in SOM (caused by shallow peaks and large background signals), the fit could sometimes be improved by allowing ϕ_0 and ϕ_1 to vary, along with D_{water}. The effect of allowing ϕ_0 and ϕ_1 to vary did not appear to systematically alter the values of D_{water} that were determined, and in most cases the fitting routine found the best fit values of ϕ_0 and ϕ_1 to be 1 and 0, respectively. It did, however, improve the quality of the surface fit in the few cases where the background signal was particularly large.

Figure 4.5(a) shows an example of the surface fit to a set of data for SOM, where each measured data point is connected to the fitted surface by a black line for comparison, and fig. 4.5(b) shows the corresponding one-to-one plot.

4.2 Measured diffusion coefficients in secondary organic material

Measurements of water diffusion in α-pinene secondary organic material (SOM) were made between 240 and 280 K, over a water activity range of 0.15 to 0.8, as shown in fig. 4.6. Experiments were repeated over a period of time to verify that the diffusion coefficients were unaffected by sample age. Measurements at lower temperatures were not possible due to the required duration of the experiments (data for the slowest diffusion coefficients presented here took several weeks to

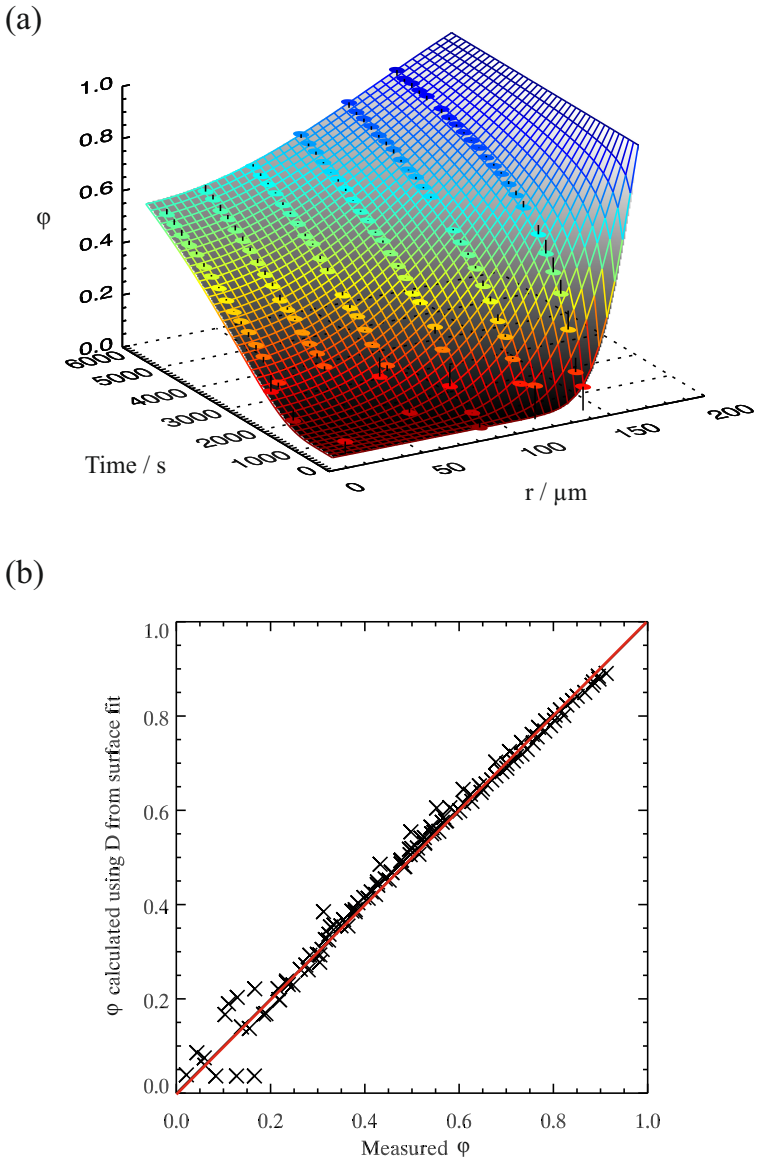

Figure 4.5: (a) Plot of the fractional concentration of O-D bonds, ϕ, as a function of radial distance and time after switch from H_2O to D_2O vapour in an SOM disc at 70% RH. The grid shows the surface fit to the data, the collected data points are joined to the grid by black lines. The colour corresponds to the value of ϕ. (b) One-to-one plot showing the measured ϕ *vs.* ϕ according to the fit, also at 70% RH.

obtain) and measurements at higher temperatures were affected by an increase in sample fluorescence over the course of the experiment so are not reported.

4.3 Parameterisation of the diffusion coefficient of water in SOM

The measured diffusion coefficients are plotted *vs* water activity and temperature in fig. 4.6(a), with each data point representing a diffusion measurement on one disc. An empirical fit to the data was produced using a Vignes-type equation (Vignes, 1966). This form of equation has been found to fit the composition-dependent diffusion coefficients of methanol/ethanol mixtures (Matthiesen *et al.*, 2011), as well as providing a fit in good agreement with water diffusion coefficients in aqueous levoglucosan solutions across a range of temperature and humidity conditions (Lienhard *et al.*, 2014). The diffusion coefficient of water is given by:

$$D_{water} = (D^0_{water})^{x_w \alpha} (D_0^{SOM})^{1 - x_w \alpha} \tag{4.1}$$

where D^0_{water} is the temperature-dependent self-diffusion coefficient of water (Smith & Kay, 1999) and D^0_{SOM} is the diffusion coefficient of water in amorphous SOM at a water activity, a_w, of 0. D^0_{SOM} is constrained to fit the form of a Vogel-Fulcher-Tammann (VFT) relationship (Angell, 1995):

$$\log_{10}(D^0_{SOM}) = -\left(A + \frac{B}{T - T_0}\right) \tag{4.2}$$

in which A, B and T_0 are fitted parameters indicating the high temperature limit of the diffusion coefficient, the fragility and the temperature at which the diffusion coefficient would diverge, respectively. x_w is the mole fraction of water, calculated from the water activity using the effective hygroscopicity parameter (κ_{org}) (Koop *et al.*, 2011; Petters & Kreidenweis, 2007):

$$x_w = \left(\frac{M_w}{M_{org}} \frac{\rho_{org}}{\rho_w} \frac{(1 - a_w)}{\kappa_{org} a_w} + 1\right)^{-1} \tag{4.3}$$

where M_w is the molar mass of water, ρ_w is the density of water, M_{org} is the effective molar mass of SOM, ρ_{org} is the density of SOM. A value of 180 g·mol^{-1}

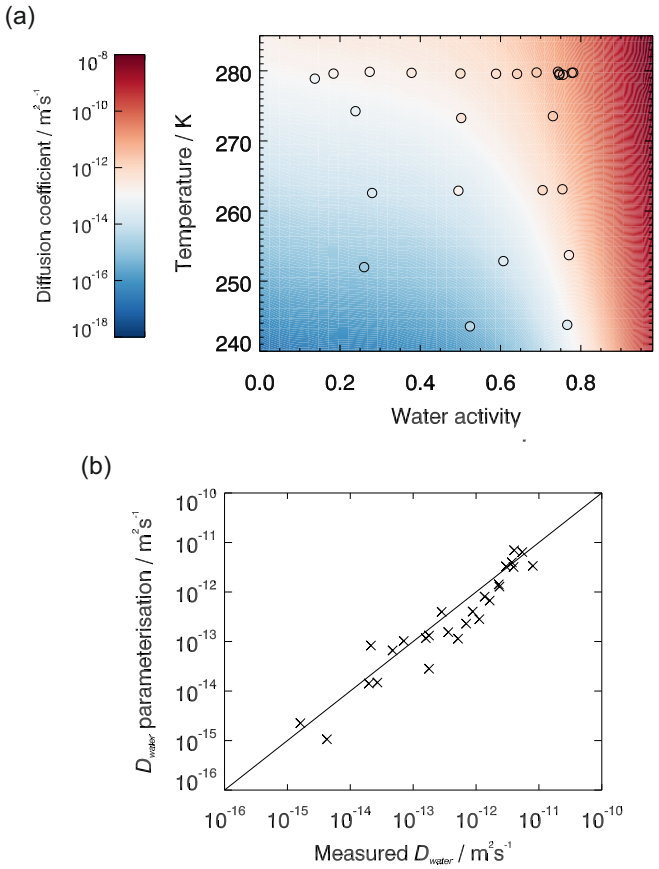

Figure 4.6: (a) Diffusion coefficients of water in SOM. Experimental data points are shown as coloured circles and the fit is the shaded background. The differences in colour between the background and circle interiors show the difference between the fit and the measured data points. (b) A one-to-one plot showing the measured water diffusion coefficients vs the parameterisation.

is used for the effective molar mass of SOM (Engelhart *et al.*, 2008; King *et al.*, 2007), and an effective density of SOM of 1.2 g·cm^{-3} (Zhang *et al.*, 2015). For κ_{org}, a value of 0.1 is used, calculated using O:C ratio measured by Yue Zhang for SOM from the flow tube of 0.38±0.01 (Aiken *et al.*, 2007, 2008; Zhang *et al.*, 2015), according to the linear relationship given by Lambe *et al.* (2011). This κ_{org} value is consistent with previous measurements (Duplissy *et al.*, 2011; Jurányi *et al.*, 2009; Petters & Kreidenweis, 2007; Prenni *et al.*, 2007; Tritscher *et al.*, 2011). α is an activity coefficient (Lienhard *et al.*, 2014; McGlashan, 1963):

$$\ln \alpha = (1 - x_w)^2[C + 3D - 4D(1 - x_w)] \tag{4.4}$$

C and D are linear in temperature below a certain temperature, T_{cutoff}, and constant at higher temperatures, such that $C = p + qT_\alpha$ and $D = r + sT_\alpha$, where

$$T_\alpha = \begin{cases} T & T < T_{cutoff} \\ T_{cutoff} & \geq T_{cutoff} \end{cases} \tag{4.5}$$

with p, q, r, s and T_{cutoff} as fitted parameters. The fit was performed using the Levenberg-Marquardt technique (Markwardt, 2009); the best fit parameters, together with their estimated errors, are shown in table 4.1. The fit is shown as the shaded surface in fig. 4.6(a), and compared to the measured data points in a one-to-one plot in fig. 4.6(b).

Table 4.1: Parameters for the Vignes-type fit described in equations 4.1, 4.2, 4.3, 4.4 and 4.5.

	p	q	r	s	T_{cutoff}	A	B	T_0
Best fit value	-13	0.043	-10.5	0.035	230	7.4	650	165
Estimated error	1	0.006	0.7	0.003	3	0.3	60	4

4.3.1 Determining errors in the water diffusion coefficient parameterisation

The errors in the individual diffusion coefficient measurements are calculated in the same way as in chapter 3. The upper error is calculated using the upper

limit on the disc's radius, the upper limit on the time taken for the switch from H_2O to D_2O vapour, and the random error in the surface fit due to errors in ϕ. Likewise, the lower error is calculated using the lower limit on the disc's radius, the lower limit on the time taken for the switch from H_2O to D_2O vapour, and the random error in the surface fit due to errors in ϕ. The error in the fitted $D_{water}(a_w, T)$ comes from not only the error in the diffusion coefficients, but also the error in RH and temperature. Due to the complicated nature of these errors, the uncertainty in the fitted diffusion coefficient was estimated by performing the Vignes-type equation fit 100,000 times. Each time, the RH and temperature to be used in the fit for each of the 26 datapoints was drawn from a probability distribution function. For the temperature errors, a normal distrubition was used, with a standard deviation corresponding to the standard deviation in the continuous temperature measurement (as measured using a calibrated PT100 temperature sensor embedded in the cooled metal block on which the sample was placed). The RH errors had to take into account errors due to potential radial inhomogeneities, errors due to the difference in vapour pressures between H_2O and D_2O, and the standard deviation in the continuous RH measurement by the dewpoint hygrometer. To do this, a skew normal distribution was assigned to each measurement, with the mode corresponding to the best estimate of RH and the 5% and 95% limits corresponding to the estimated lower and upper bounds. The reported errors in the fitted parameters are the χ^2-weighted standard deviations in the output from these 100,000 fits.

4.4 Comparison with literature data

Figure 4.7 compares the measured water diffusion coefficients at 280 K with predictions of water diffusion coefficients in α-pinene SOM based on the semi-empirical VFT-based approach by Berkemeier *et al.* (2014), also at 280 K. The predictions from this approach are lower than the experimental data presented here; this could be due to differences between the composition of the flow tube SOM sample and the model SOM composition used by Berkemeier *et al.* (2014) in the semi-empirical VFT approach. The data collected in this study are also compared with diffusion coefficients estimated from room temperature viscosity

measurements made on α-pinene SOM generated in a chamber (Renbaum-Wolff *et al.*, 2013) and in the flow tube[1]. The Stokes-Einstein equation is used here to convert viscosities to diffusion coefficients, and leads to values which are up to 8 orders of magnitude smaller than the measured values. This is unsurprising as the hydrodynamic Stokes-Einstein relation is known to break down at high viscosity, and the diffusion coefficients of water and larger solute molecules generally deviate near the glass transition (Champion *et al.*, 1997; Power *et al.*, 2013; Rampp *et al.*, 2000; Zhu *et al.*, 2011). Indeed, for water transport in viscous aqueous sucrose, the estimates from Stokes-Einstein are more than an order of magnitude off at viscosities higher than 100 Pa·s. This breakdown of the Stokes-Einstein description emphasizes the need to make direct measurements of diffusion: whilst the relation may be applicable at low viscosities or for large molecules, it fails to predict water diffusion coefficients in highly concentrated SOM. Finally, the water diffusion coefficient measurements presented here are compared with estimates produced from a model based on percolation theory (Shiraiwa *et al.*, 2013), which assumed that the water diffusion coefficient in pure SOM is the same as that in pure amorphous sucrose. Data from this study show that water diffusion in α-pinene SOM is faster than in sucrose solutions at the same water activity and temperature, possibly explaining some of the discrepancies between measured data and percolation theory estimate.

To further compare the laboratory data with the semi-empirical VFT-based approach of Berkemeier *et al.* (2014), fig. 4.8 compares both the water activity and temperature variation of the water diffusion coefficient parameterisation given in section 4.3 with the semi-empirical predictions at 280 and 240 K. The shapes

[1]SOM was produced by Yue Zhang at Harvard in a flow tube as described in section 2.2.3. James Grayson at the University of British Columbia used the approach of using a poke-flow technique and subsequent simulations of fluid flow to determine limits of viscosity is described by Renbaum-Wolff *et al.* (2013), with the sole difference here being that simulations of material flow were used to determine the lower limit of viscosity (as opposed to lower limits derived through the use of lower limits of viscosity being inferred from use of the bead-mobility technique at high RH, as was done previously). For simulations of the lower limit of viscosity, a slip length of 5 nm and a surface tension of 32 $mN \cdot m^{-1}$ were used. Contact angles were 63° at 40% RH and 70° at 30% RH, whilst for simulations of the upper limit of viscosity at 40% RH, a slip length of 10 µm, a surface tension of 75 $mN \cdot m^{-1}$, and a contact angle of 60° were used.

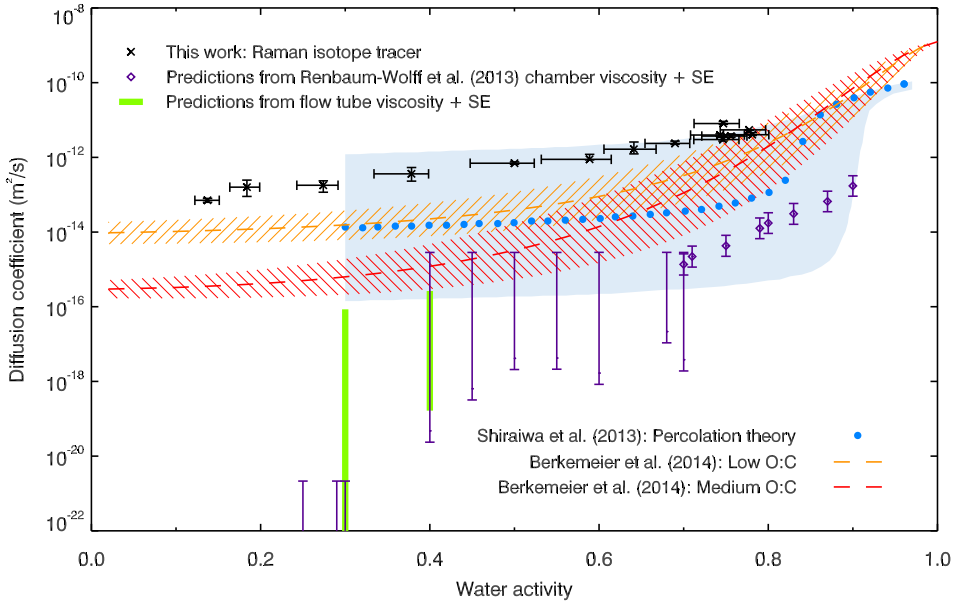

Figure 4.7: Comparison of measured diffusion coefficients of water in α-pinene SOM with literature data. Laboratory measurements at 280 K (black crosses) are compared with predictions from percolation theory at room temperature (blue circles, with blue shaded uncertainty region (Shiraiwa *et al.*, 2013)) and the semi-empirical method used by Berkemeier *et al.* (2014) for low (orange dashed line and hatched error region, O:C = 0.3) and medium (red dashed line and hatched error region, O:C = 0.5) oxidation states at 280 K. Also shown are the diffusion coefficients predicted by the Stokes-Einstein (SE) equation using the room temperature viscosity measurements on chamber-generated α-pinene SOM by Renbaum-Wolff *et al.* (2013) (generated using 80-100 ppb α-pinene and 300 ppb ozone, purple diamonds and bars), and on flow tube-generated α-pinene SOM (generated using 5 ppm α-pinene and 12 ppm ozone, green bars). Experiments using the "poke-flow" technique generate only upper and lower limits on viscosity; these are shown as purple and green bars with no datapoints.

of the water activity dependence curves are similar, despite being described by equations of different forms. The temperature dependence is stronger in the Berkemeier *et al.* (2014) prediction which predicts smaller diffusion coefficients than are measured here, although the results are in agreement within error above a water activity of 0.4.

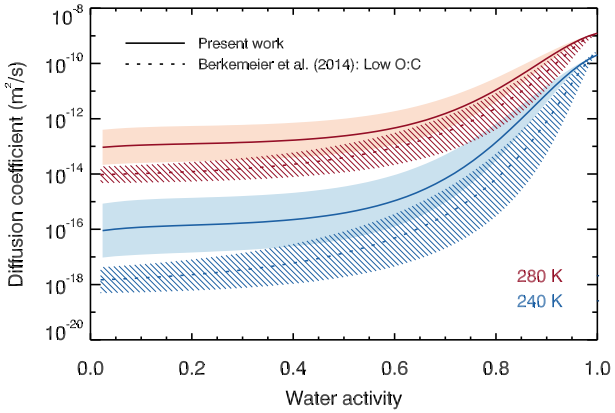

Figure 4.8: The fit to the experimental data (solid lines and shaded error regions) compared with the semi-empirical low oxidation predictions from Berkemeier *et al.* (2014) (dotted lines and hatched error regions) at 280 K and 240 K.

4.5 Relationship between water diffusion and particle rebound

There are now three materials for which water diffusion and rebound data have been investigated over a range of RHs at room temperature: aqueous sucrose, levoglucosan and α-pinene SOM. These data are reproduced in fig. 4.9(a) for the purposes of comparison (it should be borne in mind that sucrose and α-pinene SOM were studied using one set of apparatus (Bateman *et al.*, 2014b) whilst levoglucosan was studied using another (Saukko *et al.*, 2012b)). Aqueous sucrose appears to have the sharpest transition in rebound fraction, at around

75% RH, whilst levoglucosan and α-pinene SOM have more gradual decreases in rebound fraction upon increasing RH. Above 40% RH, the diffusion coefficient of water in aqueous levoglucosan is higher than in the other two materials. The lower rebound fraction of levoglucosan therefore hints that there may be some correlation between diffusion and rebound.

To assess this, the RHs at which rebound measurements have been made were converted to water diffusion coefficients using the parameterisations given by equations 3.2 and equations 4.1, 4.2, 4.3, 4.4 and 4.5. This facilitates the comparison of rebound fraction with water diffusion coefficient, as shown in fig. 4.9(b). The correlation between water diffusion and rebound fraction is particularly apparent between 10^{-12} and 10^{-13} m^2s^{-1}. However, given that there is little change in rebound fraction below a water diffusion coefficient of 10^{-12} m^2s^{-1}, where the water diffusion timescale for a 100 nm diameter droplet is much shorter than a millisecond, it seems unlikely that rebound fraction measurements could be used to distinguish between particles which would equilibrate over longer timescales.

4.6 Summary

Diffusion coefficients of water in α-pinene SOM were measured across a wide range of temperatures and RHs. At warm temperatures, these measured diffusion coefficients were found to be slightly higher than those predicted by percolation theory (Shiraiwa *et al.*, 2013) and the semi-empirical method developed by Berkemeier *et al.* (2014), and several orders of magnitude higher than would be predicted from viscosity measurements using the Stoke-Einstein equation. The experimental data were used to produce a parameterisation of the diffusion coefficient of water in α-pinene SOM as a function of water activity and temperature. Above a water activity of 0.4, this parameterisation was found to be in agreement with that of Berkemeier *et al.* (2014) within error at both 240 K and 280 K.

Having measured water diffusion coefficients in a third material for which impactor rebound fraction data are available, a correlation between the two quantities was investigated. Across the three materials, there was better correlation between water diffusion coefficient and rebound fraction than between RH and rebound fraction (see fig. 4.9). This could be because water diffusion is linked

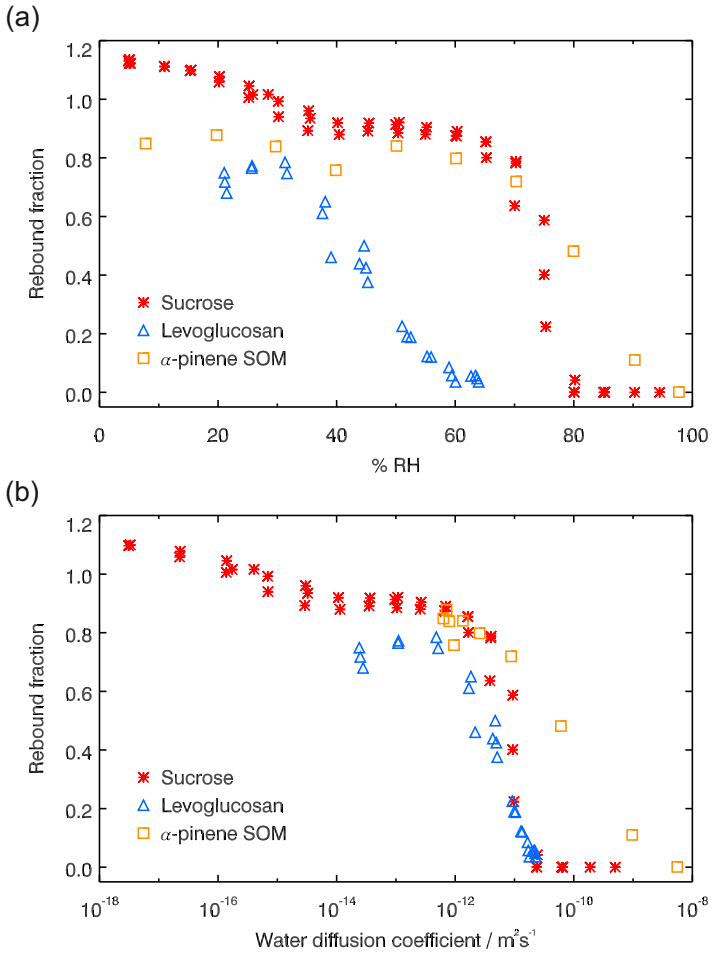

Figure 4.9: (a) Literature data for the rebound fraction of sucrose (Bateman *et al.*, 2014b), levoglucosan (Saukko *et al.*, 2012b) and α-pinene SOM (Bateman *et al.*, 2014b) in impaction apparatus, as a function of RH. (b) The same literature data, but reported in terms of water diffusion coefficient using the parameterisations given in this chapter and the previous one to convert from RH.

(albeit not by the Stokes-Einstein equation) to viscosity, which is a determining factor for particle rebound.

Because of the dependence of the water diffusion coefficient on water activity, water uptake by aerosol particles is a self-accelerating process. To relate the diffusion measurements presented in this chapter to water uptake by atmospheric aerosol, therefore, it is necessary to use a diffusion model. This will be discussed in the following chapter.

Chapter 5

Modelling water diffusion and uptake in aerosol particles

To investigate water uptake and loss from aerosol particles in response to changing RH and temperature conditions, rather than the macroscale cylindrical disc used in the laboratory diffusion measurements, a multi-shell water diffusion model was developed similar to those used by Zobrist *et al.* (2011) and Lienhard *et al.* (2014). As described below, the model tracks water diffusion into and out of a spherical aqueous droplet in response to changing relative humidity conditions. The droplet is split into a number of concentric shells, whose concentration and diffusion coefficient are allowed to vary as time progresses. Shells are numbered from $i = 0$ (the central shell) to $i = \gamma - 1$ (the outer shell), with the convention that a flux of water molecules radially outwards is positive. The model works by allowing water molecules to diffuse between shells: a flux is calculated across each of the two boundaries to each shell ($f_{(i-\frac{1}{2})}$ and $f_{(i+\frac{1}{2})}$), according to Fick's first law (see fig. 5.1). This flux determines the number of water molecules, ΔN_w, that move between shells during each timestep, Δt. The model is used for both aqueous sucrose (for the purpose of model comparison with laboratory data) and α-pinene SOM.

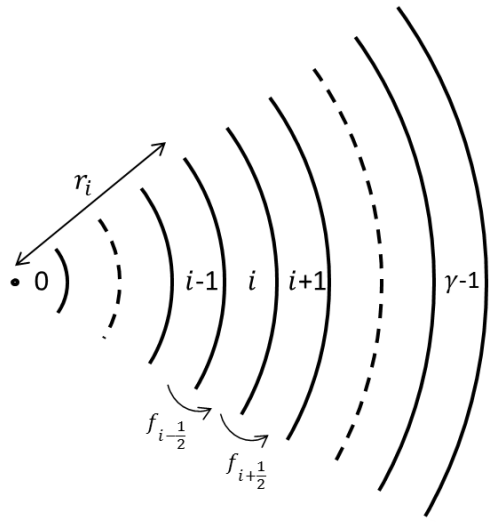

Figure 5.1: Schematic representation of shells in the model. There are γ shells, with each shell i having an internal radius of r_i.

5.1 Description of model

The inputs required each time the model is run are:

- Number of shells, γ.
- The initial water activity, a_w, across the droplet.
- The initial radius, $R_{t=0}$, of the droplet if all of the shells are at the same concentration. The model works by assuming the outer shell always has a water activity corresponding to the surrounding relative humidity, so at $t = 0$ the outer shell will actually be slightly thicker or thinner than the others if $RH/100$ is different to the starting water activity.
- The frequency with which to record a datapoint.
- The duration of the simulation.
- The relative humidity profile, p_{RH} *vs* p_t, that the simulation will follow.

- The maximum and minimum percentage change allowed in the number of water molecules in the shell which sees the biggest change in the number of water molecules in a given timestep.
- Density of solute, ρ_s, and water, ρ_w.
- Molar mass of solute, M_s, and water, M_w.

A set of arrays is created to contain information about the physical state of each shell in each timestep (water activity, shell thickness, number of water molecules, inner radius, solute mass fraction, number of solute molecules, volume, the percentage change in the number of water molecules during the timestep, the water molecule number concentration, the water diffusion coefficient, the average water diffusion coefficient between shell i and $i+1$, the average water diffusion coefficient between shell i and $i-1$, the flux from shell $i-1$ to shell i, the flux from shell i to $i+1$ and the change in the number of water molecules). So that the model runs quickly, these arrays are one dimensional, and are overwritten each timestep. "Readings" are taken at certain time intervals (i.e. the relevant data in an array are saved to a larger, two dimensional print array for use later), as defined by the user in the inputs. The initial shell thickness of all shells except for the outer shell is calculated:

$$d_{s,t=0} = \frac{R_{t=0}}{\gamma} \tag{5.1}$$

The solute mass fraction, w, in each shell is calculated from its water activity. For sucrose, this is done using the relationship given in equation 10 of Zobrist *et al.* (2011), assuming the second half of the equation is negligible at room temperature.

$$w = \frac{0.99721a_w - 1 + \sqrt{(1-0.99721a_w)^2 - 4a_w(0.13599a_w - 0.13599)}}{2(0.13599a_w)} \tag{5.2}$$

For other solutes, the effective hygroscopicity parameter may be used to relate water activity to mole fraction (Koop *et al.*, 2011). The number of water molecules, N_w, is found using the volume, V, of each shell. Assuming volume additivity of pure component densities,

$$V = \frac{V_w N_w + V_s N_s}{N_A} \tag{5.3}$$

where N_A is Avogadro's number, N_s is the number of solute molecules, and the molar volume of water and the solute are calculated as follows:

$$V_w = \frac{M_w}{\rho_w} \tag{5.4}$$

$$V_s = \frac{M_s}{\rho_s} \tag{5.5}$$

The volume of shell i, which has an internal radius r_i, is

$$V_i = \frac{4}{3}\pi r_{i+1}^3 - \frac{4}{3}\pi r_i^3 \tag{5.6}$$

At the start, all shells have the same thickness

$$r_{t=0,i} = i d_{s,t=0} \tag{5.7}$$

$$r_{t=0,i+1} = (i+1) d_{s,t=0} \tag{5.8}$$

Using equations 5.6, 5.7 and 5.8,

$$V_{i,t=0} = \frac{4}{3}\pi d_{s,t=0}^3 [(1+i)^3 - i^3] \tag{5.9}$$

By definition, the solute mass fraction is

$$w = \frac{N_s M_s}{N_s M_s + N_w M_w} \tag{5.10}$$

$$\therefore N_s = \frac{N_w M_w w}{M_s(1-w)} \tag{5.11}$$

Equating equations 5.3 and 5.6, and substituting equation 5.11, the initial number of water molecules in shell i is

$$N_{w,t=0} = \frac{\frac{4\pi N_A}{3} d_{s,t=0}^3 [(i+1)^3 - i^3]}{V_w + V_s \frac{M_w w_{t=0}}{M_s(1-w_{t=o})}} \tag{5.12}$$

The number of solute molecules in each shell is calculated from the solute mass fraction at the start. This stays fixed throughout the simulation.

$$N_s = \frac{N_{w,t=0} M_w w_{t=0}}{M_s(1-w_{t=0})} \tag{5.13}$$

In order for the outer edge to maintain equilibrium with the surrounding relative humidity, some water molecules are added/removed from the outer shell.

$$a_{w,\gamma-1} = \frac{p_{RH,t=0}}{100} \tag{5.14}$$

The new solute mass fraction of the outer shell is calculated using equation 5.2. The solute mass fraction is used, along with the number of solute molecules (which is fixed), to calculate the new number of water molecules in the outer shell (equation 5.10). The initial volume of each shell (now that the outer shell has been adjusted) is calculated using molar volumes:

$$V_{t=0} = \frac{V_w N_{w,t=0} + V_s N_s}{N_A} \tag{5.15}$$

From this the actual total radius of the droplet at the start can be calculated:

$$R = \sqrt[3]{\frac{3}{4\pi} \sum_{i=0}^{\gamma-1} V} \tag{5.16}$$

This should be very close to the user defined initial radius, differing slightly because of the outer shell gaining/losing water molecules to equilibrate with the surrounding RH. Similarly, the inner radius of shell i is

$$r_i = \sqrt[3]{\frac{3}{4\pi} \sum_{i=0}^{i-1} V} \tag{5.17}$$

which is the same as calculated in equation 5.7 at $t = 0$ (the inner radius of shell $i = 0$ is obviously 0). The thickness of the outer shell is

$$d_{s,\gamma-1} = R - r_{\gamma-1} \tag{5.18}$$

The water number concentration in each shell is

$$n_w = \frac{N_w}{V} \tag{5.19}$$

The diffusion coefficient of water in each shell, D_{H_2O}, is calculated based on its water activity, for sucrose using the parameterisation given in chapter 3, and for α-pinene SOM using the parameterisation given in chapter 4. To calculate the

flux of water molecules between shell $i-1$ and i, it is necessary to work out the average water diffusion coefficient of the two shells. For the inner shell, this is arbitrarily left as simply the diffusion coefficient of the inner shell (there is no flux from shell $i-1$ in this case, so this value is not used in any calculations).

$$D_{H_2O,i-\frac{1}{2}} = \frac{D_{H_2O,i} + D_{H_2O,i-1}}{2} \tag{5.20}$$

Similarly,

$$D_{H_2O,i+\frac{1}{2}} = \frac{D_{H_2O,i} + D_{H_2O,i+1}}{2} \tag{5.21}$$

For the outer shell, this diffusion coefficient is set to be equal to the diffusion coefficient in the outer shell, although it is not used in any calculations because the outer shell instantaneously equilibrates with the surrounding RH. Fick's first law states that the flux per unit area per unit time, J, is proportional to the concentration gradient, $\frac{\partial\phi}{\partial x}$:

$$J = -D\frac{\partial\phi}{\partial x} \tag{5.22}$$

where D is the diffusion coefficient of the diffusing species. The flux of water molecules per unit time across the boundary between shell $i-1$ and i is therefore approximated by

$$f_{i-\frac{1}{2}} = -4\pi r_i^2 D_{H_2O,i-\frac{1}{2}} \frac{\Delta\phi}{\Delta x} \tag{5.23}$$

which becomes

$$f_{i-\frac{1}{2}} = -4\pi r_i^2 D_{H_2O,i-\frac{1}{2}} \frac{(n_{w,i} - n_{w,i-1})}{0.5(d_{s,i} + d_{s,i+1})} \tag{5.24}$$

For the central shell, this is evidently 0. Similarly, the flux of water molecules per unit time across the boundary between shell i and $i+1$ is

$$f_{i+\frac{1}{2}} = -4\pi r_{i+1}^2 D_{H_2O,i+\frac{1}{2}} \frac{(n_{w,i+1} - n_{w,i})}{0.5(d_{s,i} + d_{s,i+1})} \tag{5.25}$$

This is not calculated for the outer shell because it instantaneously equilibrates with the surrounding RH. The change in the number of water molecules in each shell can now be calculated:

$$\Delta N_w = (f_{i-\frac{1}{2}} - f_{i+\frac{1}{2}})\Delta t \tag{5.26}$$

The maximum ΔN_w (out of all the shells except the outer shell) is limited by altering Δt, so that the largest percentage change in any one shell lies within a

range chosen by the user. Once ΔN_w has been added to N_w for each shell in the first timestep, the model loops over successive timesteps, finishing either when the simulation has reached the desired point or the maximum number of timesteps allowed has been reached. The time at the start of the timestep is calculated by simply adding the duration of the previous timestep, Δt, to the time, t. The RH to be used in each timestep is calculated by linearly interpolating between the two nearest points in the user-defined environmental profile. The water activity of the outer shell is set to this $RH/100$. The new solute mass fraction of the outer shell is calculated using the water activity corresponding to the surrounding RH, with equation 5.2. The new number of water molecules in this shell is then calculated using a rearrangement of equation 5.10. The new number of water molecules in each shell (except the outer shell) is again calculated by adding ΔN_w from the previous timestep to N_w (the number of water molecules in each shell at the start of the previous timestep). This new number of water molecules is used to calculate the solute mass fraction, using equation 5.10. The new water activity of each shell is calculated using equation 10 of Zobrist *et al.* (2011) for sucrose, or by using the effective hygroscopicity value for α-pinene SOM (Koop *et al.*, 2011). The volume of each shell is found using equation 5.3, and the new total radius is found using equation 5.16. The inner radius of each shell is again found using equation 5.17. The thickness of each shell except the outer shell is

$$d_{s,i} = r_{i+1} - r_i \tag{5.27}$$

The outer shell thickness is given by equation 5.18. The new water number concentration is calculated using equation 5.19, the water diffusion coefficient in each shell is found using either the sucrose parameterisation given in chapter 3 or the α-pinene SOM parameterisation given in chapter 4. Equations 5.20 and 5.21 are used to find the average diffusion coefficients between adjoining shells, and the fluxes per unit time between shells are calculated with equations 5.24 and 5.25. ΔN_w is again limited by changing Δt, so that the largest percentage change in any one shell lies within the range chosen by the user. If the correct amount of seconds has passed in the simulation for a reading to be taken, the relevant set of parameters is saved to the output array.

5.2 Convergence checks

For each scenario used in the model, convergence checks were performed to ensure that the number of shells and the minimum and maximum percentage changes did not affect the result. The aim was to make the model as highly resolved as possible (i.e. to maximise the number of shells and minimise the percentage change in each timestep) without increasing the computational demands beyond feasible timescales.

5.3 Verification of the model

To verify the accuracy of the model, its output was compared with laboratory measurements of changes in aqueous sucrose particle radii driven by RH changes, measured in both electrodynamic balance (EDB) and optical tweezers experiments by James Davies and Andrew Rickards at the University of Bristol (these methods have been described in detail by Davies *et al.* (2012b); Dennis-Smither *et al.* (2012); Hanford *et al.* (2008); Hargreaves *et al.* (2010); Rickards *et al.* (2013)). Using the same RH profiles as the laboratory experiments, the model simulated these changes in radii using water diffusion coefficients measured in aqueous sucrose with the Raman tracer technique (chapter 3). Figure 5.2 demonstrates that the model is able to reproduce the laboratory data within the accuracy of the experiments. It is possible to use diffusion coefficients measured in a 200 µm disc to simulate laboratory measurements on droplets of 13 µm and 4 µm radius, smaller in volume by a factor of $< 10^{-4}$, thus confirming the validity of the experimental and modelling approach.

5.4 Timescales for hygroscopic growth and shrinkage in SOM

In order to explore the response of SOM aerosol particles to changes in RH at 280 K, simulations of the time-resolved size and composition were performed for a 100 nm diameter water-soluble α-pinene SOM particle experiencing step changes

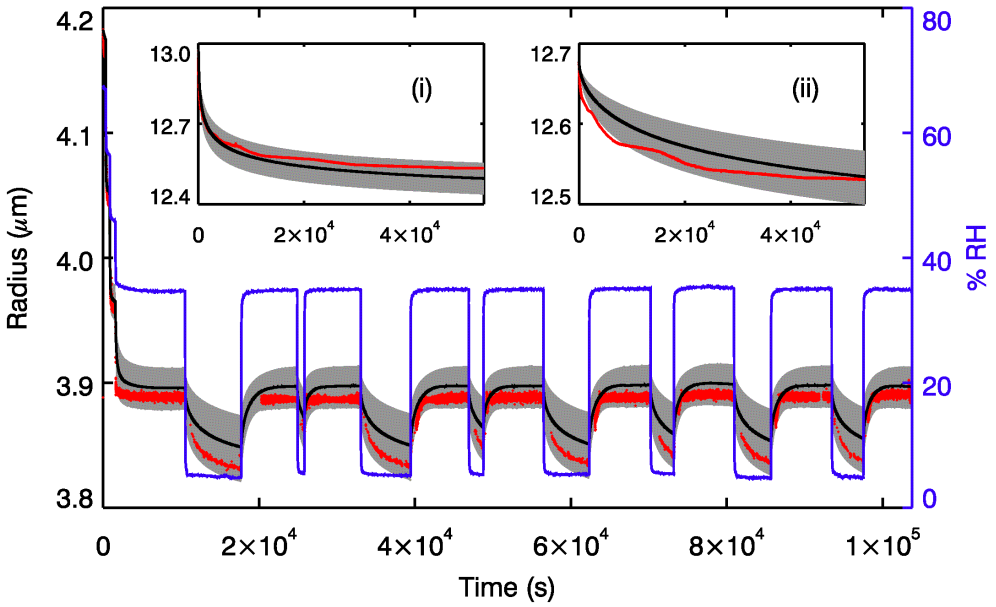

Figure 5.2: The main plot shows the changing radius of a sucrose droplet following a repeatedly stepped RH profile (blue line) at room temperature, measured using optical tweezers (red points). The same RH profile was run through the model for a droplet with 1000 shells; the output radius is shown by the black line, with the grey shaded region corresponding to the error in the measured RH of ±2%. Inset (i) shows the size change recorded in an EDB for a 13.03 µm droplet confined and equilibrated at 53% RH experiencing a rapid step change (halftime for RH change << 1 s) to 20% RH (red line). The equivalent model output is shown in black, run with 3000 shells, with the grey region corresponding to a ±2% error in starting water activity and chamber RH. Similarly, inset (ii) shows the size change recorded in an EDB for a 12.68 µm droplet confined and equilibrated at 35% RH experiencing a rapid step change to 15% RH (red line). Again, the model output is shown in black, with the grey region corresponding to a ±2% error in starting water activity and chamber RH. Uncertainties in the experimentally determined radii are estimated to be ±50 nm.

in RH. The model was set up with 150 shells and used the SOM water diffusion coefficient parameterisation given in chapter 4. Figure 5.3 shows the timescales for hygroscopic growth (upper left side of plots) and shrinkage (lower right side of plots) of the particle in response to changes from various starting RHs (x-axes, corresponding to the homogeneous starting $a_w \times 100$) to final RHs (y-axes). The time taken for the radius of the particle to increase/decrease by (a) 50% and (b) 95% of the total predicted size change is represented by the colour of each datapoint. It can be seen that water uptake and loss occur on timescales much faster than one second in these small particles, even at low RH, even though similar materials are known to have high viscosities and super-micron particles are known to shatter when subjected to mechanical force (Renbaum-Wolff *et al.*, 2013).

The first 50% of change in size occurs most rapidly in high-a_w particles when they are exposed to a sudden large decrease in RH (bottom right of fig. 5.3(a)), whereas low-a_w particles exposed to high RH are comparatively slow to take up water (top left of fig. 5.3(a)). Water can be lost rapidly from a more dilute droplet, whereas water uptake to a highly concentrated droplet is initially inhibited by low diffusion coefficients and accelerates only when enough hygroscopic growth has occurred to soften the outer layers of the particle. Low-a_w droplets experiencing small changes in RH are the slowest to complete 95% of their size change (bottom left of fig. 5.3(b)), although these are conditions where the change in composition and size are minimal.

It has been suggested that particle residence times in the dry and humid sections of a hygroscopic tandem differential mobility analyser (HTDMA; typically on the order of 10 s (Gysel *et al.*, 2004; Zardini *et al.*, 2008)) may not be sufficiently long to allow for complete equilibration of viscous aerosol water content with surrounding RH (Bones *et al.*, 2012). This could lead to erroneous measurements of the hygroscopicity parameter, κ, for example due to an over-estimation of the dry diameter in the case of incomplete water loss due to trapped water inside a glassy shell. However, fig. 5.3(b) shows that, at 280 K, 100 nm α-pinene SOM particles will complete 95% of their total size change within 0.01s for any step change in RH between 10 and 90%. Assuming that diffusion coefficients increase with increasing temperature, water diffusion in the α-pinene SOM used

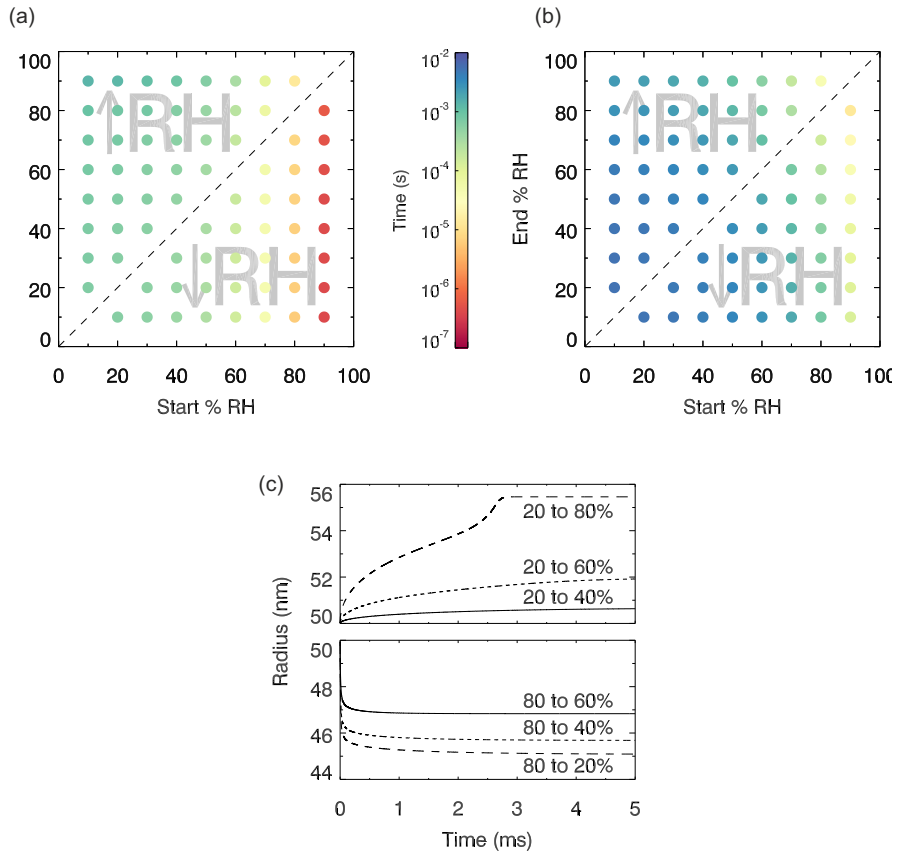

Figure 5.3: Hygroscopic growth and shrinkage times for an α-pinene SOM droplet of 100 nm starting diameter following various step changes in RH at 280 K. (a) Time for the radius to change by 50% of the total amount predicted for each RH step. (b) Time for the radius to change by 95% of the total amount predicted for each RH step. (c) Examples of size changes with time.

here is sufficiently fast at room temperature that equilibration would be achieved in an HTDMA, in agreement with previous work (Smith *et al.*, 2011). However, SOM from other sources may be considerably more viscous, with potential impacts on diffusion coefficients and therefore equilibration timescales.

Although water diffusion is fast near room temperature, timescales for equilibration increase at lower temperatures. In order to quantify this kinetic limitation, fig. 5.4 shows the output of 384 model runs where temperature is constant within a run and RH is increased by a step of 2%, over the temperature range from 220 K to 280 K. The plot shows the time taken for the water activity in the centre of a 100 nm droplet to increase by 0.01 (i.e. 50% of the change required to come back to equilibrium). At temperatures of 260 K and above, these timescales are faster than 1 s across the RH range 5% to 95%. At lower temperatures, however, slow diffusion kinetically limits the response in composition: at 240 K, the half-time for the water activity response at low RH is 3 s. The diffusion coefficient dependence on temperature is extrapolated to estimate the further increase in these timescales at upper-tropospheric temperatures. Whilst such an extrapolation should be treated with caution, it strongly suggests that diffusion is so inhibited at 220 K that small changes in water activity may take hours. Moreover, larger organic species in SOM might be expected to diffuse even more slowly than water (Abramson *et al.*, 2013). These results therefore imply that at low temperatures, equilibrium thermodynamic partitioning between condensed and gas phases may not be achieved, placing kinetic limitations on aerosol processing.

It is important to stress that timescales depend strongly on size, and increasing the starting diameter of particles in the model to 1 µm increases the timescales for diffusional mixing by a factor of 100. In the laboratory experiments, the 200 µm disc can take weeks to equilibrate with the surrounding water vapour, but a 100 nm aerosol particle of the same material under the same conditions will take less than a second to equilibrate.

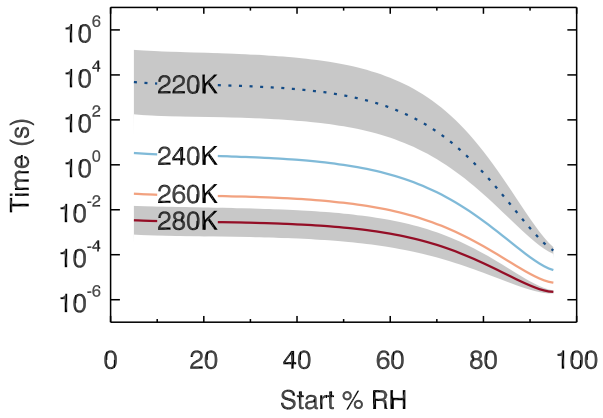

Figure 5.4: Modelled times for an increase in water activity of 0.01 at the centre of a 100 nm diameter particle following a 2% step up in RH. Below 240 K, an extrapolation of the water diffusion coefficient fit is used, indicated by a dotted line. Timescales for equivalent steps down in RH are very similar. The grey shaded region indicates the estimated uncertainty (see section 4.3.1 for details of error analysis).

5.5 Modelling aerosol water uptake in an atmospheric updraft

The multi-shell diffusion model was further configured to simulate the changing water activity of a 100 nm water-soluble α-pinene SOM particle as it was exposed to conditions equivalent to unsaturated air rising and cooling according to the dry adiabatic lapse rate (fig. 5.5 shows these profiles). Here, an extrapolation of the water diffusion coefficient parameterisation was used for trajectories starting at 220, 230 and 240 K. Figure 5.6 shows the changing water activity within the droplet for nine cases corresponding to three updraft velocities and three starting temperatures typical of synoptic cirrus formation. In each case the SOM particle starts at 20% RH, in equilibrium with the surrounding water vapour.

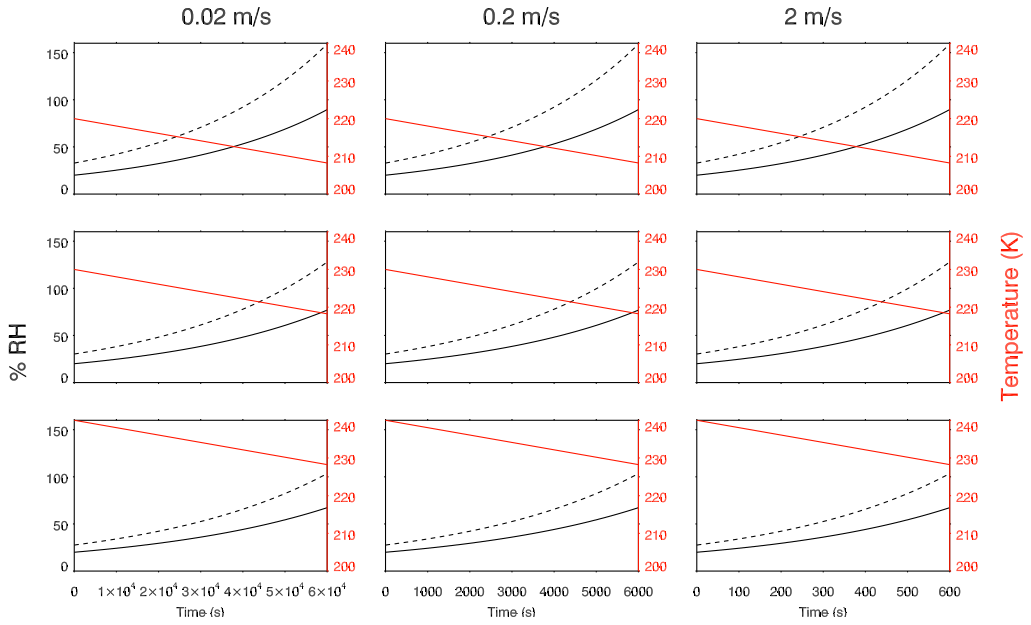

Figure 5.5: The relative humidity (black solid and dotted lines, showing RH_{liq} and RH_{ice}, respectively) and temperature (red lines) profiles used in the model simulation of aerosol water uptake in an atmospheric updraft. RH was calculated according to Murphy & Koop (2005).

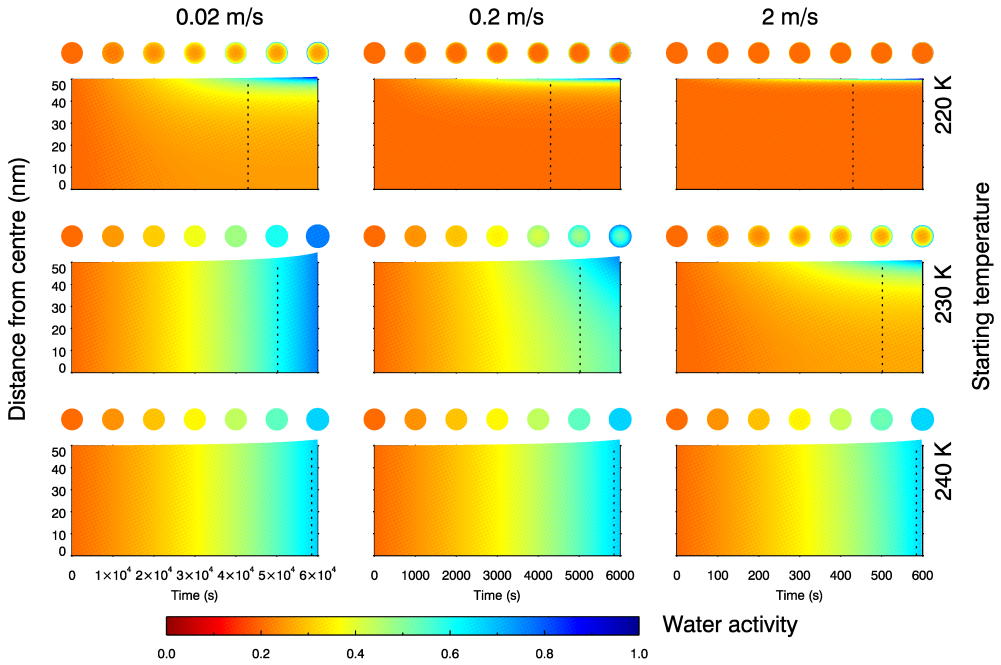

Figure 5.6: Water activity across droplet radius as a 100 nm particle follows an updraft of 0.02, 0.2 and 2 m/s (left to right) with temperature decreasing according to the dry adiabatic lapse rate and fixed water vapour partial pressure. Droplets start in equilibrium with their surrounding RH at a homogeneous water activity of 0.2, at a temperature of 220, 230 or 240 K (top to bottom). The dotted lines indicate the point at which the RHice increases above 100% and heterogeneous nucleation is feasible.

It can be seen that the faster the updraft velocity and the lower the temperature, the more marked the radial inhomogeneity in water content inside an SOM particle. A starting temperature of 230 K and updraft speed of 2 m/s, or a starting temperature of 220 K and updraft speeds between 0.02 and 2 m/s, may lead to situations in which the core of a particle remains at a low water activity when the environmental conditions are above 100% RH_{ice}. This suggests that some fraction of the water soluble component of SOM may be present in a highly viscous or glassy phase under upper tropospheric conditions relevant to synoptic cirrus formation, and hence may have the capacity to nucleate ice as observed in the laboratory (Baustian *et al.*, 2012; Murray *et al.*, 2010; Wang *et al.*, 2012; Wilson *et al.*, 2012). At higher temperatures water diffusion coefficients are rapid enough for an SOM particle to maintain equilibrium with surrounding water vapour at updraft speeds between 0.02 and 2 m/s. These liquid particles will have no amorphous solid core and therefore the mode of nucleation would change. A liquid solution droplet with no ice nucleating particles would be expected to freeze homogeneously according to the water activity criterion (Koop *et al.*, 2000).

Figure 5.6 demonstrates that SOM particle water content (and consequently phase) can be non-uniform under certain conditions, and depends on the temperature and RH history of the particle. This is consistent with the work of Berkemeier *et al.* (2014), who used estimates of diffusion coefficients to show that kinetic limitations to water diffusion may create core-shell morphologies potentially favourable for ice nucleation. In order to evaluate the impacts of SOM particles in heterogeneous and multiphase chemistry, and thus its impact on tropospheric composition, it is necessary to have a clear understanding of whether particles are present in the form of a liquid, solid or a combination of both (Bogdan *et al.*, 2010; Ravishankara, 1997). The possible presence of a highly viscous or glass phase should be borne in mind in future laboratory studies examining chemical processing in the presence of SOM.

In this work, laboratory-generated SOM is used, which has some known differences to atmospheric SOM: it is typically less oxidised and more volatile than ambient particles (Donahue *et al.*, 2012). Higher oxygen to carbon ratio in α-pinene SOM correlates with higher T_g (Berkemeier *et al.*, 2014), indicating that

atmospheric SOM may be more viscous than the SOM studied here. Recently, O'Brien *et al.* (2014) found that viscosity and/or surface tension could be higher in ambient organic particles than laboratory-generated SOM, attributing this to variations in chemical aging time and the complexity of field aerosol. Assuming that higher viscosity is associated with slower diffusion, this implies that the diffusion coefficients of water in atmospheric SOM might be lower than those measured in this laboratory study. On the other hand, the duration of the Raman diffusion experiments may lead to the unavoidable evaporation of some semi-volatile components of SOM, which may have the effect of decreasing the measured diffusion coefficients (T_g tends to increase with molar mass (Koop *et al.*, 2011), which is inverserly correlated with volatility (Shiraiwa *et al.*, 2014)). The sample used here contained only the water soluble component of SOM and was generated at low RH, from a single precursor, and this cannot necessarily be assumed to be characteristic of real atmospheric SOM. However, water-soluble material represents the major fraction of α-pinene SOM (Renbaum-Wolff *et al.*, 2013), and these results are currently the only direct measures of water diffusion in this material. The presence of less water-soluble species would reduce the hygroscopicity of SOM, possibly increasing the viscosity and decreasing diffusion coefficients by lessening the plasticising effect of water. It should be emphasized that, here, the diffusion of water has been measured, a highly mobile component, but the diffusion of larger organic molecules in SOM is much slower (Abramson *et al.*, 2013; Zhou *et al.*, 2013). This may lead to inhibition of condensed-phase chemistry in situations where water diffusion is unimpeded and cause a kinetic limitation to gas-particle partitioning of semi-volatile organic compounds. Future work should therefore focus on measuring the diffusion of larger molecules in SOM.

5.6 Summary

In this chapter, a model was described which simulates water uptake and loss in response to changing environmental conditions. The accuracy of the model was verified using laboratory data. It was then used to investigate possible kinetic limitations, or lack thereof, in SOM particles. It was shown that, although SOM can behave mechanically like a solid, at 280 K water diffusion is not kinetically

limited on timescales of 1 s for atmospheric-sized particles. For colder conditions, however, SOM may take hours to equilibrate with water vapour. Model predictions for 100 nm particles predicted that under mid to upper tropospheric conditions, radial inhomogeneities in water content produce a low viscosity surface region and more solid interior, with implications for heterogeneous chemistry and ice nucleation.

Chapter 6

Diffusion of organics in aqueous solution

Having quantified the diffusion of water, one of the most mobile components in an aqueous organic solution, it is now of interest to determine the degree to which the diffusion of larger organic molecules is inhibited at high solute concentration. Aqueous sucrose was chosen as a suitable model system, due to the extensive literature data available. As outlined in section 2.3, a Raman isotope tracer method was used to measure the diffusion of non-deuterated and deuterated sucrose across a boundary between two aqueous solutions. These results are discussed below.

6.1 Mapping diffusion across a boundary

Aqueous sucrose and deuterated sucrose droplets were placed on a hydrophobic glass slide and equilibrated in a temperature and humidity controlled chamber in a Raman microscope, as described in section 2.3. The time required for this equilibration was calculated using the diffusion coefficients of water in aqueous sucrose measured in chapter 3 together with the diffusion model described in chapter 5. Once a uniform water activity was achieved across the droplets, a second hydrophobic glass slide was placed on top, so that the solutions made contact. Diffusion proceeded across the boundary between the deuterated and non-deuterated solutions, and was monitored via the evolution of Raman spectra.

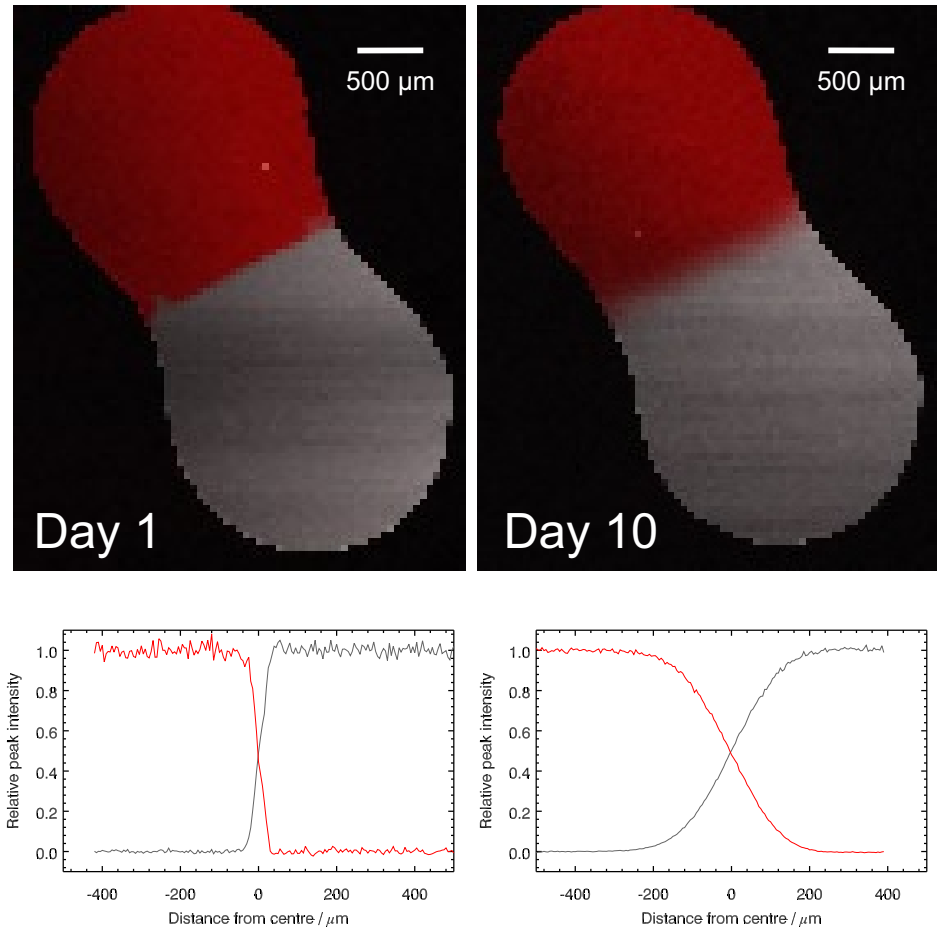

Figure 6.1: Raman maps of an aqueous non-deuterated and aqueous deuterated sucrose droplet, in contact at 60% RH. The red colour corresponds to the background-corrected intensity of the C-H stretch band, and the grey colour corresponds to the background-corrected intensity of the C-D stretch band. On intial contact (day 1), the boundary between the deuterated and non-deuterated regions is sharp. By day 10, this boundary has been broadened by diffusion. The lower plots show how the relative intensity of the C-H (red) and C-D (grey) bands change across the boundary.

Figure 6.1 shows a map of the Raman band intensities of the C-H (red) and C-D (grey) stretches, as well as plots of the relative Raman intensities as the laser tracked along a path perpendicular to the boundary. At the start of the experiment, the non-deuterated and deuterated aqueous solutions were in contact, but diffusional mixing of sucrose molecules had not yet occurred: the change from C-H to C-D between the two droplets was abrupt. As time progressed, diffusional mixing gradually caused a blurring of the boundary between the two droplets, seen by a more continuous change in colour from red to grey. Experiments to measure the diffusion coefficient of sucrose in aqueous solutions were performed at five different RHs at room temperature (see section 2.3 for details).

6.2 Analysis of Raman spectra to determine organic diffusion coefficients

A series of spectra were acquired along the perpendicular bisector to the boundary between the deuterated and non-deuterated sucrose solutions, as described in section 2.3.2. The background was subtracted from each spectrum by fitting a Gaussian curve plus a constant to the regions where no C-H, C-D or O-H peaks were present, using the Levenberg-Marquardt technique (Markwardt, 2009). This Gaussian curve was constrained in the same way as described in section 4.1: a fit to a spectrum taken of the background (the slide without the samples) determined the wavenumber and width. Each spectrum was normalised to the background-corrected intensity of the (constant) O-H band.

After a time interval (defined by the rate of diffusion - at high RHs, this was around half an hour; at low RHs this was a day) the series of spectra was collected again, and this was repeated as the interface broadened. The broadening of the boundaries between the non-deueterated and deuterated regions as time progressed is shown in fig. 6.2. Each curve was fitted according to equations 2.3 and 2.4, in order to determine the width of the interface, σ. These fits are shown in fig. 6.3. For closer comparison between the raw data with the fits, fig. 6.4 shows both on the same plot for some of the series of spectra collected at 60% RH.

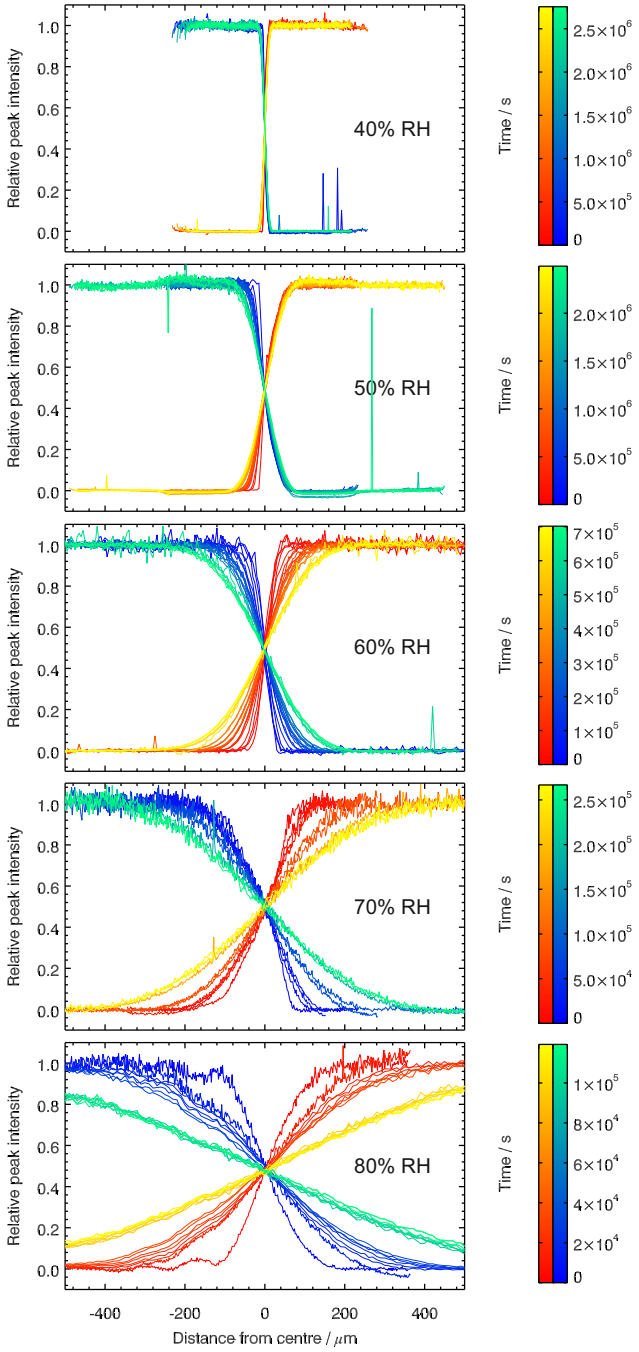

Figure 6.2: Background corrected, normalised peak intensities of the C-H (red to yellow) and C-D bands (blue to green), relative to their maxima, as time progresses after initial contact between the deuterated and non-deuterated droplets.

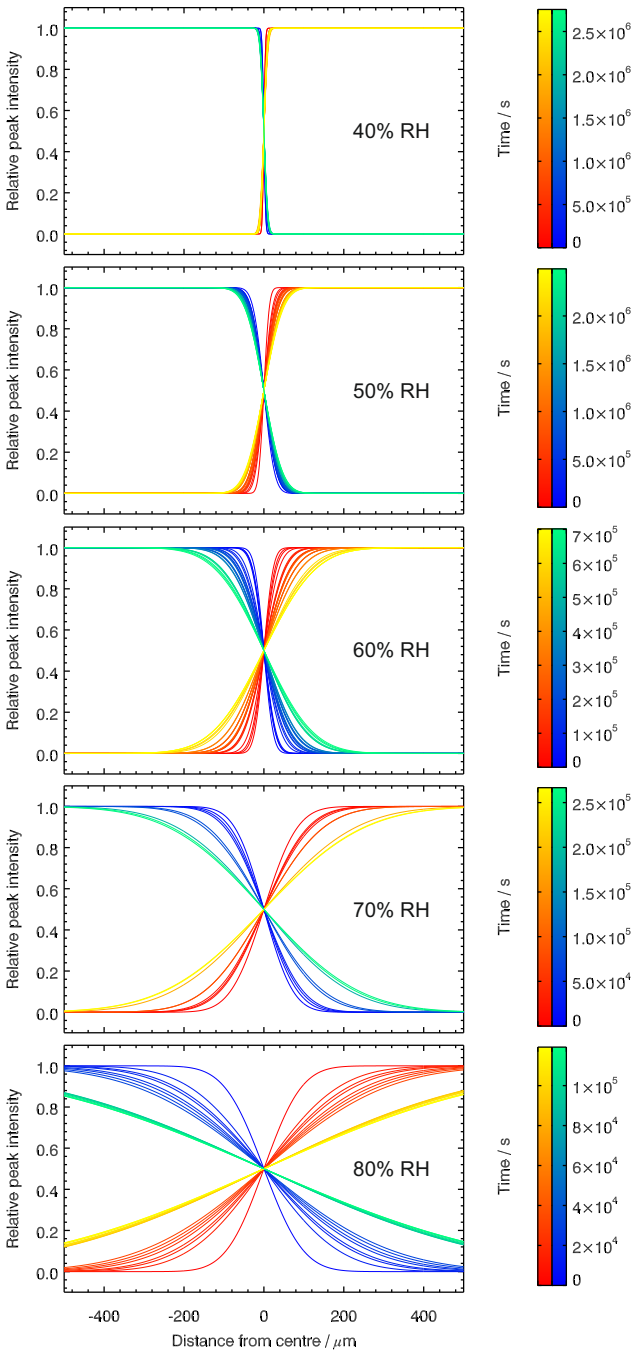

Figure 6.3: Fits to the data shown in fig. 6.2.

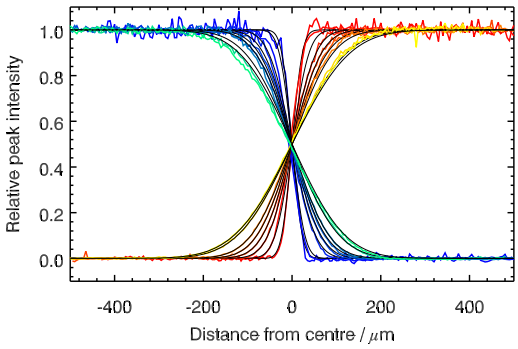

Figure 6.4: Every third series of spectra collected at 60% RH. The colour of the raw data corresponds to the normalised peak intensities of the C-H (red to yellow) and C-D bands (blue to green), relative to their maxima, as time progresses after initial contact between the deuterated and non-deuterated droplets. Fits to the data are overplotted in black.

The diffusion coefficient of sucrose, $D_{sucrose}$, was determined via the temporal evolution of σ with time:

$$\sigma^2 = \sigma_x^2 + 2Dt \tag{6.1}$$

where σ_x is the interfacial width due to the instrument's spatial resolution and t is the time since contact was made between the two droplets. The gradient of a line fitted to σ^2 *vs* time, shown in fig. 6.5, is therefore double $D_{sucrose}$. The error in each $D_{sucrose}$ measurement was calculated using the linear regression standard error in that gradient.

6.3 Sucrose diffusion coefficients

The measured diffusion coefficients of sucrose in aqueous solution are shown *vs* water activity in fig. 6.7. Also shown for comparison are the measured water diffusion coefficients in the same material (see chapter 3). Empirical fits for both sets of data, in the form of equation 3.2, are also shown, with the fitted parameters given in table 6.1.

Table 6.1: Fit parameters a to d used in equation 3.2 for $D_{sucrose}(a_w)$ in aqueous sucrose. Also shown are the fit parameters for $D_{water}(a_w)$ in the same material, reproduced from section 3.2.

	a	b	c	d
Water	-20.89	25.92	-26.97	13.25
Sucrose	-30.97	54.89	-62.34	29.12

Figure 6.6 shows how the sucrose diffusion coefficients measured in this study compare with those measured at lower concentration using NMR (Ekdawi-Sever *et al.*, 2003; Rampp *et al.*, 2000). The literature data were reported in terms of sucrose mass fraction, whereas the experimental setup used here was designed to quantify sucrose diffusion at a given water activity. Water activity is therefore converted to sucrose mass fraction for the purposes of this plot, using the two different parameterisations given by Norrish (1966) and Zobrist *et al.* (2011). Regardless of which parameterisation is used, the high sucrose mass fraction diffusion coefficients measured in this study follow on smoothly from the lower

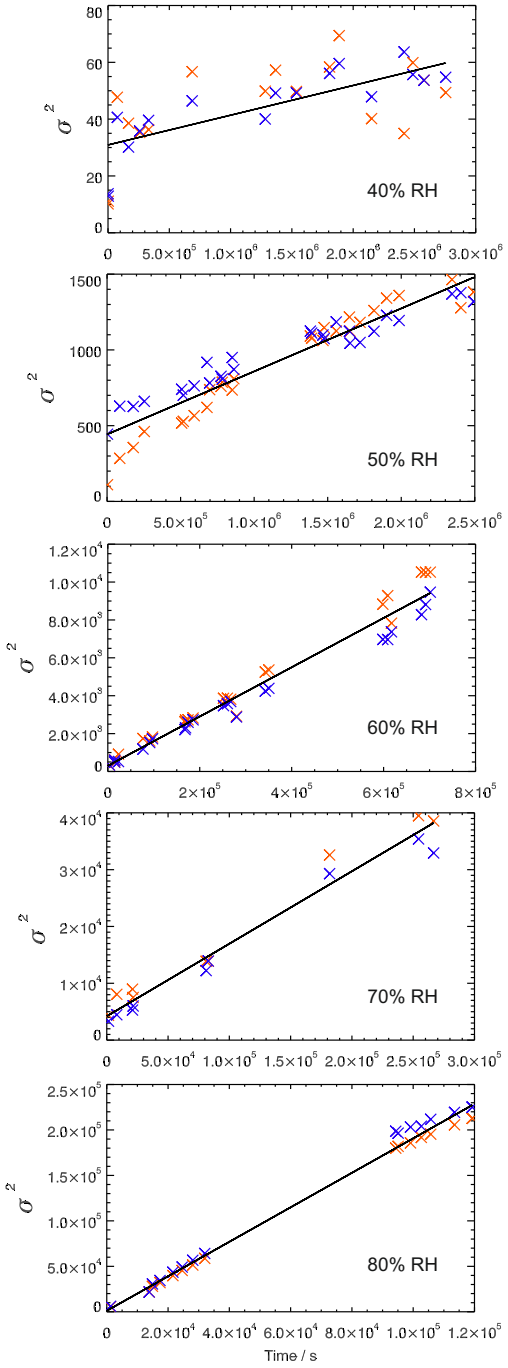

Figure 6.5: Plots of σ^2 *vs* time for the data shown in fig. 6.2. The orange datapoints represent the value of σ^2 from the fit to the normalised peak intensities of the C-H band; the blue datapoints represent these values for the C-D band. Each linear fit is performed using both the C-H and C-D data. The gradient of the linear fits is equal to double the diffusion coefficient of sucrose. The R^2 values for the lines are 0.48, 0.90, 0.97, 0.97 and 0.99 for RHs of 40, 50, 60, 70 and 80%, respectively.

sucrose mass fraction literature diffusion coefficient data. In the small region where the three datasets overlap, all measured sucrose diffusion coefficients are in good agreement.

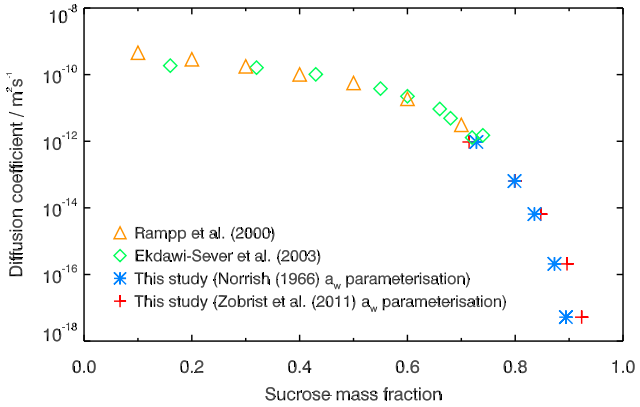

Figure 6.6: Diffusion coefficients of sucrose measured using Raman isotope tracer method at 296 K, compared with NMR measurements of sucrose diffusion by Rampp *et al.* (2000) and Ekdawi-Sever *et al.* (2003). To compare diffusion coefficients on the same scale, water activity was converted to sucrose mass fraction using either the Norrish (1966) or the Zobrist *et al.* (2011) parameterisation.

As discussed in chapters 3 and 4, the Stokes-Einstein equation that relates diffusion to viscosity is known to break down under certain conditions. Power *et al.* (2013) measured the viscosity of highly concentrated aqueous sucrose solutions at room temperature. They found that a line closely fitting their data could be producted by using the viscosity parameterisation given by Chenlo *et al.* (2002), together with the thermodynamic treatment for water activity of Norrish (1966). This line is used here to predict diffusion coefficients of water and sucrose in aqueous sucrose using the Stokes-Einstein relation, shown as dashed lines in fig. 6.7. The molecular diameters used in the Stokes-Einstein equation were 2 Å for water and 9 Å for sucrose (calculated based on the density of amorphous sucrose given by Hancock & Zografi (1997)). The breakdown of the relation for water is

highlighted by the difference between the two blue lines. At a water activity of 0.6 the relation underpredicts water diffusion by a factor of ∼100, and at a water activity of 0.4 this underprediction increases to a factor of ∼3000. Much better agreement, however, is found between the two red lines. At a water activity of 0.4 (where the error in the viscosity measurements of Power *et al.* (2013) are a factor of ∼4) the diffusion coefficient of sucrose is underpredicted by the relation by a factor of ∼6. The Stokes-Einstein equation seems to be much better able to predict sucrose diffusion than water diffusion, at least over the range of water activities studied here.

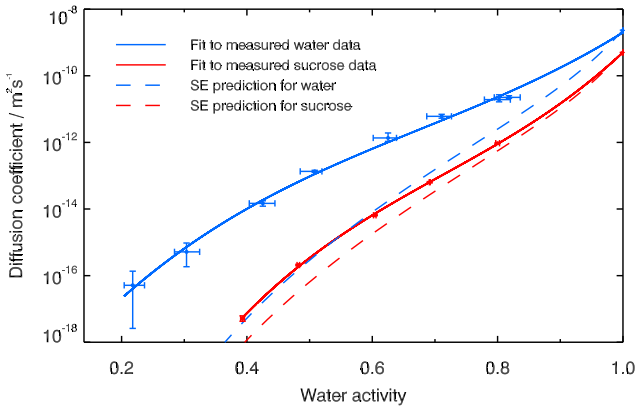

Figure 6.7: Measured diffusion coefficients of sucrose and water in aqueous sucrose at 296 K, as a function of water activity. Solid lines are empirical fits to the data, according to equation 3.2. Dashed lines show the diffusion coefficients predicted using the Stokes-Einstein (SE) equation, based on the viscosity data of Power *et al.* (2013).

The difference in diffusion coefficients of water and carbohydrate molecules in aqueous solution has been observed previously at lower solute concentrations (Ekdawi-Sever *et al.*, 2003; Rampp *et al.*, 2000). Rampp *et al.* (2000) saw the ratio of the diffusion coefficient of water to the diffusion coefficient of sucrose, α,α-trehalose, allosucrose and leucrose in their aqueous solutions increased as temperatures decreased, and speculated that this was because the water molecules were

able to diffuse through a hydrogen-bonded network formed by the carbohydrate molecules. Computational studies have suggested that water and carbohydrate molecules diffuse differently in concentrated aqueous solutions. Simulations indicate that the diffusion of carbohydrates is continuous, whilst water molecules are able to make random jumps (Ekdawi-Sever *et al.*, 2003; Molinero & Goddard III, 2005; Roberts & Debenedetti, 1999). The Stokes-Einstein description is based on macroscropic hydrodynamics and assumes the material to be a contiuum. The differences in diffusion mechanism between water and carbohydrates could therefore provide an explanation for the differing degrees to which it underpredicts the water and sucrose diffusion coefficients presented here.

6.4 Timescales for sucrose diffusion

The room temperature diffusion coefficients of water and sucrose in aqueous sucrose deviate by nearly four orders of magnitude at 40% RH. Consequently, the diffusion timescales calculated according to equation 3.3 also vary by nearly four orders of magnitude: for a 100 nm diameter particle, the half-time for sucrose diffusion is ∼100 s, whereas water diffusion occurs on timescales much faster than 1 s.

If the diffusion of organic molecules in atmospheric aerosol is similar to that of sucrose in aqueous sucrose, then these long timescales could have important implications for particle-phase chemistry and the kinetics of gas-particle partitioning. Slow diffusion of reactants between the bulk of an aerosol particle and its surface could inhibit oxidation. The slow diffusion of large molecules which condense from the vapour phase onto aerosol particles could lead to radial inhomogeneities in the concentrations of different sized molecules. Smaller molecules would be preferentially able to diffuse into the bulk of a particle, whilst larger ones are are unable to diffuse from the surface inwards. Similarly, there may be a kinetic limitation to the evaporation of large organic molecules because they are slow to diffuse from the interior of a particle to its surface. To fully understand this requires the application of a multi-layer kinetics model, which is beyond the scope of this work.

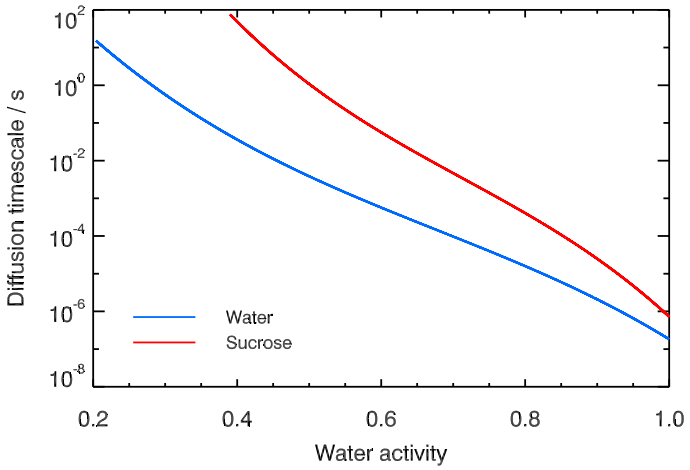

Figure 6.8: Diffusion timescales for sucrose and water molecules in aqueous sucrose at 296 K, as a function of water activity, predicted using fits to the diffusion coefficient data and equation 3.3.

6.5 Comparison of diffusion coefficients, viscosity and rebound in aqueous sucrose

Bateman *et al.* (2014b) use an impaction apparatus to measure the rebound fraction of aqueous sucrose droplets at room temperature as a function of RH. In light of the new diffusion measurements given above, it is now possible to correlate this rebound with diffusion coefficients for water and sucrose, and viscosity, as shown in fig. 6.9. It can be seen that there is a sharp transition in rebound fraction between 70 and 75% RH, where the diffusion coefficient of water is $\sim 10^{-11}$ $m^2 s^{-1}$, the diffusion coefficient of sucrose is $\sim 10^{-13}$ $m^2 s^{-1}$ and the viscosity is ~ 5 Pa·s.

Figure 4.9 hinted that there may be a correlation between rebound fraction and water diffusion. It is likely that this correlation is because both properties are linked to viscosity. Given that sucrose diffusion is also connected to viscosity, a correlation between rebound fraction and organic diffusion may also exist (a lack of organic diffusion coefficient data in other materials prevents the testing of this at present). Rebound measurements are much faster than the diffusion ex-

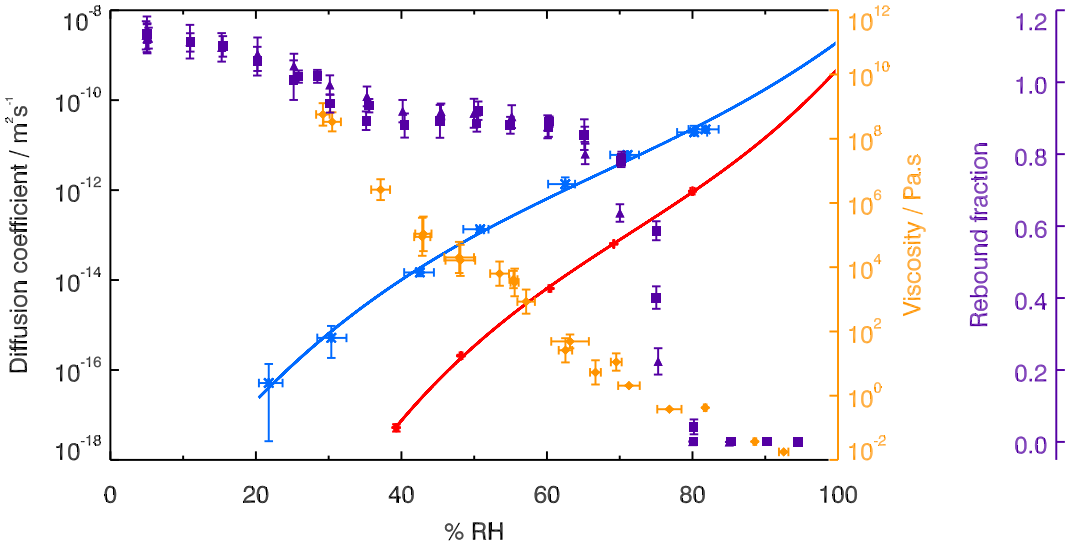

Figure 6.9: Diffusion coefficients for water (blue crosses) and sucrose (red plus signs) in aqueous sucrose, plotted against relative humidity and compared with viscosity measurements from Power *et al.* (2013) (orange diamonds) and rebound fractions measured by Bateman *et al.* (2014b) (purple squares for 190 nm particles, purple triangles for 240 nm particles).

periments presented in this work, and are not limited by the requirement to work with large quantities of materials. A correlation between bounce and diffusion or viscosity would therefore provide an avenue to obtain quantitative information about particle phase and kinetics on more materials than it would be possible to investigate using resource-intensive techniques. However, this should be approached with caution: fig. 4.9 is only for three materials, two of which are binary aqueous solutions which may or may not be appropriate proxies for the complex mixtures that make up atmospheric aerosol. Extensive measurements would be needed to test for correlation in a wide range of materials before any firm conclusions could be drawn.

6.6 Organic diffusion in α-pinene SOM

Very limited literature data are available for organic diffusion in SOM. Abramson *et al.* (2013) estimated the diffusion coefficient of pyrene based on its evaporation kinetics from α-pinene SOA formed in its presence. Zhou *et al.* (2013) coated benzo[*a*]pyrene (BaP) / ammonium sulphate particles with α-pinene SOM and monitored the loss of BaP via its reaction with ozone, estimating its diffusion coefficient by simulating the kinetics using a multi-layer model. These two sets of data are shown in table 6.2, together with diffusion timescales calculated according to equation 3.3 for 100 nm diameter particles.

Also shown in table 6.2 are the viscosity values measured by Renbaum-Wolff *et al.* (2013), which are converted here to diffusion coeffcients using the Stokes-Einstein equation. Based on their molar masses (202.25 and 252.31 g/mol) and densities (1.27 and 1.24 g/cm^3), the molecular diameters of pyrene and BaP are estimated to be 8 and 9 Å, repectively. By comparing the upper and lower parts of table 6.2, it can be seen that the Stokes-Einstein relationship works for BaP diffusion in α-pinene SOM at 50% RH (although the wide uncertainty range in viscosity makes this perhaps unsurprising). The relationship also almost works at 70% RH. However, it seems to break down under dry conditions, with the diffusion coefficients predicted from viscosity measurements being lower than those inferred from kinetics measurements. For pyrene, the characteristic diffusion timescale in α-pinene SOM under dry conditions based on evaporation kinetics

is approximately 2 days, whereas it is around 5 days or more based on viscosity measurements. The discrepancies for BaP in α-pinene SOM at low RH are even larger, ranging from minutes to days.

It should be noted that it is not clear whether these differences are in fact due to a breakdown of the Stokes-Einstein relation, or are a result of the use of diffusion coefficient estimates with unspecified uncertainties. The available data are sparse and it is thus difficult to draw conclusions at this point. Kidd *et al.* (2014a) found that the relative magnitudes of the diffusion coefficients of pinonaldehyde and acetic acid were consistent with the size difference between the molecules (i.e. the ratio of the diffusion coefficients is similar to the ratio of the molecular radii). This, together with the apparent success of the Stokes-Einstein relation for pyrene in SOM at higher RHs (and for sucrose in aqueous solution shown earlier in this chaper), indicates that more research in this area is warranted.

6.7 Summary

This chapter has reported measurements of sucrose diffusion coefficients in aqueous solution between 40 and 80% RH at room temperature. These diffusion coefficients are significantly lower than those of water in the same material under the same conditions, and subsequently the diffusion timescales of sucrose are predicted to be much larger than those of water. A comparison of sucrose and water diffusion data with viscosity and rebound measurements in aqueous sucrose showed that a sharp transition in rebound fraction is not accompanied by a sharp transition in the log of solute or solvent diffusion, or the log of viscosity.

In aqueous sucrose, the Stokes-Einstein equation was found to be much more successful in predicting organic diffusion than water diffusion using viscosity data. A review of the available literature data for the diffusion of organics in secondary organic material found that the Stokes-Einstein relation is, again, more promising for organics than for water.

The measurements of water and sucrose diffusion in aqueous sucrose presented here are the first of their kind in this binary solution at high solute concentration. They therefore provide a valuable means to study diffusion in a simple but

Table 6.2: Room temperature diffusion coefficients of pyrene and BaP in α-pinene SOM measured by Abramson *et al.* (2013); Zhou *et al.* (2013), and predicted using the Stokes-Einstein relationship with viscosity measurements from Renbaum-Wolff *et al.* (2013) and molecular diameters of 8 Å and 9 Å for pyrene and BaP, respectively. Timescales are calculated for 100 nm droplet using equation 3.3.

Diffusion measurements				
% RH	D_{pyrene} ($m^2 s^{-1}$)	D_{BaP} ($m^2 s^{-1}$)	$\tau_{\frac{1}{2},pyrene}$ (s)	$\tau_{\frac{1}{2},BaP}$ (s)
<5	2.5×10^{-21}	2×10^{-18}	150000 s	200 s
50		8×10^{-18}		50 s
70		$> 1 \times 10^{-16}$		4 s

Viscosity measurements					
% RH	η (Pa·s)	$D_{pyrene,SE}$ ($m^2 s^{-1}$)	$D_{BaP,SE}$ ($m^2 s^{-1}$)	$\tau_{\frac{1}{2},pyrene,SE}$ (s)	$\tau_{\frac{1}{2},BaP,SE}$ (s)
<5	$> 5 \times 10^8$	$< 1 \times 10^{-21}$	$< 1 \times 10^{-21}$	> 400000	> 400000
50	378–5.19×10^5		9.60×10^{-19}–1.32×10^{-15}		0.277–381
70	791–1520		3.28×10^{-16}–1.21×10^{-15}		0.302–1.11

widely used material. Future work should focus on comparing these results with rotational diffusion, relaxation and translational diffusion of other molecules in this material, in order to discern more information about the fundamental nature of diffusion.

Chapter 7

Conclusions

7.1 Summary of major findings

The existence of aerosol particles as highly viscous liquids and amorphous solids may have a profound effect on their interactions with water vapour and other chemical species in the atmosphere. It is therefore important to quantify diffusion in ultra-viscous and amorphous solid states. In this work, experimental methods for quantifying the diffusion of water and organic molecules in aqueous solutions have been developed. These methods make use of Raman microscopy to monitor the diffusion of isotope tracers, across a range of environmental conditions, and produce diffusion coefficients in good agreement with the available literature data. Diffusion coefficients between $\sim 10^{-18}$ to $\sim 10^{-10}$ $m^2 s^{-1}$ are reported; this range corresponds to solutions from the glassy to liquid states. To relate the measured diffusion coefficients to atmospheric processes, a multi-shell water diffusion model was also developed and validated against laboratory measurements of hygroscopic growth.

New data for room temperature water diffusion coefficients in aqueous solutions of sucrose, $MgSO_4$, levoglucosan and a mixture of raffinose, carboxylic acids and ammonium sulphate are presented. Also reported are the first direct measurements of the diffusion coefficients of water in the water soluble component of α-pinene secondary organic material (SOM) over a range of temperature and relative humidity conditions. Using these measured water diffusion coefficients, it was predicted that water diffusion timescales for aerosol-sized particles (∼100

nm) of aqueous sucrose at room temperature just below the glass transition are on the order of minutes. This is a vastly shorter timescale than one would expect based on the Stokes-Einstein equation, which has been used to relate diffusion to viscosity in the past. It was shown for levoglucosan, sucrose and SOM that a high bounce fraction does not necessarily mean long water diffusion timescales. The multi-shell water diffusion model was used with the SOM diffusion coefficients to predict how kinetic limitations might affect secondary organic aerosol behaviour in the atmosphere. It was shown that water diffusion is not kinetically limited in the water-soluble component of α-pinene SOM at 280 K for 100 nm particles, but slows dramatically as temperatures decrease. Under conditions relevant to the upper troposphere, radial variations in phase develop which may have important consequences for aerosol chemistry and ice nucleation.

Finally, sucrose diffusion coefficients were quantified in aqueous sucrose. At room temperature and 40% RH, the diffusion coefficient of sucrose was found to be approximately four orders of magnitude smaller than that of water in the same material. Slow organic diffusion may have important implications for aerosol growth, chemistry and evaporation, where processes may be limited by the inability of a molecule to diffuse between the bulk and the surface of a particle. Using the viscosity data of Power *et al.* (2013), it was shown that, although inappropriate for the prediction of water diffusion, the Stokes-Einstein equation works well for predicting sucrose diffusion under the conditions studied.

7.2 The relationship between diffusion coefficients with ice nucleation measurements

The low-temperature diffusion coefficients measured in this work and used in the water diffusion model confirm what was suggested by Berkemeier *et al.* (2014) - kinetic limitations to water uptake could affect the ice nucleation mechanism of these particles. They also provide insight into the ice nucleating abilities of α-pinene SOM observed by Möhler *et al.* (2008) and Ladino *et al.* (2014).

Möhler *et al.* (2008) observed ice nucleation near to the predicted homogeneous nucleation threshold above which a solution in equilibrium with gas phase

water would freeze homogeneously. Given that the experiments they described were for a situation similar to the top right hand plot of fig. 5.6, only at lower temperatures, it would seem unlikely that these particles took up water rapidly enough to equilibrate with their surroundings during cooling. It was only at an RH_{ice} of around 200%, above water saturation, that more than 2% of the particles were ice-active, indicating that the SOA was indeed very slow to take up water. Because these conditions are above the homogeneous ice nucleation threshold, it is not possible to say for certain whether the nucleation was heterogeneous (i.e. nucleation of a low viscosity surface region on a core of highly viscous material with low water diffusion coefficient) or homogeneous (i.e. nucleation of either an entirely liquid aqueous droplet or the homogeneous nucleation of an aqueous liquid film surrounding a glassy core).

Ladino *et al.* (2014) saw ice nucleation thresholds for α-pinene SOM below 230 K that were at a higher RH_{ice} than the homogeneous freezing line given by Koop *et al.* (2000). The authors suggest that either these froze homogeneously, or a kinetic limitation to diffusion within the particles meant that water uptake was delayed, leading to the nucleation of ice via the deposition mode. Again, the modelling presented in chapter 5 indicates that water diffusion at these temperatures may indeed be slow enough that kinetic limitations result in the presence of a core of low diffusivity material with a less solid exterior, the latter of which may be able to freeze heterogeneously or homogeneously. Figure 5.4 indicates that the timescales for water diffusion at these temperatures are on the order or hundreds of seconds or more, with timescales increasing as temperatures decrease. The distance of the freezing observed by Ladino *et al.* (2014) from the homogeneous line increases with decreasing temperature, reinforcing the idea of a kinetic limitation to water uptake in these particles which becomes more pronounced as temperature decreases. It should be noted, however, that the temperature region used in the literature work was far outside of the experimental range used here, so caution should be exercised when drawing firm conclusions from such an extrapolation.

7.3 Implications for aerosol evaporation, mixing and chemistry

The diffusion coefficients of water in α-pinene SOM presented in this work indicate that the evaporation of small molecules from this material at room temperature is unlikely to be kinetically hindered by their diffusion, even at low RH. If small molecules are seen to evaporate slowly, it is more likely to be due to a slow evaporative flux into the gas phase due to low volatility or mixing (see for example Cappa & Wilson (2011); Saleh *et al.* (2013)). On the other hand, the results presented in chapter 6 indicate that equilibration of larger molecules from organic aerosol may be kinetically limited by slow diffusion, particularly under dry conditions: for 100 nm particles of aqueous sucrose, diffusion timescales are on the order of hundreds of seconds at 40% RH and room temperature. As RH and temperature decrease, these timescales will increase.

Loza *et al.* (2013) hypothesized that, because SOM formed sequentially from two precursors evaporated like SOM from the second precursor, the two types of SOM did not mix due to slow diffusion under dry conditions. If the diffusion coefficients of organic molecules in the SOM used in the study are similar to those of sucrose in aqueous sucrose, it is conceivable that their diffusion was slow enough to inhibit mixing on the timescale of these experiments (hours). However, the diffusion of small molecules such as water is still likely to have been fast, suggesting that there may have been some other barrier to mixing of the two materials. In order to fully comprehend the results of these experiments, quantitative data for the diffusion coefficients of organics in SOM are required.

If it can be assumed that the diffusion coefficient of water is similar to that of atmospheric oxidants such as ozone and OH, the results presented here could also provide insight into chemical reactions in organic aerosol. However, this interpretation is not straightforward. The dependence on diffusion of aerosol chemistry will vary between reactions. Diffusion is, of course, not the only factor in determining transport within aerosol particles: oxidants which react quickly with organic material will be unable to diffuse far into a particle even if their diffusion coefficient is high. A reaction in which organic reactants need to diffuse from the bulk of an aerosol particle to replenish those lost at the surface would

be greatly influenced by the organic diffusion coefficient. On the other hand, a reaction occurring throughout the bulk of a particle may be limited by any slow diffusion of oxidants from the surface into the particle. This work shows that water diffusion in flow-tube-generated α-pinene SOM is fast at temperatures above 280 K, implying that the diffusion of other small molecules would also be fast. In this material, therefore, the slow diffusion of small molecules is unlikely to be a factor greatly influencing the reactivity. Diffusion of larger organic molecules, though, can be presumed to be much slower and so could play an important role.

As discussed in chapter 1, recent work appears to suggest that ozonolysis is delayed by an SOM coating (Weitkamp *et al.*, 2008a; Zhou *et al.*, 2013) whereas OH oxidation is not (Kolesar *et al.*, 2014; Weitkamp *et al.*, 2008b). Kolesar *et al.* (2014) suggest that organic radicals produced by the surface reaction between SOM and OH are able to chemically migrate towards the core, uninhibited by any slow physical diffusion. Whilst this may be the case, it is interesting to note that the results presented here imply that there is no kinetic limitation to water transport in SOM on these length scales at room temperature (in fact, the diffusion coefficients are several orders of magnitude away from this being a possibility). This in turn implies that there is unlikely to be a significant diffusion limitation to ozone or OH diffusion in this material. The question therefore remains as to why ozonolysis of core material is slowed by an SOM coating. Unless ozone diffusion is dramatically slower than water, it seems unlikely that slow diffusion of the oxidant through the SOM coating is slowing the reaction with the core.

If both ozone and OH diffusion are fast, one potential way of rationalising these observations is to consider the role of organic diffusion. Houle *et al.* (2015) propose a measure of the thickness of material in an aerosol particle accessible to a reacting molecule that depends on the diffusion coefficient of the organic and the reactive collision frequency of the oxidant with the surface of the particle. This reactive-diffusive length is determined by the time taken for organic molecules to move within the aerosol particle and the time between reactive collisions—the organic molecules that can participate in the reaction are those which can reach the surface in a short space of time relative to the collision frequency. If the partial pressure of the oxidant is low, then the frequency of reactive collisions is low and

more organic molecules can reach the surface in the time between collisions, and thus the reactive-diffusive length is longer. Partial pressures of ozone are typically higher by several orders of magnitude than those of OH, both in the troposphere (Wayne, 2000) and in laboratory experiments (for example see Zhou *et al.* (2013) and Kolesar *et al.* (2014)). By making the simplifying assumption that an ozone collision is roughly as likely to result in a reaction as an OH collision, a possible difference in the relative importance of organic diffusion in these reactions can be inferred. When oxidant partial pressure is high, collisions with the particle are frequent, and so the diffusion of organics to the surface from the bulk is the rate-limiting factor; when oxidant partial pressure is low, the reactive-diffusive length is long and all of the organic material in the particle can be viewed as having access to the gas phase. In this way, slow diffusion of organic molecules through SOM could be more important for ozonolysis than OH oxidation.

7.4 Future work

There are likely to be differences between the diffusion properties of ambient organic aerosol particles and different SOM samples generated in the laboratory (O'Brien *et al.*, 2014). Particle physico-chemical behaviour can be determined by its RH and temperature history, and the phase and composition of SOM is affected by the RH of formation. For example, Kidd *et al.* (2014b) found that particles formed at low RH were more solid when subsequently exposed to high RH conditions, and Wilson *et al.* (2014) found that the RH at which a particle is aged affects its volatility. Temperature is known to affect the natural aerosol mass yield and particle number size distribution over the boreal forest (Liao *et al.*, 2014), whilst the inorganic material found in natural aerosol (Murphy *et al.*, 2006) may alter diffusive properties. Abramson *et al.* (2013) noted that the diffusion coefficient of pyrene in SOM decreased as the particles were aged. More work, particularly laboratory and field measurements, is therefore needed to determine how both water and organic diffusion in SOM change with age, composition and formation conditions.

Despite the limitations to the experiments performed here, these results facilitate a more directed approach to studying aerosol kinetics. Given that the

measured water diffusion timescales for SOA are very fast at warm temperatures, research can now be focussed on finding alternative explanations for the slow evaporation and delayed chemistry observed in these particles.

References

Abbatt, J., Lee, A. & Thornton, J. (2012). Quantifying trace gas uptake to tropospheric aerosol: recent advances and remaining challenges. *Chemical Society Reviews*, **41**, 6555–6581. 1

Abramson, E., Imre, D., Beránek, J., Wilson, J. & Zelenyuk, A. (2013). Experimental determination of chemical diffusion within secondary organic aerosol particles. *Physical Chemistry Chemical Physics*, **15**, 2983–2991. 11, 17, 84, 89, 104, 106, 113

Adler, G., Koop, T., Haspel, C., Taraniuk, I., Moise, T., Koren, I., Heiblum, R.H. & Rudich, Y. (2013). Formation of highly porous aerosol particles by atmospheric freeze-drying in ice clouds. *Proceedings of the National Academy of Sciences*, **110**, 20414–20419. 10

Adler, G., Haspel, C., Moise, T. & Rudich, Y. (2014). Optical extinction of highly porous aerosol following atmospheric freeze-drying. *Journal of Geophysical Research: Atmospheres*, **119**, 6768–6787. 10

Ahlqvist, M.U. & Taylor, L.S. (2002). Water diffusion in hydrated crystalline and amorphous sugars monitored using H/D exchange. *Journal of Pharmaceutical Sciences*, **91**, 690–698. 21

Aiken, A.C., DeCarlo, P.F. & Jimenez, J.L. (2007). Elemental analysis of organic species with electron ionization high-resolution mass spectrometry. *Analytical Chemistry*, **79**, 8350–8358. 65

Aiken, A.C., Decarlo, P.F., Kroll, J.H., Worsnop, D.R., Huffman, J.A., Docherty, K.S., Ulbrich, I.M., Mohr, C., Kimmel, J.R.,

Sueper, D. *et al.* (2008). O/C and OM/OC ratios of primary, secondary, and ambient organic aerosols with high-resolution time-of-flight aerosol mass spectrometry. *Environmental Science & Technology*, **42**, 4478–4485. 65

Angell, C.A. (1995). Formation of glasses from liquids and biopolymers. *Science*, **267**, 1924–1935. 63

Angell, C.A., Ngai, K.L., McKenna, G.B., McMillan, P.F. & Martin, S.W. (2000). Relaxation in glassforming liquids and amorphous solids. *Journal of Applied Physics*, **88**, 3113–3157. 6

Bahreini, R., Keywood, M., Ng, N., Varutbangkul, V., Gao, S., Flagan, R., Seinfeld, J., Worsnop, D. & Jimenez, J. (2005). Measurements of secondary organic aerosol from oxidation of cycloalkenes, terpenes, and m-xylene using an Aerodyne aerosol mass spectrometer. *Environmental Science & Technology*, **39**, 5674–5688. 6

Bartell, L. & Roskos, R. (1966). Isotope effects on molar volume and surface tension: simple theoretical model and experimental data for hydrocarbons. *The Journal of Chemical Physics*, **44**, 457–463. 31

Bateman, A.P., Belassein, H. & Martin, S.T. (2014a). Impactor apparatus for the study of particle rebound: Relative humidity and capillary forces. *Aerosol Science and Technology*, **48**, 42–52. 16

Bateman, A.P., Bertram, A.K. & Martin, S.T. (2014b). Hygroscopic influence on the semisolid-to-liquid transition of secondary organic materials. *The Journal of Physical Chemistry A*, **119**, 4386–4395. xvii, xix, xxii, 8, 51, 52, 69, 71, 102, 103

Baustian, K., Wise, M. & Tolbert, M. (2010). Depositional ice nucleation on solid ammonium sulfate and glutaric acid particles. *Atmospheric Chemistry and Physics*, **10**, 2307–2317. 21

Baustian, K., Wise, M., Jensen, E., Schill, G., Freedman, M. & Tolbert, M. (2013). State transformations and ice nucleation in amorphous (semi-) solid organic aerosol. *Atmospheric Chemistry and Physics*, **13**, 5615–5628. 9, 21

Baustian, K.J., Cziczo, D.J., Wise, M.E., Pratt, K.A., Kulkarni, G., Hallar, A. & Tolbert, M.A. (2012). Importance of aerosol composition, mixing state, and morphology for heterogeneous ice nucleation: A combined field and laboratory approach. *Journal of Geophysical Research: Atmospheres (1984–2012)*, **117**, D06217. 21, 88

Berkemeier, T., Shiraiwa, M., Pöschl, U. & Koop, T. (2014). Competition between water uptake and ice nucleation by glassy organic aerosol particles. *Atmospheric Chemistry and Physics*, **14**, 12513–12531. xviii, xix, 17, 66, 67, 68, 69, 70, 88, 109

Bodsworth, A., Zobrist, B. & Bertram, A.K. (2010). Inhibition of efflorescence in mixed organic–inorganic particles at temperatures less than 250 K. *Physical Chemistry Chemical Physics*, **12**, 12259–12266. 3

Bogdan, A., Molina, M.J., Tenhu, H., Mayer, E. & Loerting, T. (2010). Formation of mixed-phase particles during the freezing of polar stratospheric ice clouds. *Nature Chemistry*, **2**, 197–201. 88

Bones, D.L., Reid, J.P., Lienhard, D.M. & Krieger, U.K. (2012). Comparing the mechanism of water condensation and evaporation in glassy aerosol. *Proceedings of the National Academy of Sciences*, **109**, 11613–11618. 7, 82

Boucher, O., Randall, D., Artaxo, P., Bretherton, C., Feingold, G., Forster, P., Kerminen, V.M., Kondo, Y., Liao, H., Lohmann, U., Rasch, P., Satheesh, S., Sherwood, S., Stevens, B. & Zhang, X. (2013). Clouds and aerosols. In T. Stocker, D. Qin, G.K. Plattner, M. Tignor, S. Allen, J. Boschung, A. Nauels, Y. Xia, V. Bex & P. Midgley, eds., *Climate Change 2013: The Physical Science Basis. Contribution of Working Group I to the Fifth Assessment Report of the Intergovernmental Panel on Climate*

Change, 571–658, Cambridge University Press, Cambridge, United Kingdom and New York, NY, USA. 1, 3

Bowman, F. (1958). *Introduction to Bessel functions*. Courier Dover Publications. 26

Cappa, C.D. & Wilson, K. (2011). Evolution of organic aerosol mass spectra upon heating: implications for OA phase and partitioning behavior. *Atmospheric Chemistry and Physics*, **11**, 1895–1911. 11, 12, 111

Carslaw, K., Boucher, O., Spracklen, D., Mann, G., Rae, J., Woodward, S. & Kulmala, M. (2010). A review of natural aerosol interactions and feedbacks within the Earth system. *Atmospheric Chemistry and Physics*, **10**, 1701–1737. 1

Champion, D., Hervet, H., Blond, G., Le Meste, M. & Simatos, D. (1997). Translational diffusion in sucrose solutions in the vicinity of their glass transition temperature. *The Journal of Physical Chemistry B*, **101**, 10674–10679. 16, 55, 67

Chan, C.K., Flagan, R.C. & Seinfeld, J.H. (1998). In situ study of single aqueous droplet solidification of ceramic precursors used for spray pyrolysis. *Journal of the American Ceramic Society*, **81**, 646–648. 55

Chan, L.P. & Chan, C.K. (2012). Roles of the phase state and water content in ozonolysis of internal mixtures of maleic acid and ammonium sulfate particles. *Aerosol Science and Technology*, **46**, 781–793. 13

Chang, I. & Sillescu, H. (1997). Heterogeneity at the glass transition: Translational and rotational self-diffusion. *The Journal of Physical Chemistry B*, **101**, 8794–8801. 5

Chenlo, F., Moreira, R., Pereira, G. & Ampudia, A. (2002). Viscosities of aqueous solutions of sucrose and sodium chloride of interest in osmotic dehydration processes. *Journal of Food Engineering*, **54**, 347–352. 99

Cicerone, M.T. & Ediger, M. (1996). Enhanced translation of probe molecules in supercooled o-terphenyl: Signature of spatially heterogeneous dynamics? *The Journal of Chemical Physics*, **104**, 7210–7218. 6

Davies, J.F., Haddrell, A.E., Miles, R.E., Bull, C.R. & Reid, J.P. (2012a). Bulk, surface, and gas-phase limited water transport in aerosol. *The Journal of Physical Chemistry A*, **116**, 10987–10998. 55

Davies, J.F., Haddrell, A.E. & Reid, J.P. (2012b). Time-resolved measurements of the evaporation of volatile components from single aerosol droplets. *Aerosol Science and Technology*, **46**, 666–677. 80

Debenedetti, P.G. & Stillinger, F.H. (2001). Supercooled liquids and the glass transition. *Nature*, **410**, 259–267. 6, 16

Dennis-Smither, B.J., Miles, R.E. & Reid, J.P. (2012). Oxidative aging of mixed oleic acid/sodium chloride aerosol particles. *Journal of Geophysical Research: Atmospheres (1984–2012)*, **117**, D20204. 80

Dette, H.P., Qi, M., Schrder, D.C., Godt, A. & Koop, T. (2014). Glass-forming properties of 3-methylbutane-1,2,3-tricarboxylic acid and its mixtures with water and pinonic acid. *The Journal of Physical Chemistry A*, **118**, 7024–7033. 8

Donahue, N.M., Henry, K.M., Mentel, T.F., Kiendler-Scharr, A., Spindler, C., Bohn, B., Brauers, T., Dorn, H.P., Fuchs, H., Tillmann, R. *et al.* (2012). Aging of biogenic secondary organic aerosol via gas-phase OH radical reactions. *Proceedings of the National Academy of Sciences*, **109**, 13503–13508. 88

Duplissy, J., DeCarlo, P.F., Dommen, J., Alfarra, M.R., Metzger, A., Barmpadimos, I., Prevot, A.S., Weingartner, E., Tritscher, T., Gysel, M. *et al.* (2011). Relating hygroscopicity and composition of organic aerosol particulate matter. *Atmospheric Chemistry and Physics*, **11**, 1155–1165. 65

REFERENCES

Edmond, K.V., Elsesser, M.T., Hunter, G.L., Pine, D.J. & Weeks, E.R. (2012). Decoupling of rotational and translational diffusion in supercooled colloidal fluids. *Proceedings of the National Academy of Sciences*, **109**, 17891–17896. 5

Ehn, M., Thornton, J.A., Kleist, E., Sipilä, M., Junninen, H., Pullinen, I., Springer, M., Rubach, F., Tillmann, R., Lee, B. *et al.* (2014). A large source of low-volatility secondary organic aerosol. *Nature*, **506**, 476–479. 8, 12

Ekdawi-Sever, N., de Pablo, J.J., Feick, E. & von Meerwall, E. (2003). Diffusion of sucrose and α, α-trehalose in aqueous solutions. *The Journal of Physical Chemistry A*, **107**, 936–943. xvi, xxii, 47, 48, 97, 99, 100, 101

Engelhart, G., Asa-Awuku, A., Nenes, A. & Pandis, S. (2008). CCN activity and droplet growth kinetics of fresh and aged monoterpene secondary organic aerosol. *Atmospheric Chemistry and Physics*, **8**, 3937–3949. 65

Freedman, M.A., Baustian, K.J., Wise, M.E. & Tolbert, M.A. (2010). Characterizing the morphology of organic aerosols at ambient temperature and pressure. *Analytical Chemistry*, **82**, 7965–7972. 21

Froyd, K., Murphy, D., Lawson, P., Baumgardner, D. & Herman, R. (2010). Aerosols that form subvisible cirrus at the tropical tropopause. *Atmospheric Chemistry and Physics*, **10**, 209–218. 10

Gallimore, P.J., Achakulwisut, P., Pope, F.D., Davies, J.F., Spring, D.R. & Kalberer, M. (2011). Importance of relative humidity in the oxidative ageing of organic aerosols: case study of the ozonolysis of maleic acid aerosol. *Atmospheric Chemistry and Physics*, **11**, 12181–12195. 13

Gysel, M., Weingartner, E., Nyeki, S., Paulsen, D., Baltensperger, U., Galambos, I. & Kiss, G. (2004). Hygroscopic properties of water-soluble matter and humic-like organics in atmospheric fine aerosol. *Atmospheric Chemistry and Physics*, **4**, 35–50. 82

Ha, Z. & Chan, C.K. (1999). The water activities of $MgCl_2$, $Mg(NO_3)_2$, $MgSO_4$, and their mixtures. *Aerosol Science & Technology*, **31**, 154–169. 28

Hall, W.A. & Johnston, M.V. (2011). Oligomer content of α-pinene secondary organic aerosol. *Aerosol Science and Technology*, **45**, 37–45. 27

Hallquist, M., Wenger, J., Baltensperger, U., Rudich, Y., Simpson, D., Claeys, M., Dommen, J., Donahue, N., George, C., Goldstein, A. *et al.* (2009). The formation, properties and impact of secondary organic aerosol: current and emerging issues. *Atmospheric Chemistry and Physics*, **9**, 5155–5236. 8

Hancock, B.C. & Zografi, G. (1997). Characteristics and significance of the amorphous state in pharmaceutical systems. *Journal of Pharmaceutical Sciences*, **86**, 1–12. 99

Hanford, K.L., Mitchem, L., Reid, J.P., Clegg, S.L., Topping, D.O. & McFiggans, G.B. (2008). Comparative thermodynamic studies of aqueous glutaric acid, ammonium sulfate and sodium chloride aerosol at high humidity. *The Journal of Physical Chemistry A*, **112**, 9413–9422. 80

Hargreaves, G., Kwamena, N.O., Zhang, Y., Butler, J., Rushworth, S., Clegg, S. & Reid, J. (2010). Measurements of the equilibrium size of supersaturated aqueous sodium chloride droplets at low relative humidity using aerosol optical tweezers and an electrodynamic balance. *The Journal of Physical Chemistry A*, **114**, 1806–1815. 80

He, X., Fowler, A. & Toner, M. (2006). Water activity and mobility in solutions of glycerol and small molecular weight sugars: Implication for cryo- and lyopreservation. *Journal of Applied Physics*, **100**, 074702. xvi, 17, 46, 47, 48

Heald, C.L., Henze, D.K., Horowitz, L.W., Feddema, J., Lamarque, J.F., Guenther, A., Hess, P.G., Vitt, F., Seinfeld, J.H., Goldstein, A.H. & Fung, I. (2008). Predicted change in global secondary organic aerosol concentrations in response to future climate, emissions, and land use change. *Journal of Geophysical Research: Atmospheres*, **113**, D05211. 3

Heaton, K.J., Sleighter, R.L., Hatcher, P.G., Hall IV, W.A. & Johnston, M.V. (2009). Composition domains in monoterpene secondary organic aerosol. *Environmental Science & Technology*, **43**, 7797–7802. 27

Hersey, S.P., Craven, J.S., Metcalf, A.R., Lin, J., Lathem, T., Suski, K.J., Cahill, J.F., Duong, H.T., Sorooshian, A., Jonsson, H.H. *et al.* (2013). Composition and hygroscopicity of the Los Angeles aerosol: CalNex. *Journal of Geophysical Research: Atmospheres*, **118**, 3016–3036. 49

Holz, M., Heil, S.R. & Sacco, A. (2000). Temperature-dependent self-diffusion coefficients of water and six selected molecular liquids for calibration in accurate 1H NMR PFG measurements. *Physical Chemistry Chemical Physics*, **2**, 4740–4742. 46

Hosny, N.A., Fitzgerald, C., Tong, C., Kalberer, M., Kuimova, M.K. & Pope, F.D. (2013). Fluorescent lifetime imaging of atmospheric aerosols: a direct probe of aerosol viscosity. *Faraday Discussions*, **165**, 343–356. 7, 8, 16

Houle, F.A., Hinsberg, W.D. & Wilson, K.R. (2015). Oxidation of a model alkane aerosol by OH radical: the emergent nature of reactive uptake. *Physical Chemistry Chemical Physics*, **17**, 4412–4423. 112

Jia, L. & Xu, Y. (2014). Effects of relative humidity on ozone and secondary organic aerosol formation from the photooxidation of benzene and ethylbenzene. *Aerosol Science and Technology*, **48**, 1–12. 15

Jimenez, J., Canagaratna, M., Donahue, N., Prevot, A., Zhang, Q., Kroll, J., DeCarlo, P., Allan, J., Coe, H., Ng, N. *et al.* (2009). Evolution of organic aerosols in the atmosphere. *Science*, **326**, 1525–1529. 2, 3

Jost, W. (1960). *Diffusion in solids, liquids, gases*. Physical chemistry, Academic Press. 32

Jurányi, Z., Gysel, M., Duplissy, J., Weingartner, E., Tritscher, T., Dommen, J., Henning, S., Ziese, M., Kiselev, A., Stratmann, F. *et al.* (2009). Influence of gas-to-particle partitioning on the hygroscopic and

droplet activation behaviour of α-pinene secondary organic aerosol. *Physical Chemistry Chemical Physics*, **11**, 8091–8097. 65

Kanakidou, M., Seinfeld, J., Pandis, S., Barnes, I., Dentener, F., Facchini, M., Dingenen, R.V., Ervens, B., Nenes, A., Nielsen, C. *et al.* (2005). Organic aerosol and global climate modelling: a review. *Atmospheric Chemistry and Physics*, **5**, 1053–1123. 2

Kidd, C., Perraud, V. & Finlayson-Pitts, B.J. (2014a). New insights into secondary organic aerosol from the ozonolysis of α-pinene from combined infrared spectroscopy and mass spectrometry measurements. *Physical Chemistry Chemical Physics*, **16**, 22706–22716. 105

Kidd, C., Perraud, V., Wingen, L.M. & Finlayson-Pitts, B.J. (2014b). Integrating phase and composition of secondary organic aerosol from the ozonolysis of α-pinene. *Proceedings of the National Academy of Sciences*, **111**, 7552–7557. 113

King, S.M., Rosenoern, T., Shilling, J.E., Chen, Q. & Martin, S.T. (2007). Cloud condensation nucleus activity of secondary organic aerosol particles mixed with sulfate. *Geophysical Research Letters*, **34**, L24806. 65

Knopf, D.A., Anthony, L.M. & Bertram, A.K. (2005). Reactive uptake of O_3 by multicomponent and multiphase mixtures containing oleic acid. *The Journal of Physical Chemistry A*, **109**, 5579–5589. 13

Kohen, A. & Limbach, H.H. (2005). *Isotope effects in chemistry and biology*. CRC Press. 37

Kolesar, K.R., Buffaloe, G., Wilson, K.R. & Cappa, C.D. (2014). OH-initiated heterogeneous oxidation of internally-mixed squalane and secondary organic aerosol. *Environmental Science & Technology*, **48**, 3196–3202. 14, 112, 113

Koop, T., Luo, B., Tsias, A. & Peter, T. (2000). Water activity as the determinant for homogeneous ice nucleation in aqueous solutions. *Nature*, **406**, 611–614. 88, 110

Koop, T., Bookhold, J., Shiraiwa, M. & Pöschl, U. (2011). Glass transition and phase state of organic compounds: dependency on molecular properties and implications for secondary organic aerosols in the atmosphere. *Physical Chemistry Chemical Physics*, **13**, 19238–19255. xii, xiii, 4, 7, 8, 17, 63, 75, 79, 89

Kuwata, M. & Martin, S.T. (2012). Phase of atmospheric secondary organic material affects its reactivity. *Proceedings of the National Academy of Sciences*, **109**, 17354–17359. 13

Ladino, L., Zhou, S., Yakobi-Hancock, J., Aljawhary, D. & Abbatt, J. (2014). Factors controlling the ice nucleating abilities of α-pinene SOA particles. *Journal of Geophysical Research: Atmospheres*, **119**, 9041–9051. 10, 109, 110

Lambe, A., Onasch, T., Massoli, P., Croasdale, D., Wright, J., Ahern, A., Williams, L., Worsnop, D., Brune, W. & Davidovits, P. (2011). Laboratory studies of the chemical composition and cloud condensation nuclei (CCN) activity of secondary organic aerosol (SOA) and oxidized primary organic aerosol (OPOA). *Atmospheric Chemistry and Physics*, **11**, 8913–8928. 65

Lee, A.K., Ling, T. & Chan, C.K. (2008). Understanding hygroscopic growth and phase transformation of aerosols using single particle *r*aman spectroscopy in an electrodynamic balance. *Faraday Discussions*, **137**, 245–263. 21

Lee, J.W.L., Carrascon, V., Gallimore, P.J., Fuller, S.J., Bjorkegren, A., Spring, D.R., Pope, F.D. & Kalberer, M. (2012). The effect of humidity on the ozonolysis of unsaturated compounds in aerosol particles. *Physical Chemistry Chemical Physics*, **14**, 8023–8031. 13

Li, K.K., Wang, F., Zeng, G., Reid, J.P. & Zhang, Y.H. (2011). Probing the time scale for bulk equilibration and mass transport of water in amorphous inorganic aerosol. *The Journal of Physical Chemistry B*, **115**, 14397–14403. 21, 55

Liao, L., Kerminen, V.M., Boy, M., Kulmala, M. & Dal Maso, M. (2014). Temperature influence on the natural aerosol budget over boreal forests. *Atmospheric Chemistry and Physics*, **14**, 8295–8308. 113

Lienhard, D.M., Bones, D.L., Zuend, A., Krieger, U.K., Reid, J.P. & Peter, T. (2012). Measurements of thermodynamic and optical properties of selected aqueous organic and organic–inorganic mixtures of atmospheric relevance. *The Journal of Physical Chemistry A*, **116**, 9954–9968. 28, 49

Lienhard, D.M., Huisman, A.J., Bones, D.L., Te, Y.F., Luo, B.P., Krieger, U.K. & Reid, J.P. (2014). Retrieving the translational diffusion coefficient of water from experiments on single levitated aerosol droplets. *Phys. Chem. Chem. Phys.*, **16**, 16677–16683. 17, 63, 65, 73

Ling, T.Y. & Chan, C.K. (2008). Partial crystallization and deliquescence of particles containing ammonium sulfate and dicarboxylic acids. *Journal of Geophysical Research: Atmospheres (1984–2012)*, **113**, D14205. 21

Liu, C., Shi, S., Weschler, C., Zhao, B. & Zhang, Y. (2013). Analysis of the dynamic interaction between SVOCs and airborne particles. *Aerosol Science and Technology*, **47**, 125–136. 11

Liu, H. & Macedo, E.A. (1995). Accurate correlations for the self-diffusion coefficients of CO_2, CH_4, C_2H_4, H_2O, and D_2O over wide ranges of temperature and pressure. *Journal of Supercritical Fluids*, **8**, 310–317. 46

Liu, Y., Zhu, T., Zhao, D. & Zhang, Z. (2008). Investigation of the hygroscopic properties of $Ca(NO_3)_2$ and internally mixed $Ca(NO_3)_2/CaCO_3$ particles by micro-Raman spectrometry. *Atmospheric Chemistry and Physics*, **8**, 7205–7215. 21

Loza, C.L., Coggon, M.M., Nguyen, T.B., Zuend, A., Flagan, R.C. & Seinfeld, J.H. (2013). On the mixing and evaporation of secondary organic aerosol components. *Environmental Science & Technology*, **47**, 6173–6180. 11, 111

REFERENCES

Lu, J.W., Rickards, A.M.J., Walker, J.S., Knox, K.J., Miles, R.E.H., Reid, J.P. & Signorell, R. (2014). Timescales of water transport in viscous aerosol: measurements on sub-micron particles and dependence on conditioning history. *Physical Chemistry Chemical Physics*, **16**, 9819–9830. 7

Mapes, M.K., Swallen, S.F. & Ediger, M. (2006). Self-diffusion of supercooled o-terphenyl near the glass transition temperature. *The Journal of Physical Chemistry B*, **110**, 507–511. 5

Markwardt, C.B. (2009). Non-linear least squares fitting in IDL with MPFIT. *arXiv preprint arXiv:0902.2850*. 37, 65, 93

Martin, S.T. (2000). Phase transitions of aqueous atmospheric particles. *Chemical Reviews*, **100**, 3403–3454. 3

Matsunaga, N. & Nagashima, A. (1987). Saturation vapor pressure and critical constants of H_2O, D_2O, T_2O, and their isotopic mixtures. *International Journal of Thermophysics*, **8**, 681–694. 30, 31

Matthiesen, J., Smith, R.S. & Kay, B.D. (2011). Mixing it up: Measuring diffusion in supercooled liquid solutions of methanol and ethanol at temperatures near the glass transition. *The Journal of Physical Chemistry Letters*, **2**, 557–561. 63

McFarquhar, G.M., Heymsfield, A.J., Spinhirne, J. & Hart, B. (2000). Thin and subvisual tropopause tropical cirrus: Observations and radiative impacts. *Journal of the Atmospheric Sciences*, **57**, 1841–1853. 11

McGlashan, M. (1963). Deviations from Raoult's law. *Journal of Chemical Education*, **40**, 516–518. 65

Mikhailov, E., Vlasenko, S., Martin, S., Koop, T. & Pöschl, U. (2009). Amorphous and crystalline aerosol particles interacting with water vapor: conceptual framework and experimental evidence for restructuring, phase transitions and kinetic limitations. *Atmospheric Chemistry and Physics*, **9**, 9491–9522. 6, 8

Mills, R. (1973). Self-diffusion in normal and heavy water in the range 1-45°. *The Journal of Physical Chemistry*, **77**, 685–688. 46

Möhler, O., Benz, S., Saathoff, H., Schnaiter, M., Wagner, R., Schneider, J., Walter, S., Ebert, V. & Wagner, S. (2008). The effect of organic coating on the heterogeneous ice nucleation efficiency of mineral dust aerosols. *Environmental Research Letters*, **3**, 025007. 9, 109

Molinero, V. & Goddard III, W.A. (2005). Microscopic mechanism of water diffusion in glucose glasses. *Physical Review Letters*, **95**, 045701. 101

Murphy, D. & Koop, T. (2005). Review of the vapour pressures of ice and supercooled water for atmospheric applications. *Quarterly Journal of the Royal Meteorological Society*, **131**, 1539–1565. xx, 86

Murphy, D., Thomson, D. & Mahoney, M. (1998). In situ measurements of organics, meteoritic material, mercury, and other elements in aerosols at 5 to 19 kilometers. *Science*, **282**, 1664–1669. 2

Murphy, D.M., Cziczo, D.J., Froyd, K.D., Hudson, P.K., Matthew, B.M., Middlebrook, A.M., Peltier, R.E., Sullivan, A., Thomson, D.S. & Weber, R.J. (2006). Single-particle mass spectrometry of tropospheric aerosol particles. *Journal of Geophysical Research: Atmospheres*, **111**, D23S32. xii, 2, 113

Murray, B. (2008). Inhibition of ice crystallisation in highly viscous aqueous organic acid droplets. *Atmospheric Chemistry and Physics*, **8**, 5423–5433. 3

Murray, B., Haddrell, A., Peppe, S., Davies, J., Reid, J., O'Sullivan, D., Price, H., Kumar, R., Saunders, R., Plane, J. *et al.* (2012). Glass formation and unusual hygroscopic growth of iodic acid solution droplets with relevance for iodine mediated particle formation in the marine boundary layer. *Atmospheric Chemistry and Physics*, **12**, 8575–8587. 3, 6, 7, 22, 28

Murray, B.J. & Bertram, A.K. (2008). Inhibition of solute crystallisation in aqueous H^+–NH_4^+–SO_4^{2-}–H_2O droplets. *Physical Chemistry Chemical Physics*, **10**, 3287–3301. 3

Murray, B.J., Wilson, T.W., Dobbie, S., Cui, Z., Al-Jumur, S.M., Möhler, O., Schnaiter, M., Wagner, R., Benz, S., Niemand, M. *et al.* (2010). Heterogeneous nucleation of ice particles on glassy aerosols under cirrus conditions. *Nature Geoscience*, **3**, 233–237. 9, 10, 88

Norrish, R.S. (1966). An equation for the activity coefficients and equilibrium relative humidities of water in confectionery syrups. *International Journal of Food Science and Technology*, **1**, 1365–2621. xxii, 97, 99

O'Brien, R.E., Neu, A., Epstein, S.A., MacMillan, A.C., Wang, B., Kelly, S.T., Nizkorodov, S.A., Laskin, A., Moffet, R.C. & Gilles, M.K. (2014). Physical properties of ambient and laboratory generated secondary organic aerosol. *Geophysical Research Letters*, **41**, 4347–4353. 89, 113

Parker, R. & Ring, S.G. (1995). Diffusion in maltose-water mixtures at temperatures close to the glass transition. *Carbohydrate Research*, **273**, 147–155. 16

Parsons, M.T., Knopf, D.A. & Bertram, A.K. (2004). Deliquescence and crystallization of ammonium sulfate particles internally mixed with water-soluble organic compounds. *The Journal of Physical Chemistry A*, **108**, 11600–11608. 3

Peixoto, J. & Oort, A.H. (1996). The climatology of relative humidity in the atmosphere. *Journal of Cpplimate*, **9**, 3443–3463. xiii, 9

Perraud, V., Bruns, E.A., Ezell, M.J., Johnson, S.N., Yu, Y., Alexander, M.L., Zelenyuk, A., Imre, D., Chang, W.L., Dabdub, D. *et al.* (2012). Nonequilibrium atmospheric secondary organic aerosol formation and growth. *Proceedings of the National Academy of Sciences*, **109**, 2836–2841. 6, 11

Petters, M. & Kreidenweis, S. (2007). A single parameter representation of hygroscopic growth and cloud condensation nucleus activity. *Atmospheric Chemistry and Physics*, **7**, 1961–1971. 63, 65

Pfrang, C., Shiraiwa, M. & Pöschl, U. (2011). Chemical ageing and transformation of diffusivity in semi-solid multi-component organic aerosol particles. *Atmospheric Chemistry and Physics*, **11**, 7343–7354. 13

Pöschl, U. (2005). Atmospheric aerosols: composition, transformation, climate and health effects. *Angewandte Chemie International Edition*, **44**, 7520–7540. 1

Pöschl, U., Letzel, T., Schauer, C. & Niessner, R. (2001). Interaction of ozone and water vapor with spark discharge soot aerosol particles coated with benzo[a]pyrene:O_3 and H_2O adsorption, benzo[a]pyrene degradation, and atmospheric implications. *The Journal of Physical Chemistry A*, **105**, 4029–4041. 17

Power, R., Simpson, S., Reid, J. & Hudson, A. (2013). The transition from liquid to solid-like behaviour in ultrahigh viscosity aerosol particles. *Chemical Science*, **4**, 2597–2604. xvi, xxii, 7, 16, 49, 50, 55, 67, 99, 100, 103, 109

Prenni, A.J., DeMott, P.J., Kreidenweis, S.M., Sherman, D.E., Russell, L.M. & Ming, Y. (2001). The effects of low molecular weight dicarboxylic acids on cloud formation. *The Journal of Physical Chemistry A*, **105**, 11240–11248. 3

Prenni, A.J., Petters, M.D., Kreidenweis, S.M., DeMott, P.J. & Ziemann, P.J. (2007). Cloud droplet activation of secondary organic aerosol. *Journal of Geophysical Research: Atmospheres (1984–2012)*, **112**, D10223. 65

Prenni, A.J., Petters, M.D., Faulhaber, A., Carrico, C.M., Ziemann, P.J., Kreidenweis, S.M. & DeMott, P.J. (2009). Heterogeneous ice nucleation measurements of secondary organic aerosol generated from ozonolysis of alkenes. *Geophysical Research Letters*, **36**, L06808. 9

Rampp, M., Buttersack, C. & Lüdemann, H.D. (2000). c,t-dependence of the viscosity and the self-diffusion coefficients in some aqueous carbohydrate solutions. *Carbohydrate Research*, **328**, 561–572. xvi, xxii, 16, 47, 55, 67, 97, 99, 100

Ravishankara, A. (1997). Heterogeneous and multiphase chemistry in the troposphere. *Science*, **276**, 1058–1065. 2, 17, 88

Renbaum-Wolff, L., Grayson, J.W., Bateman, A.P., Kuwata, M., Sellier, M., Murray, B.J., Shilling, J.E., Martin, S.T. & Bertram, A.K. (2013). Viscosity of α-pinene secondary organic material and implications for particle growth and reactivity. *Proceedings of the National Academy of Sciences*, **110**, 8014–8019. xviii, 6, 7, 16, 27, 67, 68, 82, 89, 104, 106

Rickards, A.M., Miles, R.E., Davies, J.F., Marshall, F.H. & Reid, J.P. (2013). Measurements of the sensitivity of aerosol hygroscopicity and the κ parameter to the O/C ratio. *The Journal of Physical Chemistry A*, **117**, 14120–14131. 80

Riipinen, I., Yli-Juuti, T., Pierce, J.R., Petäjä, T., Worsnop, D.R., Kulmala, M. & Donahue, N.M. (2012). The contribution of organics to atmospheric nanoparticle growth. *Nature Geoscience*, **5**, 453–458. 8

Roberts, C. & Debenedetti, P.G. (1999). Structure and dynamics in concentrated, amorphous carbohydrate-water systems by molecular dynamics simulation. *The Journal of Physical Chemistry B*, **103**, 7308–7318. 17, 101

Robinson, C., Schill, G. & Tolbert, M. (2014). Optical growth of highly viscous organic/sulfate particles. *Journal of Atmospheric Chemistry*, **71**, 145–156. 8

Robinson, E.S., Saleh, R. & Donahue, N.M. (2013). Organic aerosol mixing observed by single-particle mass spectrometry. *The Journal of Physical Chemistry A*, **117**, 13935–13945. 12

Roldin, P., Eriksson, A., Nordin, E., Hermansson, E., Mogensen, D., Rusanen, A., Boy, M., Swietlicki, E., Svenningsson, B., Zelenyuk, A. *et al.* (2014). Modelling non-equilibrium secondary organic aerosol formation and evaporation with the aerosol dynamics, gas-and particle-phase chemistry kinetic multilayer model ADCHAM. *Atmospheric Chemistry and Physics*, **14**, 7953–7993. 15

Rössler, E., Warschewske, U., Eiermann, P., Sokolov, A. & Quitmann, D. (1994). Indications for a change of transport mechanism in supercooled liquids and the dynamics close and below T_g. *Journal of Non-Crystalline Solids*, **172**, 113–125. 5

Roth, C.M., Goss, K.U. & Schwarzenbach, R.P. (2005). Sorption of a diverse set of organic vapors to urban aerosols. *Environmental Science & Technology*, **39**, 6638–6643. 6, 11

Rubasinghege, G. & Grassian, V.H. (2013). Role(s) of adsorbed water in the surface chemistry of environmental interfaces. *Chemical Communications*, **49**, 3071–3094. 17

Saleh, R., Shihadeh, A. & Khlystov, A. (2011). On transport phenomena and equilibration time scales in thermodenuders. *Atmospheric Measurement Techniques*, **4**, 571–581. 8

Saleh, R., Donahue, N.M. & Robinson, A.L. (2013). Time scales for gas-particle partitioning equilibration of secondary organic aerosol formed from α-pinene ozonolysis. *Environmental Science & Technology*, **47**, 5588–5594. 12, 111

Saukko, E., Kuuluvainen, H. & Virtanen, A. (2012a). A method to resolve the phase state of aerosol particles. *Atmospheric Measurement Techniques*, **5**, 259–265. 7

Saukko, E., Lambe, A., Massoli, P., Koop, T., Wright, J., Croasdale, D., Pedernera, D., Onasch, T., Laaksonen, A., Davidovits, P. *et al.* (2012b). Humidity-dependent phase state of SOA particles from biogenic and anthropogenic precursors. *Atmospheric Chemistry and Physics*, **12**, 7517–7529. xvii, xix, 6, 8, 49, 51, 52, 69, 71

Schill, G. & Tolbert, M. (2013). Heterogeneous ice nucleation on phase-separated organic-sulfate particles: effect of liquid vs. glassy coatings. *Atmospheric Chemistry and Physics*, **13**, 4681–4695. 10

Seinfeld, J.H. & Pandis, S.N. (2012). *Atmospheric chemistry and physics: from air pollution to climate change*. John Wiley & Sons. xiii, 10, 48

Shiraiwa, M. & Seinfeld, J.H. (2012). Equilibration timescale of atmospheric secondary organic aerosol partitioning. *Geophysical Research Letters*, **39**, L24801. 8, 11

Shiraiwa, M., Pfrang, C. & Pöschl, U. (2010). Kinetic multi-layer model of aerosol surface and bulk chemistry (KM-SUB): the influence of interfacial transport and bulk diffusion on the oxidation of oleic acid by ozone. *Atmospheric Chemistry and Physics*, **10**, 3673–3691. 13

Shiraiwa, M., Ammann, M., Koop, T. & Pöschl, U. (2011). Gas uptake and chemical aging of semisolid organic aerosol particles. *Proceedings of the National Academy of Sciences*, **108**, 11003–11008. 13

Shiraiwa, M., Poschl, U. & Knopf, D.A. (2012). Multiphase chemical kinetics of NO_3 radicals reacting with organic aerosol components from biomass burning. *Environmental Science & Technology*, **46**, 6630–6636. 13

Shiraiwa, M., Zuend, A., Bertram, A.K. & Seinfeld, J.H. (2013). Gas–particle partitioning of atmospheric aerosols: interplay of physical state, non-ideal mixing and morphology. *Physical Chemistry Chemical Physics*, **15**, 11441–11453. xviii, 11, 15, 17, 67, 68, 70

Shiraiwa, M., Berkemeier, T., Schilling-Fahnestock, K.A., Seinfeld, J.H. & Pöschl, U. (2014). Molecular corridors and kinetic regimes in the multiphase chemical evolution of secondary organic aerosol. *Atmospheric Chemistry and Physics*, **14**, 8323–8341. 89

Shrestha, M., Zhang, Y., Ebben, C.J., Martin, S.T. & Geiger, F.M. (2013). Vibrational sum frequency generation spectroscopy of secondary organic material produced by condensational growth from α-pinene ozonolysis. *The Journal of Physical Chemistry A*, **117**, 8427–8436. 26

Slade, J.H. & Knopf, D.A. (2014). Multiphase OH oxidation kinetics of organic aerosol: The role of particle phase state and relative humidity. *Geophysical Research Letters*, **41**, 5297–5306. 13, 15

Smith, M., Kuwata, M. & Martin, S. (2011). Secondary organic material produced by the dark ozonolysis of α-pinene minimally affects the deliquescence and efflorescence of ammonium sulfate. *Aerosol Science and Technology*, **45**, 244–261. 84

Smith, R.S. & Kay, B.D. (1999). The existence of supercooled liquid water at 150 K. *Nature*, **398**, 788–791. 63

Solomon, S., Rosenlof, K.H., Portmann, R.W., Daniel, J.S., Davis, S.M., Sanford, T.J. & Plattner, G.K. (2010). Contributions of stratospheric water vapor to decadal changes in the rate of global warming. *Science*, **327**, 1219–1223. 11

Steimer, S.S., Lampimäki, M., Coz, E., Grzinic, G. & Ammann, M. (2014). The influence of physical state on shikimic acid ozonolysis: a case for in situ microspectroscopy. *Atmospheric Chemistry and Physics*, **14**, 10761–10772. 13

Stillinger, F.H. *et al.* (1995). A topographic view of supercooled liquids and glass formation. *Science*, **267**, 1935–1939. 5

Svishchev, I. & Kusalik, P. (1994). Dynamics in liquid H_2O, D_2O, and T_2O: a comparative simulation study. *The Journal of Physical Chemistry*, **98**, 728–733. 46

Tong, H.J., Reid, J., Bones, D., Luo, B. & Krieger, U. (2011). Measurements of the timescales for the mass transfer of water in glassy aerosol at low relative humidity and ambient temperature. *Atmospheric Chemistry and Physics*, **11**, 4739–4754. 7, 17, 28, 46

Tritscher, T., Dommen, J., DeCarlo, P., Gysel, M., Barmet, P., Praplan, A., Weingartner, E., Prévôt, A., Riipinen, I., Donahue, N. *et al.* (2011). Volatility and hygroscopicity of aging secondary organic

aerosol in a smog chamber. *Atmospheric Chemistry and Physics*, **11**, 11477–11496. 65

Tsigaridis, K., Daskalakis, N., Kanakidou, M., Adams, P.J., Artaxo, P., Bahadur, R., Balkanski, Y., Bauer, S.E., Bellouin, N., Benedetti, A., Bergman, T., Berntsen, T.K., Beukes, J.P., Bian, H., Carslaw, K.S., Chin, M., Curci, G., Diehl, T., Easter, R.C., Ghan, S.J., Gong, S.L., Hodzic, A., Hoyle, C.R., Iversen, T., Jathar, S., Jimenez, J.L., Kaiser, J.W., Kirkevåg, A., Koch, D., Kokkola, H., Lee, Y.H., Lin, G., Liu, X., Luo, G., Ma, X., Mann, G.W., Mihalopoulos, N., Morcrette, J.J., Müller, J.F., Myhre, G., Myriokefalitakis, S., Ng, N.L., O'Donnell, D., Penner, J.E., Pozzoli, L., Pringle, K.J., Russell, L.M., Schulz, M., Sciare, J., Seland, Ø., Shindell, D.T., Sillman, S., Skeie, R.B., Spracklen, D., Stavrakou, T., Steenrod, S.D., Takemura, T., Tiitta, P., Tilmes, S., Tost, H., van Noije, T., van Zyl, P.G., von Salzen, K., Yu, F., Wang, Z., Wang, Z., Zaveri, R.A., Zhang, H., Zhang, K., Zhang, Q. & Zhang, X. (2014). The AeroCom evaluation and intercomparison of organic aerosol in global models. *Atmospheric Chemistry and Physics*, **14**, 10845–10895. 8

Vaden, T.D., Imre, D., Beránek, J., Shrivastava, M. & Zelenyuk, A. (2011). Evaporation kinetics and phase of laboratory and ambient secondary organic aerosol. *Proceedings of the National Academy of Sciences*, **108**, 2190–2195. 11

Vignes, A. (1966). Diffusion in binary solutions. Variation of diffusion coefficient with composition. *Industrial & Engineering Chemistry Fundamentals*, **5**, 189–199. 63

Virtanen, A., Joutsensaari, J., Koop, T., Kannosto, J., Yli-Pirilä, P., Leskinen, J., Mäkelä, J.M., Holopainen, J.K., Pöschl, U., Kulmala, M. *et al.* (2010). An amorphous solid state of biogenic secondary organic aerosol particles. *Nature*, **467**, 824–827. 6, 16

Wagner, R., Möhler, O., Saathoff, H., Schnaiter, M., Skrotzki, J., Leisner, T., Wilson, T., Malkin, T. & Murray, B. (2012). Ice cloud processing of ultra-viscous/glassy aerosol particles leads to enhanced ice nucleation ability. *Atmospheric Chemistry and Physics*, **12**, 8589–8610. 9, 28

Wang, B., Lambe, A.T., Massoli, P., Onasch, T.B., Davidovits, P., Worsnop, D.R. & Knopf, D.A. (2012). The deposition ice nucleation and immersion freezing potential of amorphous secondary organic aerosol: Pathways for ice and mixed-phase cloud formation. *Journal of Geophysical Research: Atmospheres (1984–2012)*, **117**, D16209. 9, 16, 88

Wang, B., O'Brien, R.E., Kelly, S.T., Shilling, J.E., Moffet, R.C., Gilles, M.K. & Laskin, A. (2014). Reactivity of liquid and semi-solid secondary organic carbon with chloride and nitrate in atmospheric aerosols. *The Journal of Physical Chemistry A*, **119**, 4498–4508. 15

Wang, F., Zhang, Y.H., Li, S.H., Wang, L.Y. & Zhao, L.J. (2005). A strategy for single supersaturated droplet analysis: Confocal Raman investigations on the complicated hygroscopic properties of individual $MgSO_4$ droplets on the quartz substrate. *Analytical Chemistry*, **77**, 7148–7155. 55

Wayne, R. (2000). *Chemistry of Atmospheres, 3rd*. Oxford University Press, Inc.: New York, USA. 113

Weitkamp, E.A., Hartz, K.E.H., Sage, A.M., Donahue, N.M. & Robinson, A.L. (2008a). Laboratory measurements of the heterogeneous oxidation of condensed-phase organic molecular makers for meat cooking emissions. *Environmental Science & Technology*, **42**, 5177–5182. 14, 112

Weitkamp, E.A., Lambe, A.T., Donahue, N.M. & Robinson, A.L. (2008b). Laboratory measurements of the heterogeneous oxidation of condensed-phase organic molecular makers for motor vehicle exhaust. *Environmental Science & Technology*, **42**, 7950–7956. 14, 112

Wilson, J.M., Imre, D., Beranek, J., Shrivastava, M. & Zelenyuk-Imre, A. (2014). Evaporation kinetics of laboratory-generated secondary organic aerosols at elevated relative humidity. *Environmental Science & Technology*, **49**, 243–249. 12, 113

Wilson, T., Murray, B., Wagner, R., Möhler, O., Saathoff, H., Schnaiter, M., Skrotzki, J., Price, H., Malkin, T., Dobbie, S. *et al.* (2012). Glassy aerosols with a range of compositions nucleate ice heterogeneously at cirrus temperatures. *Atmospheric Chemistry and Physics*, **12**, 8611–8632. 9, 88

Wise, M.E., Baustian, K.J., Koop, T., Freedman, M.A., Jensen, E.J. & Tolbert, M.A. (2012). Depositional ice nucleation onto crystalline hydrated NaCl particles: a new mechanism for ice formation in the troposphere. *Atmospheric Chemistry and Physics*, **12**, 1121–1134. 21

Wong, J.P., Liggio, J., Li, S.M., Nenes, A. & Abbatt, J.P. (2014). Suppression in droplet growth kinetics by the addition of organics to sulfate particles. *Journal of Geophysical Research: Atmospheres*, **119**, 12–222. 8

Yatavelli, R., Stark, H., Thompson, S., Kimmel, J., Cubison, M., Day, D., Campuzano-Jost, P., Palm, B., Hodzic, A., Thornton, J. *et al.* (2014). Semicontinuous measurements of gas–particle partitioning of organic acids in a ponderosa pine forest using a MOVI-HRToF-CIMS. *Atmospheric Chemistry and Physics*, **14**, 1527–1546. 12

Yeung, M.C., Lee, A.K. & Chan, C.K. (2009). Phase transition and hygroscopic properties of internally mixed ammonium sulfate and adipic acid (AS-AA) particles by optical microscopic imaging and Raman spectroscopy. *Aerosol Science and Technology*, **43**, 387–399. 21

Zardini, A., Sjogren, S., Marcolli, C., Krieger, U., Gysel, M., Weingartner, E., Baltensperger, U. & Peter, T. (2008). A combined particle trap/HTDMA hygroscopicity study of mixed inorganic/organic aerosol particles. *Atmospheric Chemistry and Physics*, **8**, 5589–5601. 3, 82

Zaveri, R., Easter, R., Shilling, J. & Seinfeld, J. (2014). Modeling kinetic partitioning of secondary organic aerosol and size distribution dynamics: representing effects of volatility, phase state, and particle-phase reaction. *Atmospheric Chemistry and Physics*, **14**, 5153–5181. 15

Zhang, X., Pandis, S.N. & Seinfeld, J.H. (2012). Diffusion-limited versus quasi-equilibrium aerosol growth. *Aerosol Science and Technology*, **46**, 874–885. 8

Zhang, Y., Sanchez, M., Douet, C., Wang, Y., Bateman, A., Gong, Z., Kuwata, M., Renbaum-Wolff, L., Sato, B., Liu, P. *et al.* (2015). Changing shapes and implied viscosities of suspended submicron particles. *Atmospheric Chemistry and Physics Discussions*, **15**, 6821–6850. 65

Zhang, Y.H. & Chan, C.K. (2000). Study of contact ion pairs of supersaturated magnesium sulfate solutions using raman scattering of levitated single droplets. *The Journal of Physical Chemistry A*, **104**, 9191–9196. 55

Zhao, L.J., Zhang, Y.H., Wei, Z.F., Cheng, H. & Li, X.H. (2006). Magnesium sulfate aerosols studied by FTIR spectroscopy: hygroscopic properties, supersaturated structures, and implications for seawater aerosols. *The Journal of Physical Chemistry A*, **110**, 951–958. 55

Zhou, S., Lee, A., McWhinney, R. & Abbatt, J. (2012). Burial effects of organic coatings on the heterogeneous reactivity of particle-borne benzo[a]pyrene (BaP) toward ozone. *The Journal of Physical Chemistry A*, **116**, 7050–7056. 14

Zhou, S., Shiraiwa, M., McWhinney, R.D., Pöschl, U. & Abbatt, J.P. (2013). Kinetic limitations in gas-particle reactions arising from slow diffusion in secondary organic aerosol. *Faraday Discussions*, **165**, 391–406. 14, 17, 89, 104, 106, 112, 113

Zhu, L., Cai, T., Huang, J., Stringfellow, T.C., Wall, M. & Yu, L. (2011). Water self-diffusion in glassy and liquid maltose measured by Raman microscopy and NMR. *The Journal of Physical Chemistry B*, **115**, 5849–5855. 16, 17, 21, 32, 67

Zobrist, B., Marcolli, C., Pedernera, D. & Koop, T. (2008). Do atmospheric aerosols form glasses? *Atmospheric Chemistry and Physics*, **8**, 5221–5244. 6, 49, 52

Zobrist, B., Soonsin, V., Luo, B.P., Krieger, U.K., Marcolli, C., Peter, T. & Koop, T. (2011). Ultra-slow water diffusion in aqueous sucrose glasses. *Physical Chemistry Chemical Physics*, **13**, 3514–3526. xvi, xxii, 8, 17, 28, 46, 47, 49, 50, 51, 73, 75, 79, 97, 99